UNIVERSITÀ DEGLI STUDI DI PADOVA

Dipartimento di Fisica e Astronomia "Galileo Galilei"

Master Degree in Astrophysics and Cosmology

Final Dissertation

Very Massive Stars and Their Compact Remnants

Thesis supervisor

Dr. Giuliano Iorio

Thesis co-supervisors

Prof.ssa Michela Mapelli

Dr. Stefano Torniamenti

Candidate

Filippo Simonato

Academic Year 2023/2024

Contents

List of Figures

Abstract

At the end of carbon burning, very massive stars (VMSs, $M_{star} \geq 100\ M_{\odot}$) can efficiently produce electron-positron pairs in their core, triggering an instability that leads either to the ejection of a fraction of their mass in multiple pulsations (pulsational pair-instability supernova) or to their complete destruction (pair-instability supernova). Despite the robust theoretical framework pair-instability theory is grounded in, we still do not have any unquestionable detection of a pair-instability supernova. Thus far, VMS modellers have implemented wind models, that could have under-estimated the mass-loss rate. As a consequence, the predicted maximum metallicity at which stars are expected to enter the pair-instability regime might be excessively high. In this Thesis, I studied the evolution of very massive stars with a new model for radiation-driven stellar winds, focusing on low metallicities, to obtain an accurate prediction for the pair-instability supernova rate density. To this purpose, I modelled the evolution of very massive stars using the stellar evolution code MESA. I modelled them as single stars and binary systems, following episodes of mass transfer. I then used my models to produce stellar tracks for the rapid population synthesis code SEVN, which is optimized to simulate several millions of single and binary stars per day, probing the parameter space of pair-instability supernovae. Finally, I modelled the evolution of the pair-instability supernova rate as function of redshift, by combining my population synthesis models with a metal-dependent cosmic star formation rate history.

Chapter 1

Introduction

Pair-instability supernovae and pulsational pair-instability supernovae can occur when the pair creation becomes efficient: the energy of the photons, which should provide the radiation pressure to contrast the gravitational collapse, is now diverted in the creation of electrons and positrons, resulting in a dynamical instability. As a consequence of this instability, the star starts to contract, igniting explosive nuclear reactions, which involve oxygen and silicon. If the mass of the helium core is between 64 and 135 $M_{\odot}$, the star is expected to explode leaving no compact remnant (pair-instability supernova); instead, if the mass of the helium core is between 32 and 64 $M_{\odot}$, the star can undergo strong mass ejections in different pulsations (pulsational pair-instability supernova), before collapsing into a black hole. These kinds of supernovae have been predicted to occur at the end of VMSs life-cycle. Despite the fact that, based on theoretical models, we would have expected to observe them in the Small Magellanic Cloud, we do not have any uncontroversial detection of them. This suggests that the expected rate of events could be over-estimated due to our insufficient comprehension of VMS evolution.
In this thesis work, I studied the evolution of very massive stars implementing a new model for stellar winds to obtain new, updated predictions for the pair-instability and pulsational-pair instability rate density. The thesis is organized as follows.
In Chapter 2, I present the state-of-art knowledge of very massive star evolution: I discuss quasi-chemically homogeneous evolution, the expected behaviour of very massive stars on the Hertzsprung-Russell diagram, the main parameters that affect their evolution, such that rotation and metallicity. Depending on the metallicity and the mass of the helium core, very massive stars can experience different phenomena at the end of their life: they can undergo core-collapse supernovae, pair-instability supernovae or directly collapse into a black hole; their relevance as possible progenitors of intermediate-mass black holes is pointed out here. Then, I discuss the observed properties of very massive stars and the main uncertainties of the models used to describe them. In this Chapter, I also describe the new model for the stellar winds, why it is necessary and its uncertainties. I introduce the concept of transition mass-loss and explain how it has been exploited to extend the wind model to the low metallicity regime. Finally, I describe the astrophysical relevance of binary star systems. A description of how companion stars in these systems can interact and transfer their mass each other is carried out. Binary evolution is the most common evolutionary channel of very massive stars and typical processes occurring in these systems, like Roche-lobe overflow, common envelope or even stellar mergers, can strongly affect their evolution.
Chapter 3 is completely dedicated to introduce the pair-instability regime. I present the stability criterion and an analysis of pair-instability and pulsational pair-instability supernovae. Here, I mention the most suitable pair-instability supernova candidate and how to study the occurrence of these events through their chemical signature. Finally, I summarize the observational constraints on the pair-instability supernova rate density.
Chapter 4 describes the tools I used to compute very massive star models. I describe stellar evolution codes, developed to model the interior of a star and evolve it over the time by integrating the stellar structure differential equations. In particular, I focus on the code MESA, which I have used for my

simulations, describing its treatment of very massive stars and mass transfer in binary system. I used my MESA models to produce tables for SEVN, a population synthesis code. Population synthesis codes can perform the evolution of several millions of stellar systems in a day by interpolating pre-computed stellar tracks. So, here I give a general overview about population synthesis codes and the SEVN evolution algorithm. In the last part of this Chapter, I illustrate how it is possible to combine the results of SEVN with data-driven prescriptions for star formation rate and metallicity evolution through the semi-analytic code COSMORATE to model pair-instability and pulsational pair-instability rate density across cosmic time.
Chapter 5 contains the main results of the simulations performed with MESA for single stellar models and binary systems. Finally, I show a comparison between the rate density obtained with the old and the new model for stellar winds and a new prediction for its evolution through the Universe history.

Chapter 2

Very Massive Stars

In this Chapter I describe the evolution and fate of very massive stars ($M_{star} \geq 100\ M_\odot$), indicating the possible candidates and observed properties. Then, I analyze a new physical model for their stellar winds. Finally, I discuss very massive binaries and the processes that can occur in this scenario.

2.1 Evolution and Observations

Very massive stars (VMSs) are defined as stars with a mass higher than 100 $M_\odot$. The mechanism that allows the formation of such massive stars is still one of the main open questions in modern astrophysics. Two different channels are considered: formation via gas accretion and formation via collisions between less massive stars. Both these processes have some critical issues.
In the gas accretion channel, one challenge is represented by fragmentation. When a gravitationally-unstable medium collapses, it tends to produce stars with a characteristic mass comparable to the Jeans mass M_J:

$$M_J = \frac{\pi}{6}\,\frac{c_s^3}{\sqrt{G^3\,\rho}} = 0.5\left(\frac{T}{10\ \mathrm{K}}\right)^{3/2}\left(\frac{n}{10^4\ \mathrm{cm^{-3}}}\right)^{1/2} \mathrm{M_\odot}\,, \tag{2.1}$$

where c_s is the sound speed, ρ is the gas density, T is the gas temperature, and n is the gas number density. A very massive star is an object whose mass is higher than the Jeans mass of the interstellar medium from which it is forming and one can expect that the gas fragments into various small stars rather than forming a single large one. One possible solution is that radiation feedback and magnetic fields can reduce fragmentation by heating the gas, removing angular momentum and providing extra pressure that prevents the collapse (Krumholz, 2015 [1]).
Population III (Pop. III) stars are the first stars in the Universe, born from the nucleosynthesis of the primordial material, where no heavy metals were present, and, as a consequence, with metallicity $Z \sim 0$. It was thought that the first stars were massive because of the lack of efficient cooling agents in the primordial gas. Indeed, molecules of H_2 are the main coolants for the collapse of primordial clouds, which are less efficient in cooling than heavier metals. H_2 can remain hot during the collapse, leading to formation of VMSs. So, due to the fact that $M_J \propto T^{3/2}$, the evolution of very massive stars was only considered in the context of Pop. III stars. In many cases, simulations validate these results (Abel et al., 2000 [2], Bromm et al., 2009 [3]), but observations of VMSs in the Local Universe suggest that they can be relevant also at non-zero metallicity (Crowther et al. 2010 [16]).
There are no strong arguments against the idea that VMSs form via gas accretion like lower mass stars. However, as aforementioned, they can form also through a totally different channel, the collisional channel. In this case, the main challenge is related to the small cross-sectional area with respect to interstellar separation. If gravitational attraction is significant in enhancing collision rates, the mean time t_{coll} between collisions in a cluster is

$$t_{\mathrm{coll}} = 7.1\, n_4^{-2}\, \sigma_1\, r_0^{-1}\, m_0^{-1}\ \mathrm{Myr}\,, \tag{2.2}$$

where $n_4 = n/10^4$ stars pc^{-3} and n is the number density of stars in the cluster, $\sigma_1 = \sigma/\ 10$ km s^{-1} and σ is the velocity dispersion, $r_0 = r/\mathrm{R_\odot}$ and r is the radius, $m_0 = m/\mathrm{M_\odot}$ and m is the mass. Thus,

under the observed conditions ($n \sim 10^4$ pc^{-3}), we expect ≤ 1 collision between 1 M$_\odot$ stars to occur within the lifetime of a massive star in star clusters. Even under the most optimistic assumptions, production of very massive stars via collisions requires that clusters reach densities much higher than the ones seen in young clusters. This very dense phase must be short, since it is not observed; models for the production of very massive stars via collisions consist largely on proposals for how to produce such a short, very dense, phase (Krumholz, 2015 [1]).
After having reviewed the two main formation channels for VMSs, I analyse the evolution, fate and observations of these stars in the next sections.

2.1.1 From Main Sequence to Advanced Evolutionary Phases

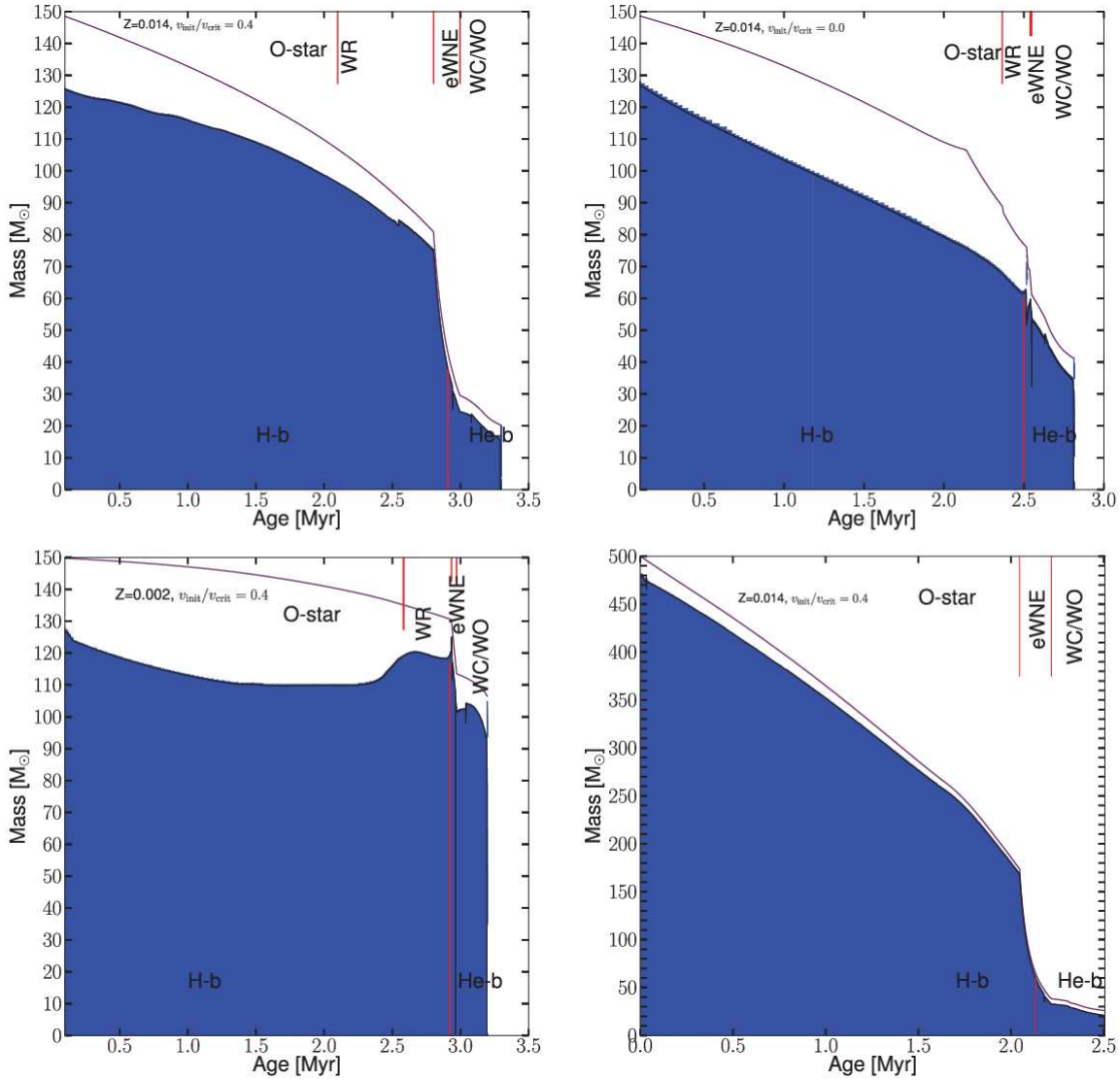

Figure 2.1: Time evolution of the mass: rotating Z = 0.014, $M_{\rm init} = 150$ M$_\odot$ (top-left) and non-rotating (top-right) models, rotating Z = 0.002, $M_{\rm init} = 150$ M$_\odot$ model (bottom left), and rotating Z = 0.014, $M_{\rm init} = 500$ M$_\odot$ model (bottom right). The blue zones represent the convective regions. The top solid black line indicates the total mass of the star, and vertical red markers are given for the different phases at the top of the plots: O-type, WR = eWNL, eWNE, and WC/WO. The transition between H- and He-burning phases is indicated by the red vertical line at the bottom of the plots [7].

The evolution of VMSs is quite similar to the one of massive stars (8 M$_\odot \leq M_{\rm star} \leq 100$ M$_\odot$), with differences in the advanced phases and final fate of these stars. The mass-loss plays an important role and strongly impacts their evolution. While the mass-loss driving mechanism is generally well understood for O-type stars (hot, blue-white stars), the main uncertainties affect the evolutionary phase in

which VMSs enter the regime of optically-thick winds. The terms optically-thick and optically-thin winds describe how opaque is the wind to radiation emitted by the star: an optically-thin wind is transparent to most of the radiation passing through it; in optically-thick winds, the radiation is strongly absorbed and re-emitted or scattered by the wind material and the interaction affects the structure and dynamics of the wind. In this Section, which follows Hirschi (2017 [7]), I discuss the following wind models: Vink et al. (2001 [4]) for radiative line-driven winds; de Jager et al. (1988 [5]) in the range $\log(T_{\rm eff}/{\rm K}) \geq 3.7$; Bennett et al. (2012 [6]) for $\log(T_{\rm eff}/{\rm K}) \leq 3.7$. A new model (Sabhahit et al., 2022 [32], 2023 [38]) that effectively characterizes the transition from an optically-thin to an optically-thick wind in VMSs is described in Section 2.2.

During the main sequence (MS), VMSs have a huge convective core that, for initial mass of the star $\geq$ 150 $M_\odot$, can represent more than 75% of the total mass. They evolve quasi-chemically homogeneously even if processes that induce mixing, like rotation, are not present in the radiative zones. Quasi-chemically homogeneous evolution means that a massive star remains nearly chemically uniform throughout its interior during its evolution, rather than developing the typical layered structure seen in most stars: the mixing timescale is shorter than the nuclear timescale and the material produced in the core is redistributed in the envelope. This is a consequence of low C-N-O content and high central temperature, as for massive stars. In the advanced evolutionary phases, the total mass decreases slower than the convective core mass and the part occupied by it is smaller. In Fig. 2.1 the impact of metallicity and rotation is shown. In each plot, the different phases are highlighted by red markers: eWNL indicates Wolf-Rayet star of the nitrogen type when the superficial hydrogen fraction X_s is between 0.3 and 0.005, eWNL are Wolf-Rayet stars of the nitrogen type when the superficial hydrogen fraction $X_s < 0.005$, WC and WO indicate Wolf-Rayet star of the carbon and oxygen type respectively. Wolf-Rayet (WR) stars are evolved, massive stars that have completely lost their hydrogen envelope and are fusing helium or heavier elements in the core. The top-left panel shows a model at Z = 0.014, $M_{\rm init}$ = 150 $M_\odot$ and rotating at $v_{\rm init}/v_{\rm crit} = 0.4$, the top-right panel a non-rotating $Z = 0.014$ and $M_{\rm init}$ = 150 $M_\odot$ model, the bottom-left panel a model at $Z = 0.002$, $M_{\rm init}$ = 150 $M_\odot$ and $v_{\rm init}/v_{\rm crit} = 0.4$, the bottom-left panel a model at $Z = 0.014$, $M_{\rm init}$ = 500 $M_\odot$ and $v_{\rm init}/v_{\rm crit} = 0.4$. In rotating models, the size of the convective zone stands high due to additional mixing and can lead to an increase of the zone: this is a consequence of quasi-chemically homogeneous evolution studied also in massive stars. In the 500 $M_\odot$ model, the size of the convective region is even higher and evolves quasi-chemically homogeneously for all its life.

VMSs are expected to have very high mass-loss rate, of the order $\dot{M} \sim 10^{-5}$ $M_\odot$/yr (the new model presented in the next section predicts mass-loss rate even higher). As a results of this mass-loss rate, the envelope is stripped already in early phases and the star enters the WR phase; in the models presented here the star is considered WR when the hydrogen mass fraction at the surface drops below 0.3. In this phase, the star undergoes very strong mass-loss episodes, reducing its mass up to half of the initial mass in the more massive models. This translates in a reduction of the luminosity and a vertical evolution in the Hertzsprung-Russell (HR) diagram is expected as shown in Fig. 2.2, a typical feature of evolution dominated by mass-loss and convective mixing [7]. As for massive stars, the helium burning phase lasts about 10%-20% of the MS. Comparing the evolution of the 500 $M_\odot$ and 150 $M_\odot$ models, it is evident that both stars span more or less the same small range of temperature values in the O-type phase, but the 150 $M_\odot$ model increases its luminosity during the MS, in contrast to the 500 $M_\odot$ model. This is also more clear in the WR phase, when the luminosity of the 500 $M_\odot$ star steeply decreases. At the end of the He-burning, the stars move to the red and terminate their life at $\log(T_{\rm eff}/{\rm K}) \sim 4.5$, since the cores contract, releasing energy, and the envelopes expand.

Taking the rotation into account, there are only small differences with respect to the scenario just depicted, since the mass-loss still dominates the evolution. Indeed, the rotational mixing keeps the star more chemically homogeneous and also the less massive models have a vertical evolution in the HR diagram. In addition, the stars enter earlier the WR phase and lower luminosities are reached.

What mainly affects the evolution is the metallicity: at lower metallicities, the tracks are shifted to the red after the MS and reach higher luminosities as for massive stars and at Z = 0.002, the 300 $M_\odot$, 200 $M_\odot$ and 150 $M_\odot$ models experience an horizontal evolution in the HR diagram. The mass-loss rate scales with the metallicity, $\dot{M}({\rm Z}) = \dot{M}({\rm Z}_\odot)\left(\frac{Z}{Z_\odot}\right)^\alpha$, where $\dot{M}({\rm Z}_\odot)$ is the mass-loss rate at solar

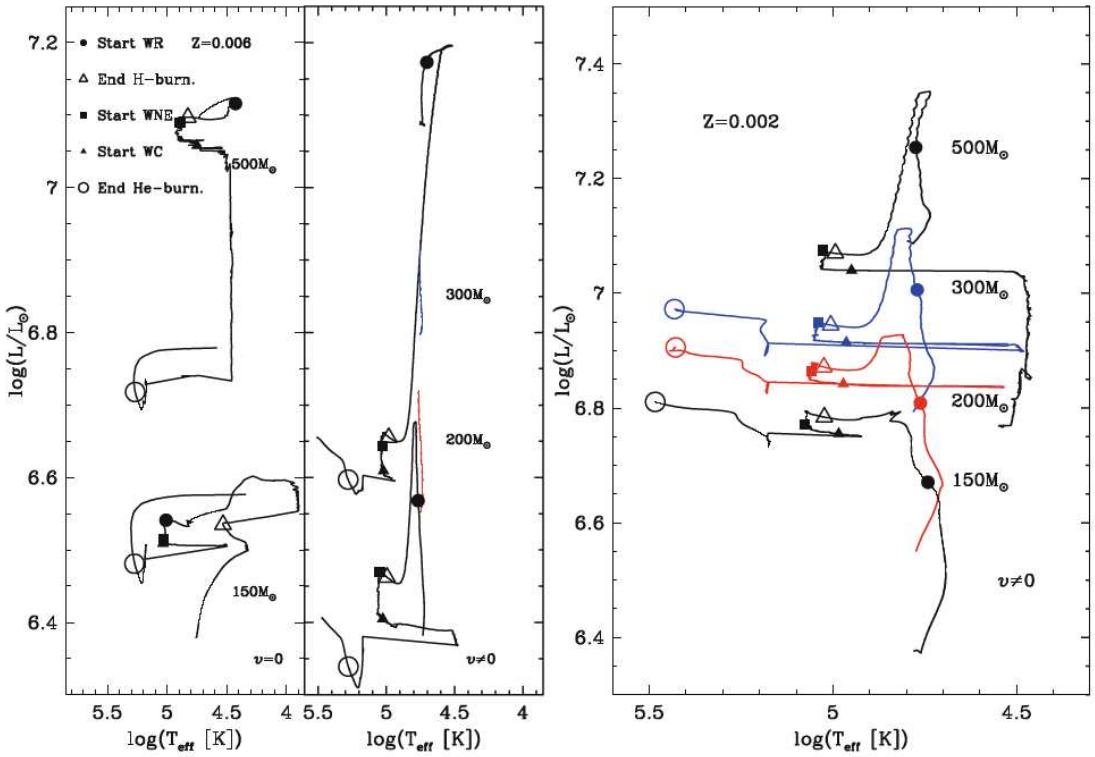

Figure 2.2: HR diagram for models between $M_{\rm init} = 150$ and $M_{\rm init} = 500$ $M_\odot$ at Z = 0.006 for non-rotating and rotating models, respectively, on the left. Rotating models at Z = 0.002 on the right. Key stages are indicated along the tracks: white triangles indicate the end of the H burning, white circles the end of the He burning, black circles the start of WR phase, black triangles the WR star of the carbon type, black squares the WR phase of the nitrogen type. [7].

metallicity, and the luminosity depends on the mass, $L \propto M^\delta$; so, this explains the different behaviour in the HR diagram.

The mass-loss rate plays a crucial role in VMSs. Fig. 2.3 shows the evolution of $\dot{M}$ as function of time: in the O-type phase, it is between 10^{-5} $M_\odot$/yr and $10^{-4.5}$ $M_\odot$/yr, while the highest value $\sim 10^{-3}$ $M_\odot$/yr is reached during the WR phase. A bi-stability limit is encountered in the MS, where the mass-loss rate can vary significantly in a very short period. The bi-stability limit refers to a phenomenon in which the mass-loss rate of a star experiences an increase or decrease as the star surface temperature crosses a certain threshold: when the surface temperature of a star decreases and crosses this threshold, the dominant ion in the wind-driving region of the star atmosphere can change, leading to a change in the mass-loss rate.

Another important parameter to understand VMSs is the Eddington parameter $\Gamma_{\rm Edd}$. The Eddington luminosity ($L_{\rm Edd}$) is the maximum luminosity a body can achieve in hydrostatic equilibrium and $\Gamma_{\rm Edd}$ is a dimensionless parameter indicating the degree to which a star is close to $L_{\rm Edd}$: $\Gamma_{\rm Edd} = L/L_{\rm Edd} = (k\,L)/(4\,\pi\,c\,G\,M)$, where L and M are the luminosity and mass of the star and k is the opacity. Since $\Gamma_{\rm Edd} \propto L/M$, an increase in the luminosity or a decrease in the mass result in an important change in its value. Vink et al. (2011 [8]) proposed an enhanced mass-loss rate for stars with $\Gamma_{\rm Edd} \geq 0.7$, close to the Eddington limit ($\Gamma_{\rm Edd} = 1$), which laid the basis for the stellar wind model presented in the next section. In the models shown in Fig. 2.4, there are two interesting cases in which $\Gamma_{\rm Edd} \geq 0.7$: the first one is the 150 $M_\odot$ model at $Z = 0.014$, where it happens in the advanced evolutionary phases and the mass-loss is less efficient (dashed blue line); the second one is the 150 $M_\odot$ model at $Z = 0.006$, where it happens already in the MS and the new wind prescription can have important consequence on the expected evolution (green solid line). These behaviours can result in strong mass ejections and have consequences on the fate of the stars.

To understand how VMSs end their life, the crucial parameter is the carbon-oxygen (CO) core mass. Many studies (Yoshida & Umeda 2011 [11], Yusof et al. 2013 [12], Woosley 2017 [14]) have shown that

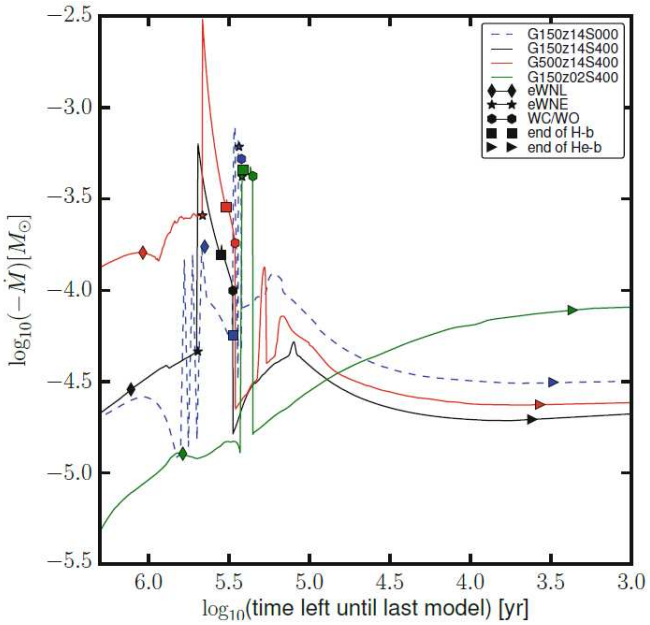

Figure 2.3: Evolution of the mass loss rate as a function of time left until last model (log scale) for the rotating $M_{\rm init}$ = 500 $M_\odot$ model (solid red), the rotating $M_{\rm init}$ = 150 $M_\odot$ model (solid black), the non-rotating (dashed) $M_{\rm init}$ = 150 $M_\odot$model at Z = 0.014, and the rotating $M_{\rm init}$ = 150 $M_\odot$ model at Z = 0.006 (solid green) [7].

most of them end their life with a CO core mass range between 60 and 130 $M_\odot$. They have an advanced evolution very similar to massive stars with masses 40-60 $M_\odot$: a radiative core C-burning followed by a large convective C-burning shell, radiative neon burning, and convective oxygen and silicon burning phases. All the solar metallicity models will eventually undergo core collapse after going through the usual advanced burning phases. An anti-correlation with the mass at the end of the helium burning is present: the higher temperature in more massive cores leads to a carbon-α $^{12}C(\alpha,\gamma)^{16}O$ reaction more efficient than the 3α one, reducing the fraction of carbon. At low metallicity, the mass-loss is weaker and the CO core bigger: this does not affect the evolution until the neon burning, but, after this phase, the stars enter the pair-instability regime (which is the topic of Chapter 3). Rotation still affects the expected mass in this phase, resulting in a lower total mass for rotating models [7].

2.1.2 Final Fate

In contrast to massive stars that undergo core collapse supernovae (CCSNe) at the end of the their life, VMSs are expected to experience different processes depending on mass and metallicity. VMSs near solar metallicity are expected to produce two types of CCSN: either a type Ib or type Ic supernova (SN), but no type II due to the fact that they lose the hydrogen envelope during their evolution [7]. SN classification is based on spectroscopic observations: type Ib SNe, by definition, are the ones that show strong helium absorption features; type II SNe are hydrogen-rich; type Ic SNe are defined by the absence of hydrogen and helium features. At lower metallicities, VMSs are expected to undergo pair-instability supernovae (PISNe) if the mass of the helium core is between 64 $M_\odot$ and 135 $M_\odot$ or pulsational pair-instability supernovae (PPISNe) if the mass of the helium core is between 32 $M_\odot$ and 64 $M_\odot$: the star can either explode leaving no compact remnants (PISN) or undergo strong mass ejections (PPISN), preventing the formation of black holes with masses between 60 $M_\odot$ and 120 $M_\odot$ (see Chapter 3 for a more detailed discussion).
For higher helium core masses, the star is expected to directly collapse in a black hole; so in the last part of this section, I talk about VMSs as progenitor of intermediate-mass black holes (IMBHs, 10^2 $M_\odot \leq M_{\rm IMBH} \leq 10^4$ $M_\odot$). Fig. 2.5 shows the expected compact remnants as function of the initial mass of the star and the metallicity and Fig. 2.6 shows the expected mass of the remnants as function of the initial mass of the stars at various metallicities. A gap in the distributions due to pair-instability is evident in both the plot, while VMSs with helium core mass greater than 135 $M_\odot$ are suitable candidates to explain the formation of IMBHs, one of most interesting and studied topic in

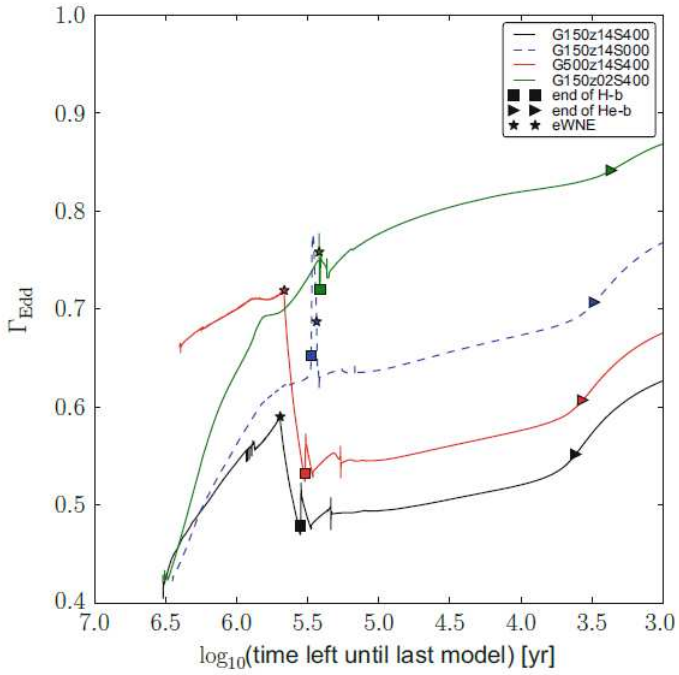

Figure 2.4: Evolution of the Eddington parameter as a function of time left until last model (log scale) for the rotating M_{ZAMS} = 500 $M_\odot$ model (solid red), the rotating M_{ZAMS} = 150 $M_\odot$ model (solid black), the non-rotating (dashed) M_{ZAMS} = 150 $M_\odot$ model at Z = 0.014, and the rotating 150$M_\odot$ model at Z = 0.006 (solid green) [7].

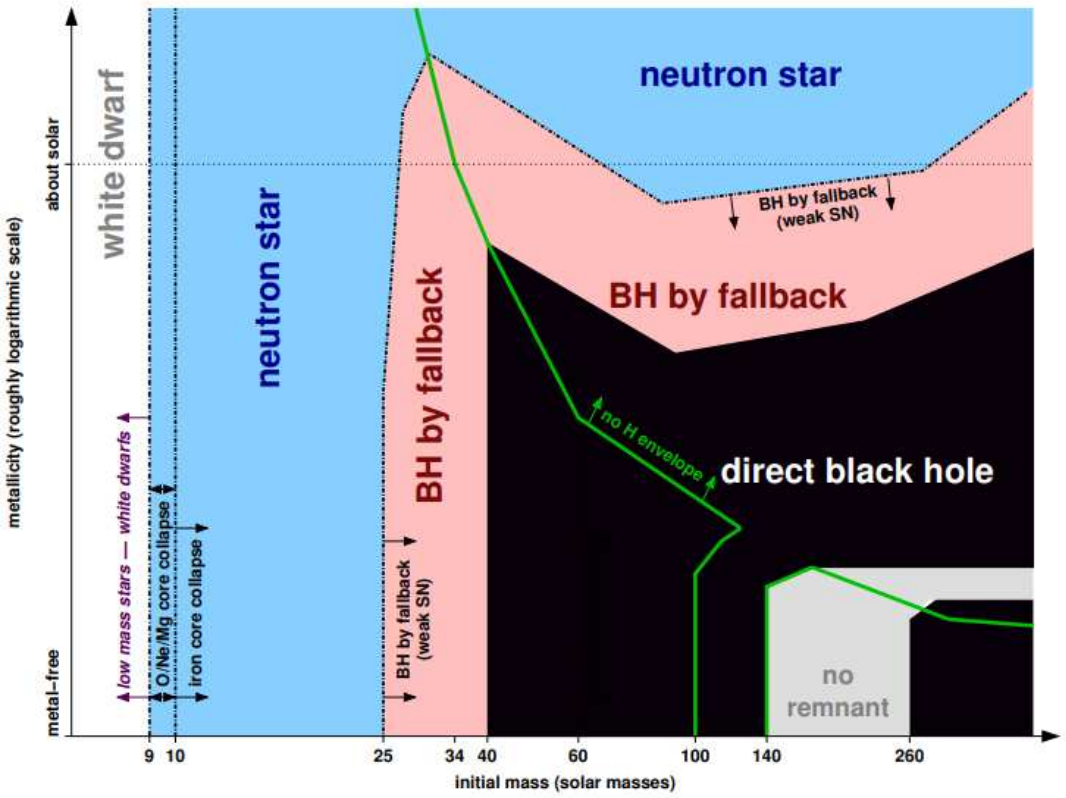

Figure 2.5: Scheme for compact remnants of single stars as a function of initial mass and metallicity: white dwarfs (white shading), neutron stars (light blue shading), black holes due to fallback after an initial explosions (light red shading), direct collapse (black shading), and a regime of no remnants (light gray shading). The green line shows where mass loss may remove the hydrogen-rich envelope prior to explosion of the star [9].

modern astrophysics. Several studies show that the formation of IMBHs needs two main ingredients: low metallicity and dynamics. Low metallicity is linked to the mass loss by stellar wind emission of the progenitor stars, as previously discussed, and is directly related to the final mass in the pre-supernova phase. Dynamics, instead, enhances the probability of close encounters that increases the chances for collisions: indeed, before collapsing, VMSs can merge and form more massive stars.
In Di Carlo et al. (2021 [13]), the formation of IMBHs in dense young star clusters via runaway collisions and binary mergers is investigated. To form the VMS (M_{star} = 439.7 $M_\odot$) which directly collapses in the most massive IMBH they found (M_{IMBH} = 437.9 $M_\odot$), the participation of 10 massive and very massive stars is needed. Also the other IMBHs formed via runaway collisions in their simulations have a similar path, involving multiple stellar mergers. Even if the mechanism driving stellar winds in VMSs is still not fully understood and there are many uncertainties related to the supernova mechanisms, many theoretical results suggest that the ideal progenitor of an IMBH is a VMS with $M_{star} \gtrsim 260\ M_\odot$ and $Z \lesssim 0.002$ to avoid pair-instability regime and strong mass-loss (Spera & Mapelli 2017 [10], Woosley 2017 [14], Marchant et al. 2019 [15], Heger et al. 2023 [9]).

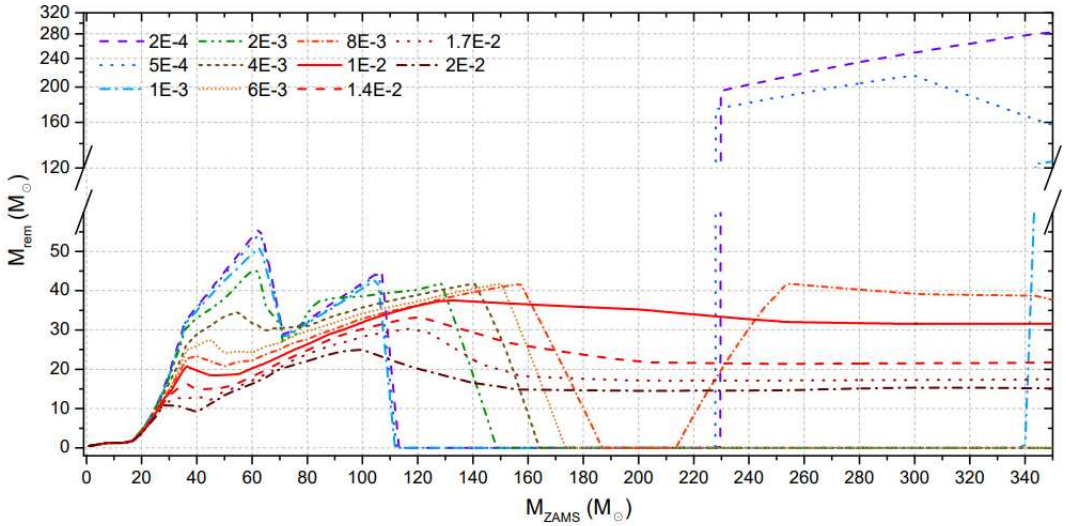

Figure 2.6: Mass of the compact remnant (M_{rem}) as a function of the zero-age main sequence (ZAMS) mass of the star (M_{ZAMS}). From bottom to top: dash-dotted brown line: $Z = 2.0 \times 10^{-2}$; dotted dark orange line: $Z = 1.7 \times 10^{-2}$; dashed red line: $Z = 1.4 \times 10^{-2}$; solid red line: $Z = 1.0 \times 10^{-2}$; short dash-dotted orange line: $Z = 8.0 \times 10^{-3}$; short dotted light orange line: $Z = 6.0 \times 10^{-3}$; short dashed line: $Z = 4.0 \times 10^{-3}$; dash-double dotted line: $Z = 2.0 \times 10^{-3}$; dash-dotted light blue line: $Z = 1.0 \times 10^{-3}$; dotted blue line: $Z = 5.0 \times 10^{-4}$; dashed violet line: $Z = 2.0 \times 10^{-4}$ [10].

2.1.3 Observed Properties of Very Massive Stars

VMSs have been observed in the Local Universe and the interest in them has grown in the last decades. In Tab. 2.1 the most massive observed stars are listed and in Fig. 2.7 the image of the central part of the Tarantula Nebula (or 30 Doradus) is reported, which contains the cluster R136 with stars of masses 135 $M_\odot$, 175 $M_\odot$, 195 $M_\odot$ and 265 $M_\odot$ (Crowther et al., 2010 [16]). Their spectral analysis is not similar to that of an absorption-line dominated O-star spectrum but to the one of an emission-line dominated WNh star spectrum (WR star of the nitrogen type with left-over hydrogen in their spectra). Such WNh stars are likely still on the H-burning MS with an enhanced mass-loss rate (Martins & Palacios, 2022 [17]). In addition, two main aspects related to the temperature are observed. VMS temperatures are enclosed in a narrow range of values:

- $\log(T_{eff}/K) \sim 4.5$ in the Arches cluster at super-solar metallicity (Martins et al., 2008 [19]);
- $\log(T_{eff}/K) \sim 4.62$ in NGC 3603 (Crowther et al., 2010 [16]);
- $\log(T_{eff}/K) \sim 4.7$ in the 30 Doradus cluster (Bestenlehner et al., 2014 [20]);

Name	Mass ($M_\odot$)	Location
R136a1	264 (320)	LMC
R136a2	195	LMC
R136c	175	LMC
Peony star (WR 102ka)	175 (WR)	MW
HD 269810	150	LMC
VFTS 682	150 (WR)	LMC
R136a3	135	LMC
NGC 3603-B	132	MW
Arches-F9	120 (WN)	MW
η Carina-A	120 (160)	MW

Table 2.1: List of the most massive stars observed. The numbers in parentheses, following the current mass, stand for the estimated initial masses. WR, WN, MW and LMC mean respectively Wolf-Rayet star, Wolf-Rayet of type WN, Milky Way and Large Magellanic Cloud (Kozyreva, 2014 [18]).

- $\log(T_{\rm eff}/{\rm K}) \sim 4.72$ in R136 (Crowther et al., 2010 [16]).

Figure 2.7: The image shows the central region of the Tarantula Nebula in the Large Magellanic Cloud. The young and dense star cluster R136 can be seen at the lower right of the image. This cluster contains hundreds of young blue stars, among them the most massive star detected in the Universe so far (Credit: NASA/ESA/P. Crowther, University of Sheffield).

Then, the temperature distribution suggests an important temperature-metallicity correlation with VMS having higher temperatures at lower Z. The temperature distribution of VMSs could be an interplay between the effects of Z and the age of the cluster, but a consistent trend with Z might hint towards a dominant Z effect.
The vertical alignment of the observed temperatures of stars could just be due to a burst of star formation, with the massive stars in the cluster all at the same age, but the situation is more complicated for VMSs. They are subjected to substantial envelope inflation and this implies that the most massive stars will inflate to lower $T_{\rm eff}$ than the less massive stars in the cluster; an higher mass loss might reduce or offset this effect. Existing VMS models fail to explain the observed features and various corrections have been implemented to avoid inflation at low temperature (see discussion about the mixing length theory in the stellar evolution code MESA in Section 4.1.1). This is the reason why a new model for the stellar winds and a deeper comprehension of the mass-loss mechanisms are necessary.

2.2 A New Model for the Stellar Winds

Stellar winds are streams of plasma ejected from the outer layers of the stars. The hydrodynamic equation of motion relates the acceleration of motion to the forces acting in the wind and, under the assumption of stationarity $\frac{dv}{dt} = 0$, it takes the form:

$$v\,\frac{d\,v}{d\,r} = -\frac{G\,M}{r^2} - \frac{1}{\rho}\,\frac{d\,P}{d\,r} + a(r)\,, \tag{2.3}$$

where the term on the left-hand side is the inertial term, the first term on the right-hand side is the gravitational term, the second one is the acceleration due to gas pressure and $a(r)$ can represent any additional force. If a force is added below the sonic point $R_{\rm sonic}$ (where $v = c_s$), this results in a higher mass-loss rate; on the other hand, if the additional force acts beyond this point, it results in a higher wind velocity. In this discussion, the sonic point $R_{\rm sonic}$ coincides with the critical point $R_{\rm crit}$ of the equation of motion, the point in which the denominator of the equation of motion is zero. In O-type stars, the key additional force term is due to the radiative force on line opacity. In the Sobolev approximation, which assumes that local variations in the velocity gradient are negligible compared to variations over longer lengths, the radiative acceleration $a_{\rm rad}$ of one line is given by the following expression:

$$a_{\rm rad} = \frac{F_{\nu_0}\,\nu_0}{c}\left\{1 - e^{-\tau_{\nu_0}}\right\}\frac{d\,v}{d\,r}\,\frac{1}{c\,\rho}\,, \tag{2.4}$$

where F_{ν_0} is the monochromatic flux emitted at the line rest frequency ν_0, $\frac{\nu_0}{c}\,\frac{dv}{dr}$ is the width of the frequency band that can be absorbed, $\left\{1 - e^{-\tau_{\nu_0}}\right\}$ is the probability that absorption occurs and τ_{ν_0} is the optical depth (Lamers & Cassinelli, 1999 [21]). Castor et al. (1975, [22]) proposed to parameterise the contribution of an ensemble of lines a_L as follows:

$$a_L = a_e\,M(j)\,, \tag{2.5}$$

$$a_e = \frac{k_e}{c}\,\frac{L}{4\,\pi\,r^2} = \Gamma_{\rm Edd}\,\frac{G\,M}{r^2}\,, \tag{2.6}$$

$$M(j) \equiv k\,j^{-\alpha}\,s^{\delta}\,, \tag{2.7}$$

where a_e is the acceleration due to electron scattering with opacity coefficient k_e, $M(j)$ is called force multiplier, k, α, δ are the force multiplier parameters, $j \sim \rho\,\frac{dr}{dv}$ is the optical depth parameter and s describes the ratio between the characteristic particle density and some normalization factors. In particular, α can vary from 0 (optically-thin lines) to 1 (optically-thick lines). This is known as CAK (Castor-Abbott-Klein) theory and the equation of motion, taking the contribution by a_L into account, can be solved analytically. It predicts a β-law for the velocity, with $\beta \sim$ 0.5-0.7, and a mass-loss rate which depends on the force multiplier parameters k and α and on the Eddington parameter:

$$v(r) = v_\infty\left(1 - \frac{R_\star}{r}\right)^{\beta}, \tag{2.8}$$

$$\dot{M} \propto (k\,L)^{1/\alpha}\,M\,(1 - \Gamma_{\rm Edd})^{1-1/\alpha}\,, \tag{2.9}$$

where v_∞ is the terminal velocity asymptotically attained, $v_\infty = v(r \to \infty)$. The evolution of a_L (called $g^{\rm line}$ in the plot) as function of the radius is shown in Fig. 2.8. Nevertheless, the CAK theory cannot well explain optically-thick winds observed in the WR phase of VMSs.
The current state-of-the art relies on either the Lambert W function in which the radiative acceleration is determined by Monte Carlo methods (Müller & Vink, 2008 [24]) or on direct integration of the radiative acceleration in the co-moving frame:

$$a_{\rm rad} = \frac{1}{c}\int k_\nu\,F_\nu\,d\,\nu\,, \tag{2.10}$$

where k_ν is the frequency-dependent opacity and F_ν the flux. Since the degree of ionisation decreases as function of the radius going outwards, photons can interact with different sources of opacity, such as

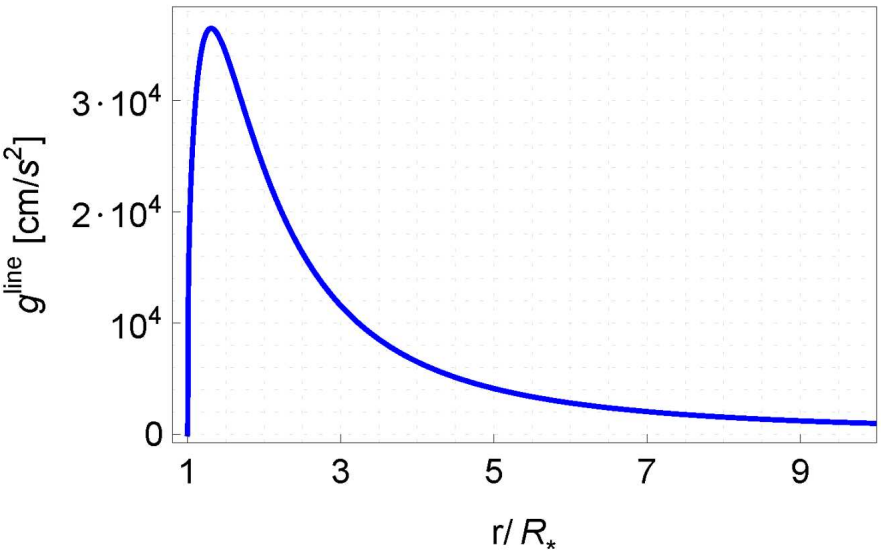

Figure 2.8: The radiative acceleration g_{line} ($a_L \equiv g_{\rm line}$) for a typical O star without rotation as function of $r/R_\star$, for $r < 10\ R_\star$ (Curé & Araya, 2023 [23]).

Fe and other relevant ions, in their path through the atmosphere. So, gaps between the spectral lines are filled leading to a layered ionisation structure. The instauration of classical WR winds depends on the condition that they become optically-thick at the critical radius and that the line acceleration due to the high opacity is able to balance the gravity force, driving an optically-thick wind (Nugis & Lamers, 2002 [25]). The key point of this analysis is that, due to their very high mass-loss rates, the atmospheres become so dense that the wind sonic point is reached at very high flux-mean optical depth and the radiation can be treated in the diffusion limit, obtaining the following expression for the radiative acceleration:

$$a_{\rm rad} \sim k_{\rm Ross} \frac{L}{4\,\pi\,r^2\,c}\,, \tag{2.11}$$

where k_{Ross} is the Rosseland mean opacity. The diffusion approximation is valid when the ratio α of the collision mean free path λ to the characteristic length Λ of the considered phenomenon is small and, simultaneously, the ratio of the mean time between collisions to the characteristic time scale is of order α^2; both these conditions are satisfied in the optically-thick case. However, it is more convenient to consider the Eddington parameter in the following form:

$$\Gamma_{\rm Edd}(r) = \frac{\varkappa_F(r)}{4\,\pi\,c\,G}\,\frac{L}{M}\,, \tag{2.12}$$

where $\varkappa_F(r)$ is the flux-weighted mean opacity, which approaches k_{Ross} in the deepest atmospheric layers (Fig. 2.9). The modelling of an appropriate wind stratification involves an accurate calculation of $\varkappa_F(r)$ through the entire atmosphere, from the deep optically-thick layers to the outer optically-thin regions (Vink, 2024 [27]).
Thus far, the majority of stellar evolution models employs the prescription for the stellar winds by Vink et al. (2001, [4]) for the O-type stars, which includes dependecies on the temperature and on the metallicity:

$$\begin{aligned}\log \dot{M} = -6.697 + 2.194\,\log\Big(\frac{L}{10^5\,{\rm L}_\odot}\Big) - 1.313\,\log\Big(\frac{M}{30\,{\rm M}_\odot}\Big) - 1.226\,\log\Big(\frac{v_\infty}{2\,v_{\rm esc}}\Big) \\ +0.933\,\log\Big(\frac{T_{\rm eff}}{40000}\Big) - 10.92\Big[\log\Big(\frac{T_{\rm eff}}{40000}\Big)\Big]^2 + 0.85\log\Big(\frac{Z}{Z_\odot}\Big)\,,\end{aligned} \tag{2.13}$$

where $v_{\rm esc} = \big(\frac{2\,G\,M}{R_{\rm crit}}\big)^{1/2}$ and $R_{\rm crit}$ is the critical point. However, there are still many uncertainties on the quantitative mass-loss rate and stellar winds of VMSs have been predicted and observed to be boosted in the optically-thick regime (Vink et al. 2011 [8], Bestenlehner et al. 2014 [20]).

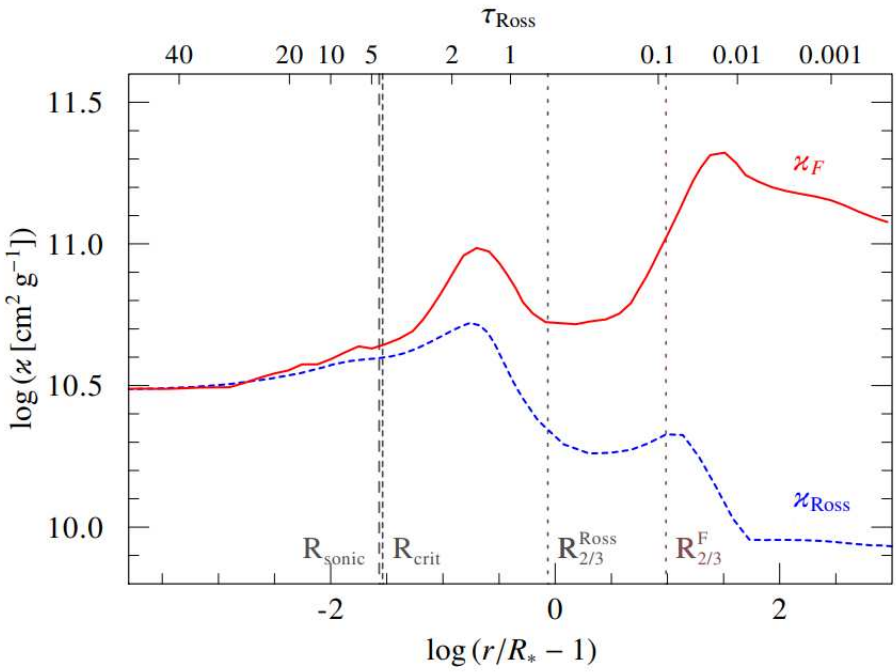

Figure 2.9: Comparison of the flux-weighted mean opacity (red, solid) to the Rosseland mean opacity (blue, dashed) in an atmosphere model for a hydrogen-free WN star at solar metallicity (Sander et al., 2020 [26]). Sander et al. adopted different definitions of $R_{\rm sonic}$ and $R_{\rm crit}$ from the ones I used: here $R_{\rm sonic} \equiv R(v = c_s)$, where c_s is the sound speed; $R_{\rm crit} \equiv R(v = a)$, where a is the critical point the equation of motion including a micro-turbulence term in the velocity. However, the fact that $\varkappa_F$(r) approaches $k_{\rm Ross}$ in the deepest atmospheric layers does not depend on these definitions.

2.2.1 Transition Mass Loss

Vink & Gräfener (2012 [28]) introduced the concept of transition mass-loss to properly calibrate the mass-loss rate and characterise the switch from an optically-thin to an optically-thick wind in VMSs. In this section, I strictly follow their work to reproduce their result.
Assuming stationary winds, the Eq. 2.3 can be integrated from the inner boundary R to infinity, passing through the sonic point $R_{\rm sonic}$:

$$\begin{aligned} &\int_R^\infty 4\pi r^2 \rho v \frac{dv}{dr} dr + \int_R^{R_{\rm sonic}} 4\pi r^2 \Big[\frac{1}{\rho}\frac{dP_{\rm gas}}{dr} + \frac{GM}{r^2}\Big] dr + \\ &+ \int_{R_{\rm sonic}}^\infty 4\pi r^2 \frac{1}{\rho}\frac{dP_{\rm gas}}{dr} dr + \int_{R_{\rm sonic}}^\infty 4\pi r^2 \rho \Big[\frac{GM}{r^2} - a(r)\Big] dr = 0 . \end{aligned} \tag{2.14}$$

In the sub-sonic region, the hydrostatic equilibrium is a good approximation and the second term in the equation above is negligible; in addition, also the gas pressure force can be considered negligible in the super-sonic region and we disregard the third term. The first term, instead, is the momentum in the wind: $\dot{M} v_\infty$. Considering the Eddington parameter in form of Eq. 2.12, the integrated equation of motion reduces to:

$$\dot{M} v_\infty = 4\pi G M \int_{R_{\rm sonic}}^\infty \big(\Gamma_{\rm Edd}(r) - 1\big) \rho \, dr . \tag{2.15}$$

Then, using the total Eddington parameter and the flux-weighted mean optical depth at the critical point $\tau_{F,s} = \int_{R_{\rm sonic}}^\infty \varkappa_F \rho \, dr$, the above equation can be expressed in a simpler form:

$$\dot{M} v_\infty = \frac{L}{c}\Big(\frac{\Gamma_{\rm Edd} - 1}{\Gamma_{\rm Edd}}\Big)_{\rm avg} \tau_{F,s} . \tag{2.16}$$

In the limiting case of $\Gamma_{\rm Edd} \gg 1$, this leads to the two equivalent relations:

$$\eta = \tau_{F,s} = 1 \, , \; \dot{M}_{\rm trans} = \frac{L_{\rm trans}/c}{v_{\infty,\rm trans}} , \tag{2.17}$$

where $\eta = \frac{\dot{M}\, v_\infty}{L/c}$ is the efficiency of the wind and $\dot{M}_{\rm trans}$, $L_{\rm trans}$ and $v_{\infty,\rm trans}$ are the mass-loss rate, the luminosity and the terminal velocity at the transition point. The validity of assuming $\Gamma_{Edd} \gg 1$ has been tested using the PoWR code (Gräfener et al. 2002 [29], Hamann & Gräfener 2003 [30], Sander et al. 2015 [31]) and Vink & Gräfener found a correction factor $f \sim 0.6$ in their Galactic models:

$$\eta = f\, \tau_{F,s} = f\ ,\ \dot{M}_{\rm trans} = f\, \frac{L_{\rm trans}/c}{v_{\infty,\rm trans}}\,. \tag{2.18}$$

Finally, Eq. 2.18 can be used to estimate the transition mass-loss rate. This computation has been done to predict the transition mass-loss rate in the two Of/WNh stars in the Arches cluster and they found $\log(\dot{M}_{\rm trans}) \sim -5.16$ M$_\odot$ yr^{-1}, which is in good agreement with the empirically determined $\log(\dot{M}_{\rm emp}) \sim -5.19$ M$_\odot$ yr^{-1}. How the variation of different stellar parameters can affect the value of f has been tested: changing luminosity and temperature does not significantly impacts its value, while it mainly depends on the ratio $v_\infty/v_{\rm esc}$.

2.2.2 Mass Loss Implementation

Since the importance of the mass-loss increases with the mass of the stars, it is vital to implement accurate optically-thick wind models in the evolution of VMSs. Vink et al. (2011, [8]) investigated the winds of stars with masses up to 300 M$_\odot$ and they found a kink in the mass-loss rate as function of $\Gamma_{\rm Edd}$. Below the kink, they found a good agreement with the approach in Vink et al. (2001, [4]); while beyond the kink, the mass-loss rate steeply depends on $\Gamma_{\rm Edd}$. Considering Thomson acceleration and a fully ionized gas, $\Gamma_{\rm Edd}$ and $\dot{M}$ can be expressed as follows:

$$\Gamma_{\rm Edd} = \frac{\varkappa_{\rm Thom}}{4\,\pi\, G\, c}\,\frac{L}{M} \sim 10^{-4.813}\,(1+X_s)\,\frac{L}{M}\,, \tag{2.19}$$

$$\dot{M}_{\Gamma_{\rm Edd}} \propto M^{0.78}\,\Gamma_{\rm Edd}^{4.77} \propto \frac{(1+X_s)^{4.77}\,L^{4.77}}{M^{3.99}}\,, \tag{2.20}$$

where X_s is the surface hydrogen abundance.
In Sabhahit et al. (2022, [32]), they investigated two different dependencies of the mass-loss rate to understand the relative importance of X_s. Exploiting the concept of transition mass-loss, they derived a recipe for the mass-loss rate that involves the one predicted by Vink et al. (2001, [4]) in the low-$\Gamma_{\rm Edd}$ regime ($\Gamma_{\rm Edd} < 0.4$) and, in the high-$\Gamma_{\rm Edd}$ one, they proposed the following models which depend either on $\Gamma_{\rm Edd}$ (and consequentially on X_s; Eq. 2.21) or only on L/M (Eq. 2.22):

$$\begin{aligned}\log\,\dot{M}_{{\rm high},\Gamma_{\rm Edd}} = -9.552 + 4.77\,\log(1+X_s) + 4.77\log\Big(\frac{L}{10^5\,{\rm L}_\odot}\Big) + \\ -3.99\,\log\Big(\frac{M}{30\,{\rm M}_\odot}\Big) - 1.226\,\log\Big(\frac{v_\infty}{2\,v_{\rm esc}}\Big) + 0.5\,\log(\frac{Z}{Z_\odot})\,,\end{aligned} \tag{2.21}$$

$$\begin{aligned}\log\,\dot{M}_{{\rm high},L/M} = -8.445 + 4.77\log\Big(\frac{L}{10^5\,{\rm L}_\odot}\Big) - 3.99\,\log\Big(\frac{M}{30\,{\rm M}_\odot}\Big) + \\ -1.226\,\log\Big(\frac{v_\infty}{2\,v_{\rm esc}}\Big) + 0.5\,\log(\frac{Z}{Z_\odot})\,.\end{aligned} \tag{2.22}$$

Notice that both the models predict a mass-loss rate higher than the canonical O-type star rate and a lower dependence on the metallicity. Using the 1D stellar evolution code MESA (version r12115, Paxton et al. 2011 [33], 2013 [34], 2015 [35], 2018 [36], 2019 [37]), they modeled stars with masses ranging from 60 up to 500 M$_\odot$ at Z = 0.02 (solar metallicity) and Z = 0.008 (Large Magellanic Cloud metallicity). The stellar parameters at the transition are reported in Tab. 2.2. The two recipes represent different extreme cases (strong or no dependence on X_s) and, even if the absolute mass-loss rate slightly changes, they translate in opposite behaviours in the HR diagram as shown in Fig. 2.10: the $\Gamma_{\rm Edd}$-models move to the red, while L/M-models evolve in a very narrow range of temperature decreasing in the luminosity. In addition, the inflation effect is much lower in the models not moving to the red (see discussion in Section 2.1.3). Summarizing, vertical evolution where the luminosity drops

	$\log(L/L_\odot)$	v_∞ (km/s)	$T_{\rm eff}$ (K)	X_s	$\log \dot{M}$	$M/\mathrm{M}_\odot$	$\Gamma_{\rm Edd}$
GAL	6.06	2000	33900	0.7	-5.16	76.9	0.39
LMC	6.31	2550	44400	0.62	-5.0	121.8	0.42

Table 2.2: Transition parameters of Of/WNh stars from Arches cluster in the Galaxy (GAL) and 30 Dor cluster in the Large Magellanic Cloud (LMC). The transition luminosities, effective temperatures and X_s are obtained empirically, and used to evaluate the transition mass-loss rate and the $\Gamma_{\rm Edd,\ trans}$ [32].

steeply can naturally account for constant temperatures of VMSs by self-regulating and balancing the effect of mass loss and inflation throughout the evolution and can also explain the trend in the temperature as function of Z.

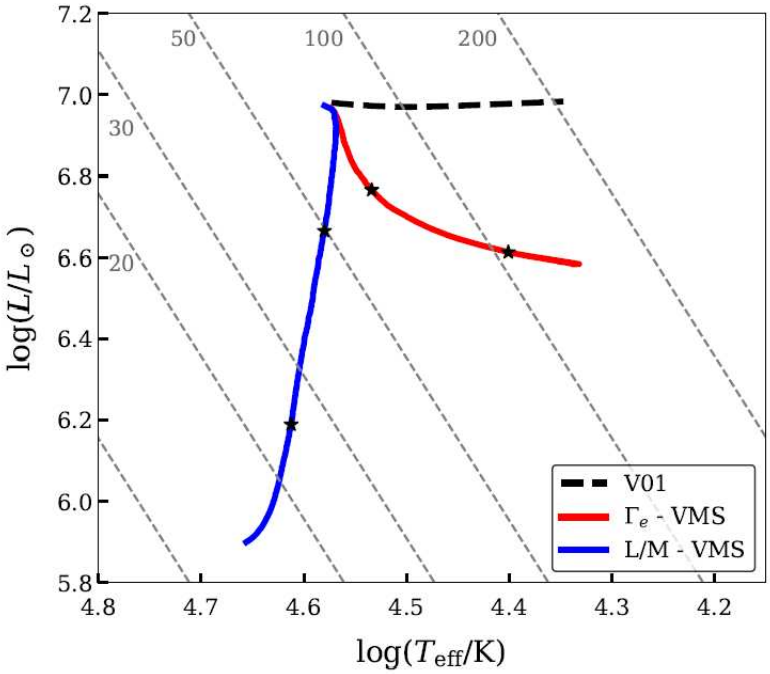

Figure 2.10: Comparison of 400 $\mathrm{M}_\odot$ VMS main sequence evolution using different mass-loss dependencies on the stellar properties: $\dot{M}_{\rm high,\Gamma_{Edd}}$ (Eq. 2.21; blue line), $\dot{M}_{{\rm high},L/M}$ (Eq. 2.22; red line), $\dot{M}_{\rm Vink}$ (Eq. 2.20; dashed black line). Black star symbols mark the ages 1 and 2 Myr along the stellar track. The grey dashed lines are the constant radius lines and the numbers represent the radius in terms of $\mathrm{R}_\odot$. [32]

2.2.3 Mass Loss Framework at low Metallicities

In a second paper, Sabhahit et al. (2023, [38]) proposed a way to extend the model presented in the previous section to low metallicity, where we do not have available data to constrain the mass-loss rate. In order to investigate PISNe and PPISNe, it is crucial to model the evolution of VMSs at low metallicities, where the mass-loss is less efficient and VMSs can have massive He- and CO-core and enter the pair-instability regime.
As previously discussed, VMSs have a uniform chemical composition: given a range of luminosities $L\,(L = 10^5 - 10^8\ \mathrm{L}_\odot)$ and a fixed surface hydrogen abundance X_s, the related masses $\mathrm{M}_{\rm hom}$ can be computed under the assumption of homogeneity from the mass-luminosity relations (Gräfener et al., 2011 [39]). The mass-loss rate $\dot{M}_{\rm Vink}$ can be computed from Eq. 2.13, fixing the metallicity; in Sabhahit et al. (2023 [38]), they did not include the temperature dependency, since Monte Carlo models show almost no variation of $\dot{M}$ with the effective temperature above 60 $\mathrm{M}_\odot$ (Vink & Sander, 2021 [40]). The terminal velocity can be estimate with the following formula:

$$v_\infty = 2.6 \sqrt{\frac{2\,G\,M_{\rm hom}\,(1-\Gamma_{\rm Edd}(L))}{R}} \left(\frac{Z}{Z_\odot}\right)^{0.2}, \tag{2.23}$$

where R is obtained from the Stefan-Boltzmann law. Now, it is possible to compute the wind efficiency parameter:

$$\eta_{\rm Vink} \equiv \eta(\dot{M}_{\rm Vink}) = \frac{\dot{M}_{\rm Vink}\, v_\infty}{L/c}\,. \tag{2.24}$$

To obtain the correction parameter f, the following parametric formula can be used:

$$f = \frac{\eta}{\tau_{F,s}}\left(\frac{v_\infty}{v_{esc}}\right) \sim \left(1 + \frac{v_{esc}^2}{v_\infty^2}\right)^{-1}. \tag{2.25}$$

When $\eta_{\rm Vink} = \frac{\eta}{\tau_{F,s}}$, the transition happens. The variation of wind efficiencies and cross-over points as function of the luminosity at different metallicities is shown in Fig. 2.11: the higher the metallicity, the lower the luminosity required to reach the transition point. These equations can be satisfied to obtain the luminosity $L_{\rm switch}$ and the mass $M_{\rm switch,\ hom}$ at the cross-over and, finally, compute $\Gamma_{\rm Edd,switch}$; the wind efficiency in this point is defined as $\eta_{\rm switch} \equiv \eta_{\rm Vink}(L_{\rm switch})$.

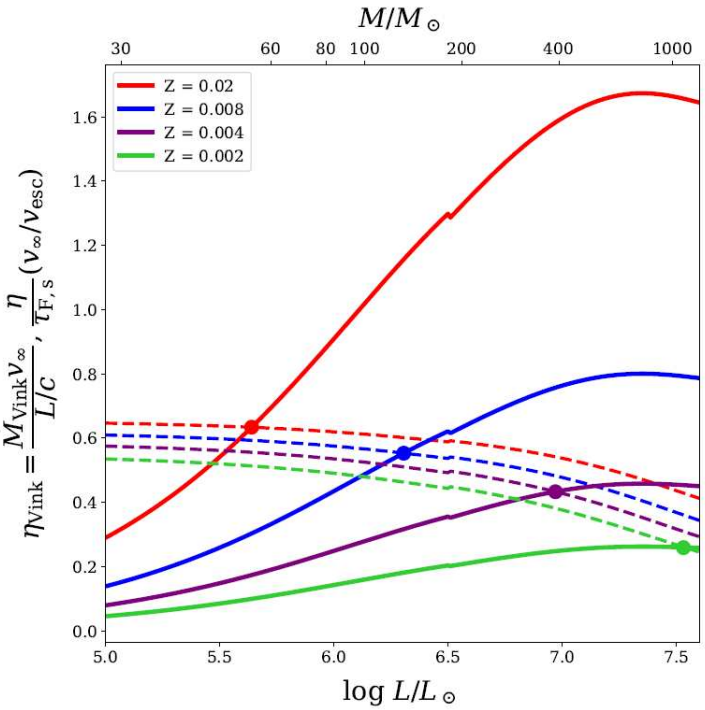

Figure 2.11: Variation of wind efficiency parameter as a function of luminosity (solid lines). The dashed lines show the variation of the parametric form of f. Different colors represent different metallicities ranging from Z = 0.02 to 0.002. The location where a solid and dashed line cross denotes the transition on the zero-age main sequence at that corresponding metallicity. The small wiggle in the plots at $\log(L/L_\odot) = 6.5$ is due to switch in the mass-luminosity relation adopted from Gräfener et al. (2011 [39]) [38].

As in the case of solar and LMC metallicity, the implementation at low metallicity is divided into two parts:

- for the low-$\Gamma_{\rm Edd}$ ($\Gamma_{\rm Edd} \leq \Gamma_{\rm Edd,\ switch}$) regime, the absolute mass-loss rate is $\dot{M}_{\rm low-\Gamma_{Edd}} = \dot{M}_{\rm Vink}$;
- for the high-$\Gamma_{\rm Edd}$ ($\Gamma_{\rm Edd} \geq \Gamma_{\rm Edd,\ switch}$) regime, the absolute mass-loss rate is enhanced according to: $\dot{M}_{\rm high-\Gamma_{Edd}} = \dot{M}_{\rm switch} \times \left(\frac{L}{L_{\rm switch}}\right)^{4.77}\left(\frac{M}{M_{\rm switch}}\right)^{-3.99}$.

The reason of such an implementation is that it predicts an higher mass-loss rate. The evolution of $\dot{M}$ as function of the Eddington parameter is shown in Fig. 2.12.
The new framework is robust and solves some of the problems in VMS evolution. However, $M_{\rm switch,\ hom}$ is the maximum obtainable mass given $L_{\rm switch}$ and this can lead to an over-prediction of the mass-loss rate. Then, the crucial condition to model the transition from optically-thin to optically-thick winds is $\eta_{\rm Vink} = \frac{\eta}{\tau_{F,s}}$; so, any over- or under-prediction of these parameters affects the final result.

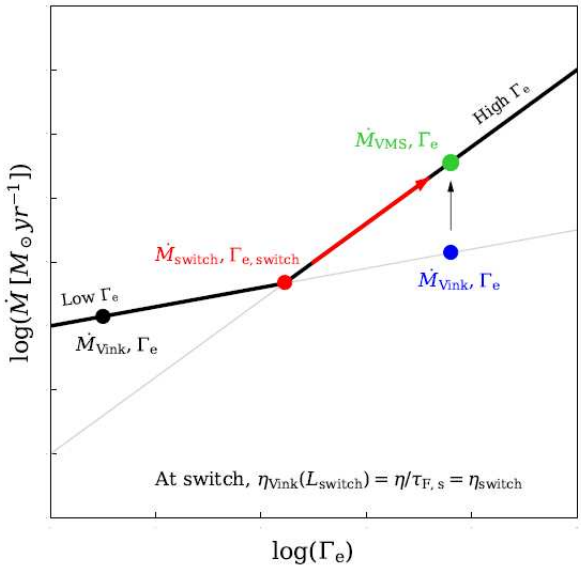

Figure 2.12: Schematic representation of the new VMS mass-loss framework where the condition to switch to a high-$\Gamma_{\rm Edd}$, optically-thick wind is based on wind efficiency parameters. [38].

2.3 Binary Evolution

The vast majority of VMSs are formed in binary or higher order systems (Sana et al. 2012 [41]). Populations of O-type stars in six nearby Galactic open clusters have been studied thanks to spectroscopic observations: 71% of them interact with a companion and more than half of them do it already in the MS. In addition, 20%-30% of them merge with their companion and 40%-50% of them accrete a large amount of mass or are stripped of their envelope. So, it is clear that binary evolution drastically changes the evolution of VMSs and their fate. The two most important parameters to describe a binary system are the mass-ratio $q = M_2/M_1$, where M_1 is the mass of the more massive star and M_2 the one the less massive star, and the orbital period $P_{\rm orb}$, which can span a vast range of value depending on the objects in the system. To have a complete view of the evolution of VMSs, it is then fundamental to analyze also binary systems. I discuss mass transfer and common envelope episodes in the next sections.

2.3.1 Mass Transfer and Roche-lobe Overflow

Stars undergo mass transfer episodes if they exchange matter to each other; it may be driven by stellar winds or Roche-lobe overflow (RLOF).
When a massive star loses mass by stellar winds, the companion can capture some of this mass. Based on the Bondi-Hoyle mechanism, spherical accretion in which the matter falls radially onto the accreting object from all the directions (1944, [42]), Hurley et al. (2002, [43]) described the mean mass accretion rate due to stellar winds:

$$\dot{M}_2 = \frac{1}{\sqrt{1-e^2}} \left(\frac{G\,M_2}{v_w^2}\right)^2 \frac{\alpha_w}{2\,a^2} \frac{1}{[1+(v_{\rm orb}/v_w)^2]^{3/2}} \,|\dot{M}_1|\,, \tag{2.26}$$

where e is the binary eccentricity, M_2 is the mass of the accreting star, v_w is the velocity of the wind, $\alpha_w \sim 3/2$ is an efficiency constant, a is the semi-major axis, $v_{\rm orb}$ is the orbital velocity of the binary and $\dot{M}_1$ is the mass-loss rate of the donor. The Bondi-Hoyle mechanism is usually not efficient due to a geometrical reason: the donor star ejects mass over all the solid angle and only a small fraction of it falls onto the accreting star.
A crucial and more efficient mechanism is the Roche-lobe overflow. To introduce it, let me consider the so-called restricted three-body problem, where the motion of a mass-less test particle in the gravitational potential of two orbiting masses is followed. The best reference frame to describe this system is the one co-rotating with the binary and, after a change of coordinates, the following effective

potential, called Roche potential, can be defined:

$$\phi_R = -\frac{G\,(M_1+M_2)}{2\,a}\left\{\frac{2}{1+q}\,\frac{1}{\sqrt{x^2+y^2+z^2}}+\frac{2q}{1+q}\,\frac{1}{\sqrt{(x-1)^2+y^2+z^2}}+\left[\left(x-\frac{q}{1+q}\right)^2+y^2\right]\right\}, \tag{2.27}$$

which depends only on the mass ratio q and the semi-major axis a. The first two terms are related to the gravitational potentials of the two objects in the binary and the last one to a fictitious centrifugal term due to the fact we are not considering an inertial frame. This potential has five points of equilibrium, called Lagrangian points, that are shown in Fig. 2.13. The Roche-lobe of a star in a binary system is a teardrop-shaped equipotential surface surrounding the star. If the donor star fills its Roche-lobe during its evolution, the matter can be transferred to the other star through the inner Lagrangian point L_1. For circular orbit, the Roche-lobe radius R_L is well approximated by the following expression (Eggleton, 1983 [45]):

$$R_L = \frac{0.49\,q^{-2/3}}{0.6\,q^{-2/3}+\ln\left(1+q^{-1/3}\right)}\,a. \tag{2.28}$$

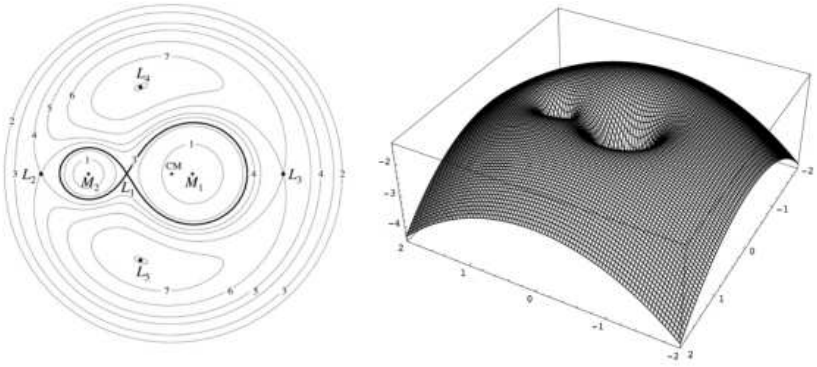

Figure 2.13: Equipotential surfaces (right) and lines (left) of the Roche potential ϕ_R (Eq. 2.27) and the Lagrangian points (Lauer 2017 [44]).

A crucial information about RLOF is whether it is stable or not. Assuming $R \propto M^{\zeta}$ [43], the time variation of the donor's radius during RLOF is:

$$\frac{d\,R_1}{d\,t} = \frac{\partial\,R_1}{\partial\,t} + \zeta\,\frac{R_1}{M_1}\,\frac{d\,M_1}{d\,t}\,, \tag{2.29}$$

the term $\frac{\partial R_1}{\partial t}$ is due to nuclear burning and ζ measures the adiabatic or thermal response of the donor star to mass loss; $\frac{d M_1}{d t}$ represents the mass lost by the donor, so it is always negative. Similarly, the change of the Roche-lobe radius is:

$$\frac{d\,R_{L,1}}{d\,t} = \frac{\partial\,R_{L,1}}{\partial\,t} + \zeta_L\,\frac{R_{L,1}}{M_1}\,\frac{d\,M_1}{d\,t}\,, \tag{2.30}$$

where $\frac{\partial R_{L,1}}{\partial t}$ depends on tides and gravitational wave radiation and ζ_L describes the response of the Roche-lobe to mass loss. If $\zeta_L > \zeta$, the Roche-lobe shrinks faster than the radius of the star does and the mass transfer is unstable; otherwise, it remains stable until the radius changes significantly by nuclear burning. Mass transfer can be unstable either on a dynamical timescale (Eq. 2.31) or on a thermal timescale (Eq. 2.32):

$$t_{\rm dyn} \sim \sqrt{\frac{\frac{4}{3}\,\pi\,R^3}{G\,M}} \sim 3300\left(\frac{R}{\mathrm{R}_\odot}\right)^{3/2}\left(\frac{\mathrm{M}_\odot}{M}\right)^{1/2}\mathrm{s}\,, \tag{2.31}$$

$$t_{\rm therm} \sim \frac{G\,M^2}{R\,L} \sim 3\times10^7\left(\frac{M}{\mathrm{M}_\odot}\right)^2\frac{\mathrm{L}_\odot}{L}\,\frac{\mathrm{R}_\odot}{R}\,\mathrm{yr}\,. \tag{2.32}$$

If mass transfer is dynamically unstable or both stars overfill their Roche lobe, then the binary is expected to merge or enter common envelope.

2.3.2 Common Envelope

If two stars undergo common envelope (CE) episodes, their envelopes stop co-rotating with their cores, which are now embedded in the same non-cororating envelope, and start spiralling-in as a consequence of the gas drag exerted by the envelope. The same phenomenon can happen also in a binary system composed of a star and a compact object. Part of the energy lost by the cores as an effect of this drag is converted into heating of the envelope, making it more loosely bound. If this process leads to the ejection of the envelope, then the binary survives, but the post-CE binary is composed of two naked stellar cores (or of a compact object and a naked stellar core). If the envelope is not ejected, the cores spiral in till the merger. Fig. 2.14 shows a schematic representation of a BH-star binary which undergoes a common envelope episode.

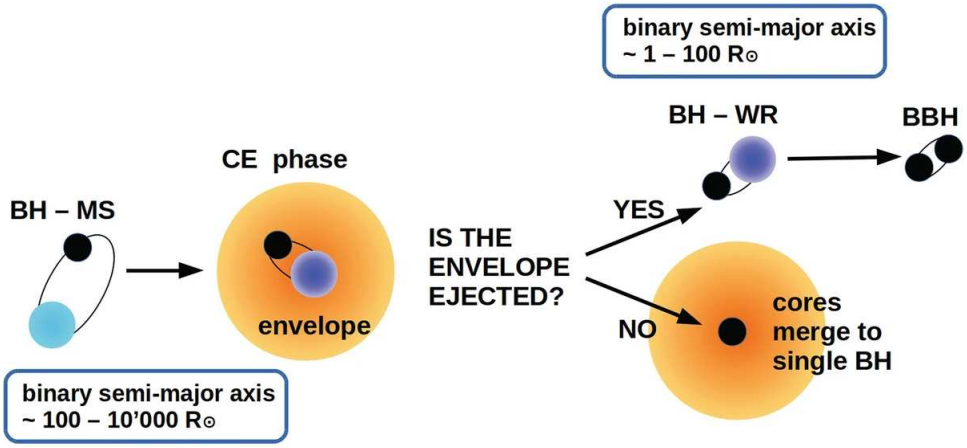

Figure 2.14: Schematic representation of a common envelope episode (Mapelli, 2021 [46]). The initial binary is composed by a BH and a MS star.

The α formalism is usually adopted to describe CE (Webbink, 1984 [47]): the idea is that the energy needed to unbind the envelope is provided by the energy lost by the cores during the spiral in phase and can be expressed as:

$$\Delta E = \alpha \left(E_{b,f} - E_{b,i}\right) = \alpha \frac{G\, M_{c1}\, M_{c2}}{2} \left(\frac{1}{a_f} - \frac{1}{a_i}\right), \tag{2.33}$$

where $E_{b,i}$ and $E_{b,f}$ are the binding energy of the two cores before and after the CE phase, a_i and a_f are the semi-major axes before and after the CE phase, M_{c1} and M_{c2} are the masses of the cores and α is a dimensionless parameter quantifying the fraction of energy transferred to the envelope. The binding energy of the envelope is:

$$E_{\rm env} = G \left[\frac{M_{\rm env1}\, M_1}{\lambda_1\, R_1} + \frac{M_{\rm env2}\, M_2}{\lambda_2\, R_2}\right], \tag{2.34}$$

where M_1 and M_2 are the masses of the members of the binary, $M_{\rm env1}$ and $M_{\rm env2}$ are the masses of the envelopes, R_1 and R_2 the radii of the members of the binary and $\lambda_{1,2}$ measures the concentration of the envelope. Imposing ΔE $= E_{\rm env}$, we can derive the a_f at which the envelope is ejected: if $a_f < R_1 + R_2$, the binary merges during CE; otherwise, it survives. This model poorly describes the real physics of CE and analytic models and numerical simulations are essential in order to improve the model (Mapelli, 2021 [46]).
However, also phenomena different from CE are possible. As discussed in Section 2.1.1, VMSs have a quasi-chemically homogeneous evolution and their radii are usually smaller than the radii of stars developing a chemical composition gradient. Marchant et al. (2016 [48]) simulated tight binaries whose components are fast rotating massive stars. Some of their simulated binaries evolve into contact binaries whose components fill and overfill their Roche volumes. If the metallicity is low enough ($Z < Z_\odot/10$) and the orbital period short enough ($P_{\rm orb} < 3$ d), these binaries may evolve as over-contact binaries, which differs from the classical CE. Indeed, the co-rotation can be maintained until the material does not overflow through the second Lagrangian point L_2 (see Fig. 2.13). This means that the spiral-in can be avoided and the system can remain stable evolving on a nuclear timescale.

Chapter 3

Pair-Instability Supernovae

In this Chapter, I discuss pair-instability supernova (PISN) and pulsational pair-instability supernova (PPISN) events, analysing the uncertainties of the pair-instability mass gap. Then, I describe the observational candidates and constrains.

3.1 Theoretical Framework

Stellar winds are less efficient at low metallicities and this can lead to stars with very massive He- and CO-core, favoring them to end up in the mass range in which PISNe and PPISNe take place: if the mass of the helium core is between 64 $M_\odot$ and 135 $M_\odot$, the star is expected to explode leaving no compact remnant (PISN); if the mass of the helium core is between 32 $M_\odot$ and 64 $M_\odot$, the star can undergo strong mass ejections in different pulsations (PPISN), before collapsing in a black hole (Heger & Woosley 2002 [51]). Indeed, if the helium core grows above 32 $M_\odot$ and core temperature is higher than $7{\times}10^8$ K, the pair-creation of electrons and positrons ($\gamma + \gamma \longrightarrow e^- + e^+$) becomes efficient resulting in a dynamical instability: photons should provide the radiation pressure to contrast the gravitational collapse, but their energy is now diverted in the production of electrons and positrons, triggering a contraction of the core at an accelerated rate. The collapse causes the ignition of explosive reactions involving heavier elements, in particular oxygen and silicon, that lead to either pulsations or supernova explosion (Barkat et al. 1967 [49], Fowler & Hoyle 1964 [50]). If the helium core is more massive than 135 $M_\odot$, the contraction cannot be reversed and the star collapses directly in a black hole (Woosley 2017 [14]).
A perturbation method is usually adopted to understand if the star is globally stable or not. Anyway, a study by Stothers (1999 [52]) has shown that an approximated criterion based on the first adiabatic exponent Γ_1 weighted and integrated over the whole star can determine the stability of the star; by adopting this stability criterion, we say that the star is unstable when:

$$\langle \Gamma_1 \rangle = \frac{\int_0^M \frac{\Gamma_1 P}{\rho}\, dm}{\int_0^M \frac{P}{\rho}\, dm} < \frac{4}{3}\,, \tag{3.1}$$

where $\Gamma_1 = \left(\frac{\partial \ln P}{\partial \ln \rho}\right)_{\rm ad}$ is the first adiabatic exponent, P is the pressure, ρ is the density and M the mass of the star. A T_c vs ρ_c diagram is reported in Fig. 3.1: the region enclosed by the dashed line is the region where $\Gamma_1 < \frac{4}{3}$ and the solid lines are the evolutionary tracks of two models at $M = 150$ $M_\odot$ and $M = 250$ $M_\odot$. When $\langle \Gamma_1 \rangle < \frac{4}{3}$, the radiation pressure is not able to sustain the gravitational pull due to the large mass of the star and higher the temperature, more the pairs produced, accelerating the collapse. If the collapse velocity is not high enough, the nuclear reactions can halt it and produce a bounce: the more massive the helium core, the deeper the bounce and higher the bounce temperature, more the oxygen burnt leading to a thermonuclear explosion that disrupts the star; in the PPISN case, the energy released by the explosive burning is not enough to unbind the star.
PPISNe have been extensively discussed in a paper by Woosley (2017 [14]): he modeled a set of pure

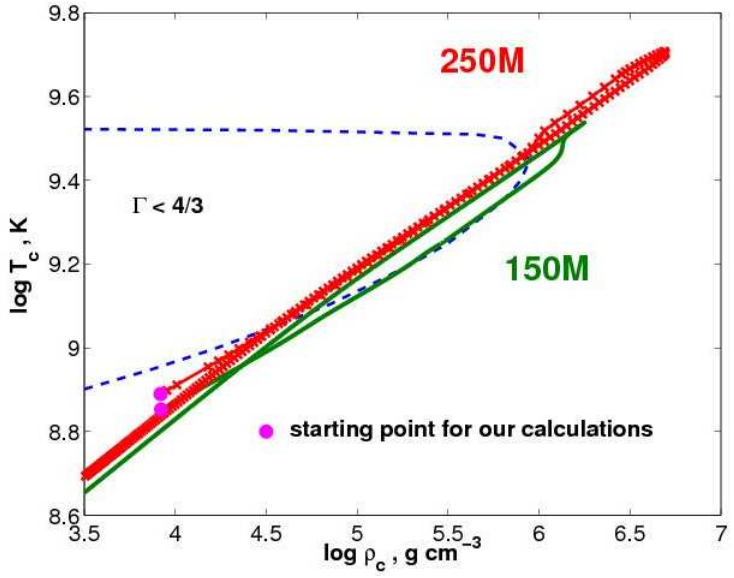

Figure 3.1: Evolutionary tracks of 150 $M_\odot$ (green) and 250 $M_\odot$ (red) models in central density – temperature diagram. The area enclosed by the dashed line indicates the pair-instability regime where $\Gamma < \frac{4}{3}$. The filled circles mark the starting points for each model sequence [18].

helium stars with masses ranging from 30 $M_\odot$ to 64 $M_\odot$, resulting in a range of CO-core masses between $\sim$ 24 $M_\odot$ and $\sim$ 54 $M_\odot$, at Z = 0. The study of pure helium stars in this context is quite common, since VMSs are expected to be stripped of their H envelope in the last evolutionary phases, the ones which are important to understand the pair-instability regime; however, if a star ejects or not its envelope is one the main uncertainties to properly determine the pair-instability mass gap, as discussed in the following. For pure-helium cores up to 40 $M_\odot$, the pulsational pair-instability regime starts earlier for the more massive stars reaching an energy of 10^{49} erg at 40 $M_\odot$. Beyond this mass, the pulsations are not perturbations of the core structure anymore, but single explosive events generating significant mass ejections. Each explosion is then followed by relaxation oscillations and a period in which the star contracts to a new unstable state. More than 100 weak pulsations are found in the 38 $M_\odot$ model, while 18 strong pulsations are present in the 42 $M_\odot$ model. In the 64 $M_\odot$ model, only one pulsation occurs and it completely disrupts the star leaving no compact remnant: so, PISNe can be seen as a particular case of PPISNe in which the star can experience only one pulsation. The histories of the pulses in 36, 40, 44, 48, 50 and 52 $M_\odot$ models are reported in Fig. 3.2.
The masses of the final BHs after the pulsating phase range between 34 $M_\odot$ and 47 $M_\odot$ and then a gap in the BH mass distribution is opened due to PISNe, but many uncertainties still affect our comprehension of these events and how they can impact the BH mass distribution. The most important one relies on our knowledge of VMSs evolution, but another important one is related to the carbon-α $^{12}C(\alpha,\gamma)^{16}O$ reaction rate. Farmer et al. (2017 [53]) studied the robustness of the lower limit of the pair-instability mass gap $M_{\text{low-lim}} \sim 47\ M_\odot$ varying metallicity, internal mixing and mass-loss rate: simulating pure-helium stars, they found it is remarkably robust, resulting in a shift of $3-4\ M_\odot$; instead, changing the $^{12}C(\alpha,\gamma)^{16}O$ reaction rate within its 1σ uncertainty shifts the location of the gap between 40 $M_\odot$ and 56 $M_\odot$. The range of CO-core mass values in which the star enters the pair-instability regime is in any case consistent with the ones found by Woosley [14]. Costa et al. (2021 [54]) added another element to this analysis, considering also the hydrogen envelope: if it collapses onto the final BH, the lower limit of the pair-instability mass gap may increase of $\sim$ 20 $M_\odot$ [46]. Assuming an optimistic approach in which the whole H envelope collapses onto the final BH, they found $M_{\text{low-lim}} \sim 68\ M_\odot$ as lower limit of the gap adopting the standard $^{12}C(\alpha,\gamma)^{16}O$ reaction rate; instead, when they considered a lower rate at -3σ, the gap completely disappears. This confirms the important role played by the carbon-α rate.

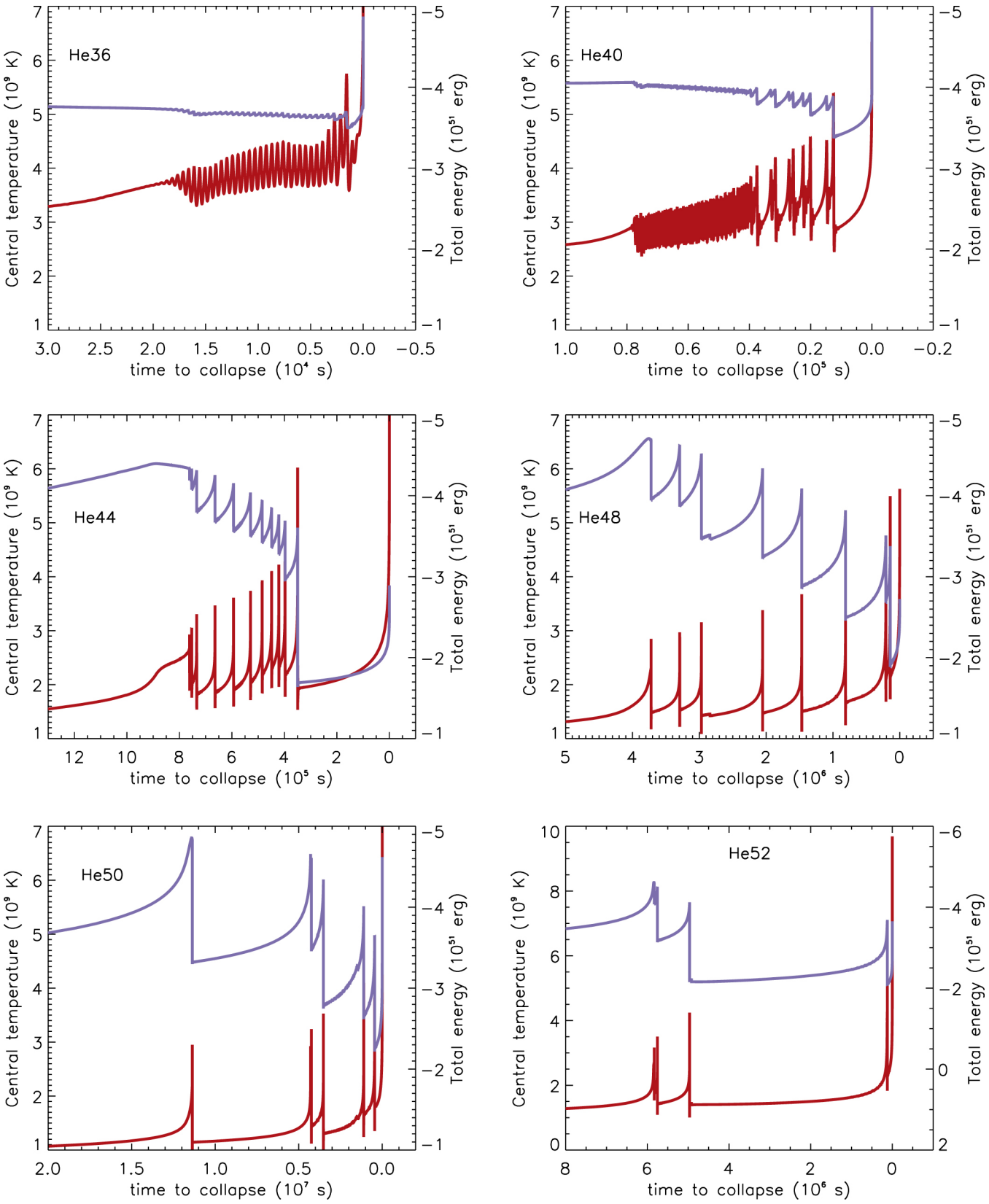

Figure 3.2: Pulse history in pure helium stars of 36, 40 44, 48, 50 and 52 $M_\odot$. Central temperature in 10^9 K is the red line and net binding energy in 10^{51} erg is blue. Time, measured prior to final core collapse to a black hole, is in units of 10^4 s for the 36 $M_\odot$ model; 10^5 s for the 40 and 44 $M_\odot$ models; 10^6 s for the 48 $M_\odot$ and 52 $M_\odot$ models; and 10^7 s for the 50 $M_\odot$ model. [14].

3.2 Pair-Instability Supernova Candidates

Even if the exact limits of the pair-instability mass gap can be debated and are affected by many uncertainties, the theoretical predictions are clear and robust: VMSs at low metallicities with He-core mass between 64 $M_\odot$ and 135 $M_\odot$ are expected to experience PISNe at the end of their life. However, up to now, no unambiguous PISN candidates have been detected and, in a recent paper, Arca Sedda et al. (2024 [55]), analysing the PISN rate in massive clusters, suggested that only future surveys can obtain unquestionable detections of them.
PISNe can produce tens of solar masses of radiative ^{56}Ni, resulting in a luminous transient similar to the one of super-luminous SNe (SLSNe); through the analysis of SLSN events, some PISN candidates have been observed. Schulze et al. (2024 [56]) monitored the photometric and spectroscopic evolution in ultraviolet (UV) and near-infrared (NIR) of the SN 2018ibb for more than three years. SN 2018ibb is a hydrogen-poor SLSN at redshift z = 0.166 that evolves extremely slowly compared to other SLSNe; it radiated $> 3 \times 10^{51}$ erg during its evolution and the bolometric light curve reached 2×10^{44} erg s^{-1} at the peak. Both the light curve (Fig. 3.3) and the spectrum (Fig. 3.4) require 25-44 $M_\odot$ of ^{56}Ni, pointing to the explosion of a metal-poor star with a He-core mass of 120-130 $M_\odot$. SN 2018ibb is the best PISN candidate to date, since it passed the following tests:

- rise time $>$ 93 days (expectation: 120-150 days);
- production of 25-44 $M_\odot$ of ^{56}Ni (expectation: 10-44 $M_\odot$);
- bolometric light curve consistent with PISN models;
- ejecta velocity $\sim$ 8500 km s^{-1} (expectation: 7000-11000 km s^{-1});
- flat evolution of the velocity after the maximum light;
- low metallicity Z $\sim$ $Z_\odot/4$.

Some unexpected features are however present: PISN models do not predict significant [Co II] λ 1.025 μm, which is instead here measured and represent an unique case among PISN candidates and any SLSNe; an excess bluewards of 5000 Å , which does not fit the models, is present, but it can be partially explained with the interaction with the circumstellar medium.
Assuming that PISN and SLSN luminosity functions are roughly the same, it is possible to express the PISN rate density $R_{\rm PISN}$ as function of the SLSN one and set its upper limit; if SN 2018ibb is a true PISN, this sets the lower limit, resulting in the following observational constraints between redshift z = 0.1 and z = 0.2: 0.009 Gpc^{-3} yr^{-1} $\leq R_{\rm PISN} \leq$ 0.7 Gpc^{-3} yr^{-1}. These values are lower with respect to the ones predicted in previous works (except for the one in Briel et al., 2022 [59]). A meaningful comparison with other models is however quite complicated due to the dependencies on stellar evolution models and cosmic star formation rate density.

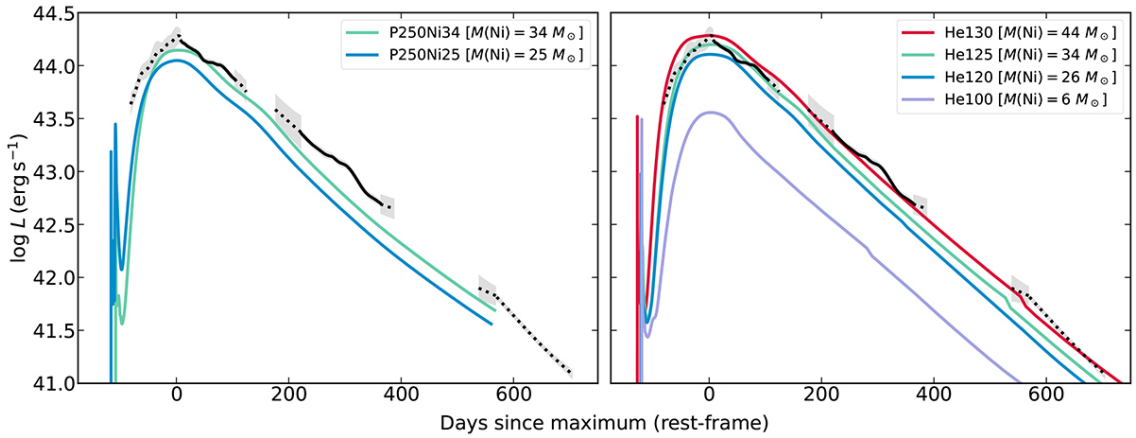

Figure 3.3: Comparison of 2018ibb with models P250Ni25 and P250Ni34 in Kozyreva et al. (2017 [57]) (left) and the He100, He125, and He130 in Heger & Woosley (2002 [51]) (right). The black line is the SN 2018ibb luminosity [56].

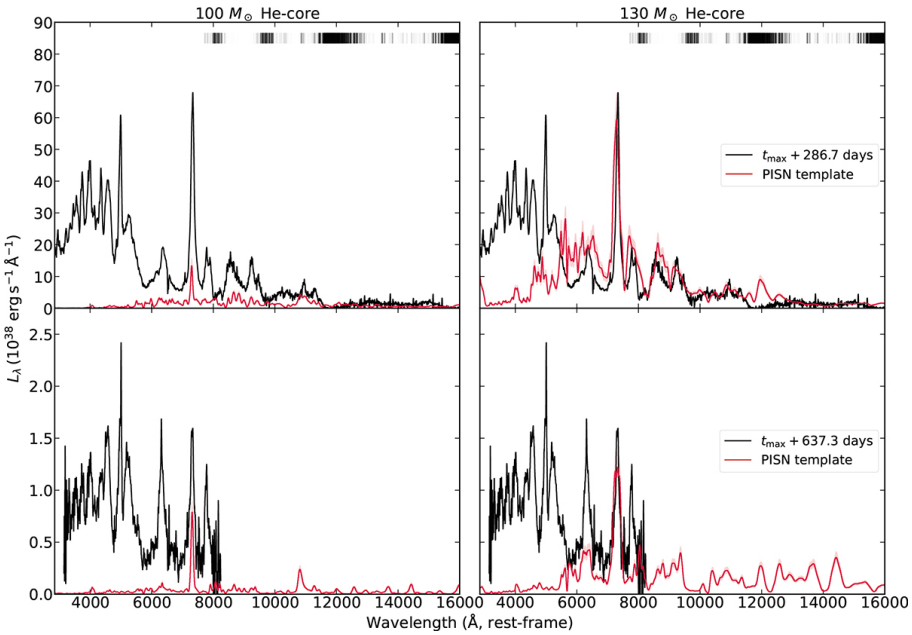

Figure 3.4: Late-time spectra of SN 2018ibb at 287 and 637 days after its maximum. Overlaid are the computed PISN spectra from Jerkstrand et al. (2016 [58]) scaled to these epochs. The shaded region indicates the uncertainty of the explosion time. The He130 model provides an adequate description of the emission redwards of 6000 Å at t_{max}+286.7 days, but a worse match for the second epoch. The He100 model matches the observation of neither epoch [56].

There is also an indirect way to detect PISNe and PPISNe, studying the chemical signature. Indeed, they can enrich the environment with a unique abundance pattern, characterized by a high ratio of even-to-odd elements. This is related to a lower neutron excess with respect to core-collapse supernovae (CCSNe) and the fact that odd-charged isotopes are neutron-rich: the core of PISN progenitors is usually less dense than the one of CCSN progenitors and the neutronization ($e^- + p \longrightarrow n + \nu_e$) is less significant in the final evolutionary stages of the star. The star J1010-2358 is a promising candidate for a pure descendant of a Pop. III 260 $M_\odot$ PISN, showing a strong odd-even effect in its abundance pattern (Xing et al., 2023 [60]). In Fig. 3.5 a new analysis of the same star by Skúladóttir et al. (2024 [61]) is reported, in which it is shown that the best fit model consists in a 13 $M_\odot$ Pop. II CCSN combined with a 39 $M_\odot$ Pop. III CCSN. This discussion shows also the limits of this kind of analysis to study the occurrence of PISNe, since we cannot be sure about which events polluted the gas from which the stars were formed.

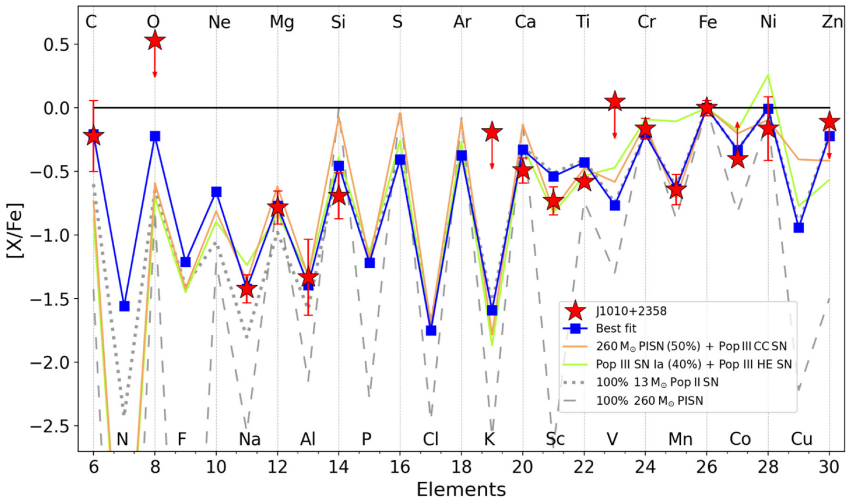

Figure 3.5: Abundance pattern of J1010+2358 (red) compared with the best fit (blue); additionally shown are environments enriched by a 260 $M_\odot$ PISN (50%) and a Pop. III CCSN (orange); a Pop. III SN Ia (40%) and a high-energy Pop. III SN (green); the 13 $M_\odot$ Pop. II SN; and a 260 $M_\odot$ PISN (grey dashed) [61].

Chapter 4

Methodology

In this Chapter, I describe the tools used to develop and analyze my models. In particular, I explain what stellar evolution and population synthesis codes are and how I combined their results with a metal-dependent star formation rate history thanks to the semi-analytical code COSMORATE.

4.1 Stellar Evolution Codes

A stellar evolution code is a computational tool that simulates the life-cycle of stars, from their formation to the advanced evolutionary phases. The core of a stellar evolution code involves solving a series of differential equations that represent the key physical processes and internal structure of a star. These processes include: nuclear fusion, which releases energy; energy transport, which can occur through radiation, convection, or conduction; opacity; mass loss due to stellar winds. In general, for numerical codes it is more convenient to use the mass as coordinate instead of radius. So, in this coordinate system, the fundamental equations of the stellar structure are:

$$\text{Continuity equation: } \frac{\partial r}{\partial m} = \frac{1}{4\,\pi\,r^2\,\rho}\,; \tag{4.1}$$

$$\text{Hydrostatic equilibrium: } \frac{\partial P}{\partial m} = -\frac{G\,m}{4\,\pi\,r^4}; \tag{4.2}$$

$$\text{Energy conservation: } \frac{\partial L}{\partial m} = \epsilon_n - \epsilon_\nu; \tag{4.3}$$

$$\text{Transport equation: } \frac{\partial T}{\partial m} = -\frac{G\,m\,T}{4\,\pi\,r^4\,P}\,\nabla; \tag{4.4}$$

where ϵ_n, ϵ_ν are the energy from nuclear reactions and the one lost by neutrinos, and $\nabla \equiv \frac{d\,\ln T}{d\,\ln P}$ depends on the dominant energy transport.
In addition to the system of equations just considered, they implement functions to take into account also:

$$\text{Equation of state: } \rho = \rho(P,\,T); \tag{4.5}$$

$$\text{Wind mass loss: } \frac{d\,M_{\rm tot}}{d\,t} = f(L, T, Z); \tag{4.6}$$

$$\text{Chemical evolution: } \frac{\partial\,X_i}{\partial\,t} = \frac{m_i}{\rho}\Big(\sum_j r_{ji} - \sum_k r_{ik}\Big), \tag{4.7}$$

where r_{ji} (r_{ik}) is the rate of the reactions that transform the element j (i) in i (k).
A stellar evolution code requires input parameters such as the star initial mass, chemical composition and rotation rate. Then, by integrating these equations, the code can evolve stars through the various stages: proto-star formation, main sequence, red giant/supergiant and final stages. The computational power and numerical techniques employed in these codes have advanced significantly: modern codes

use adaptive time-step, parallel processing, and sophisticated algorithms to handle the vast range of timescales and physical conditions present in stellar interiors. These improvements allow for high-resolution simulations that can capture detailed phenomena such as convection currents, pulsations and the effects of magnetic fields.
Many different stellar evolution codes have been developed, e.g. STARS (Eggleton 1971 [62]), STERN (Yoon & Langer 2005 [79]), PARSEC (Bressan et al. 2012 [63]), FRANEC (Degl'Innocenti et al. 2018 [64]), BEC (Szécsi et al. 2022), GENEC (Eggenberger et al. 2008 [66]), MESA (Paxton et al. 2011 [33], 2013 [34], 2015 [35], 2018 [36], 2019 [37]), but they are all private except for MESA.
In this work, I used MESA to model the evolution of VMSs (single stellar models and binary systems) implementing the new winds by Sabhahit et al. (2023 [38]; Section 2.2.3) and produce tracks for the population synthesis code SEVN.

4.1.1 MESA

MESA (Modules for Experiments in Stellar Astrophysics) is 1D hydrostatic stellar evolution code, written in Fortran. It is built on a modular framework, enabling users to customize simulations as they need. Indeed, this modularity allows to customize different aspects of stellar evolution such as nuclear reactions, energy transport, mass loss and convection processes. Some of the most important modules are:

- `eos`, which models the equation of state, working with density and temperature as independent variables and it is based on OPAL EOS tables (Rogers & Nayfonov 2002 [67]); outside the range covered by these tables, MESA switches to SCVH tables (Saumon et al. 1995 [68]) when $\log(T_{\rm eff}/{\rm K}) < 3.5$ and $\log(\rho_c/[{\rm g\ cm^{-3}}]) < -2$, HELM (Timmes & Swesty 2000 [69]) and PC (Pothekin & Chabrier 2010 [70]) tables when $\log(T_{\rm eff}/{\rm K}) > 7.5$ and $\log(\rho_c/[{\rm g\ cm^{-3}}]) > 2.5$;

- `net`, which implements the nuclear reaction networks and includes the `basic` network (which contains only 8 isotopes: H, ^{3}He, ^{4}He, ^{12}C, ^{14}N, ^{16}O, ^{20}Ne, ^{24}Mg) and more extended networks for detailed computations (Timmes 1999 [71]);

- `atm`, which uses mass, radius and luminosity to set the pressure P_s and temperature T_s at the top of the outermost cell through direct integrations or interpolations in model atmosphere tables (Grevesse & Noels 1993 [72], Castelli & Kurucz 2003 [73]);

- `star`, which is a stellar structure and evolution library that uses the other modules to evolve the star;

- `binary`, which uses the `star` module to initialise and evolve two stars (or one star and a compact object) in order to perform binary evolution.

The boundary conditions and fundamental parameters can be specified through an `inlist` file, while additional functions can be added through specific `run_star_extras` files.
To model VMSs, I used the MESA version r12115 [33] [34] [35] [36] [37], which includes improvements in the handling of opacity tables, updates of the equation of state and nuclear reaction network modules and optimizations to improve the computational efficiency. I describe the treatment of massive and very massive stars (Paxton et al. 2013 [34]) and binary systems (Paxton et al. 2015 [35]) in MESA in the following.
Massive and very massive stars are numerically difficult to model and one reason relies on their loosely bound, radiation pressure dominated envelopes that can cause density and gas pressure inversions, and inflation of the radius at lower temperatures with respect to the less massive stars. To explain how these issues are treated in MESA, let me introduce the mixing length theory (MLT), implemented in the `mlt` module.
The MLT of convection describes the bulk movement of fluids in analogy with molecular heat transfer. In each time-step, the thermodynamic structure of a model must be calculated and this requires knowledge of whether any shell is stable against convection. According to Ledoux criterion (Ledoux,

1947 [74]), dynamical stability is given by

$$\nabla_{\rm rad} < \nabla_{\rm ad} + \frac{\phi}{\delta}\nabla_{\mu}\,, \tag{4.8}$$

where ϕ and δ are the partial derivatives of density with respect to temperature and chemical composition, $\nabla_{\rm rad}$ and $\nabla_{\rm ad}$ are the radiative and adiabatic temperature gradients and ∇_{μ} is the chemical composition gradient. Assuming homogeneous chemical composition, $\nabla_{\mu} \longrightarrow 0$ and the Schwarzschild stability criterion is met: $\nabla_{\rm rad} < \nabla_{\rm ad}$ (Schwarzschild, 1958 [75]). Where the criterion is satisfied, the evaluated zone is stable and the flux is carried out by radiation. On the other hand, in case of efficient convection, the flux $\rm F_{conv}$ is carried entirely by convection. A useful toy model for MLT is:

$$F_{\rm conv} = \frac{1}{2}\,\rho\, v\, c_p\, T\, \alpha_{\rm MLT}\,(\nabla_T - \nabla_{\rm ad})\,, \tag{4.9}$$

with

$$\alpha_{\rm MLT} \equiv \frac{\lambda}{H_P}\,, \tag{4.10}$$

where ρ, v, c_p are density, velocity of the convective cells and specific heat and ∇_T takes into account the balance of the global temperature gradient; Eq. 4.10 is the definition of the mixing length parameter $\alpha_{\rm MLT}$, which characterizes the distance λ that a parcel of convective material can travel, in terms of the pressure scale height $\rm H_P = \frac{d\ln P}{d\ln T}$. The parameter $\alpha_{\rm MLT}$ can be seen as the convective mean-free path or the convective efficiency: the higher $\alpha_{\rm MLT}$, the more the flux carried by convection (Cox & Giuli 1968 [76], Joyce & Tayar 2023 [77]).
Since the velocity of the convective cells depends on the difference $\nabla_T - \nabla_{\rm ad}$ (Pasetto et al. 2016 [78]), when a super-adiabatic gradient ($\nabla_T > \nabla_{\rm ad}$) arises in the radiation-dominated envelopes, the convective velocity can approach the sound speed and it can force the adoption of prohibitively short time-steps: the treatment of convective energy transport by MLT is out of its applicability domain. To avoid super-adiabatic zones, a treatment of the convection which involves an a-posteriori reduction of the super-adiabatic gradient has been introduced; this MESA method is called MLT++. For each model, `MESA star` computes

$$\lambda_{\rm max} \equiv \max\left(\frac{L_{\rm rad}}{L_{\rm Edd}}\right)\,,\ \beta_{\rm min} \equiv \min\left(\frac{P_{\rm gas}}{P}\right)\,. \tag{4.11}$$

When $\delta_{\nabla} \equiv \nabla_T - \nabla_{\rm ad}$ is higher than a fixed threshold, whose default values is $\delta_{\nabla,\rm thresh} \sim 10^{-3}$, the super-adiabaticity is artificially reduced, so that convection is still inefficient: `MESA star` sets ∇_T to reduce $\delta_{\nabla} - \delta_{\nabla,\rm thresh}$ by a factor $\alpha_{\nabla} \times f_{\nabla}$, where f_{∇} is specified by the user and α_{∇} is a linear combination of $\lambda_{\rm max}$ and $\beta_{\rm min}$; for large values of $\lambda_{\rm max}$ and small values of $\beta_{\rm min}$, $\alpha_{\nabla} \longrightarrow 1$. The comparison between tracks with MLT and MLT++ implemented is shown in Fig. 4.1. As shown and discussed in the next chapter, the new stellar wind model, described in Section 2.2, can self-regulate the super-adiabatic gradient and prevent the radius inflation (at least in the main sequence).
The module `MESA binary` uses `MESA star` to evolve binary systems; it can be used to model a star plus a point-mass companion or two stars. In the following formulas, $\rm M_1$, $\rm R_1$ and $\rm R_{RL,1}$ are the mass, radius and Roche-lobe radius of the donor star. The radius of the Roche lobe is modelled following Eq. 2.28 and the stability of the mass transfer is understood in terms of mass-radius relationships, similarly to what described in Section 2.3.1. Adopting $\zeta_{\rm eq}$, $\zeta_{\rm ad}$ and $\zeta_{\rm RL}$ defined as:

$$\zeta_{\rm eq/ad} = \left(\frac{d\,\ln\,R_1}{d\,\ln\,M_1}\right)_{\rm eq/ad}\,, \tag{4.12}$$

$$\zeta_{\rm RL} = \frac{d\,\ln\,R_{\rm RL,1}}{d\,\ln\,M_1}\,, \tag{4.13}$$

if the overflowing satisfies $\zeta_{\rm eq} > \zeta_{\rm RL}$, it remains inside the lobe transferring mass in thermal equilibrium; if $\zeta_{\rm ad} > \zeta_{\rm RL} > \zeta_{\rm eq}$, the mass transfer occurs on a thermal timescale (Eq. 2.32); if $\zeta_{\rm RL} > \zeta_{\rm ad}$, the star is not in hydrostatic equilibrium, the process becomes dynamical and MESA cannot handle it anymore. Anyway, I did not use this criterion in my simulations. Indeed, the simulations, which

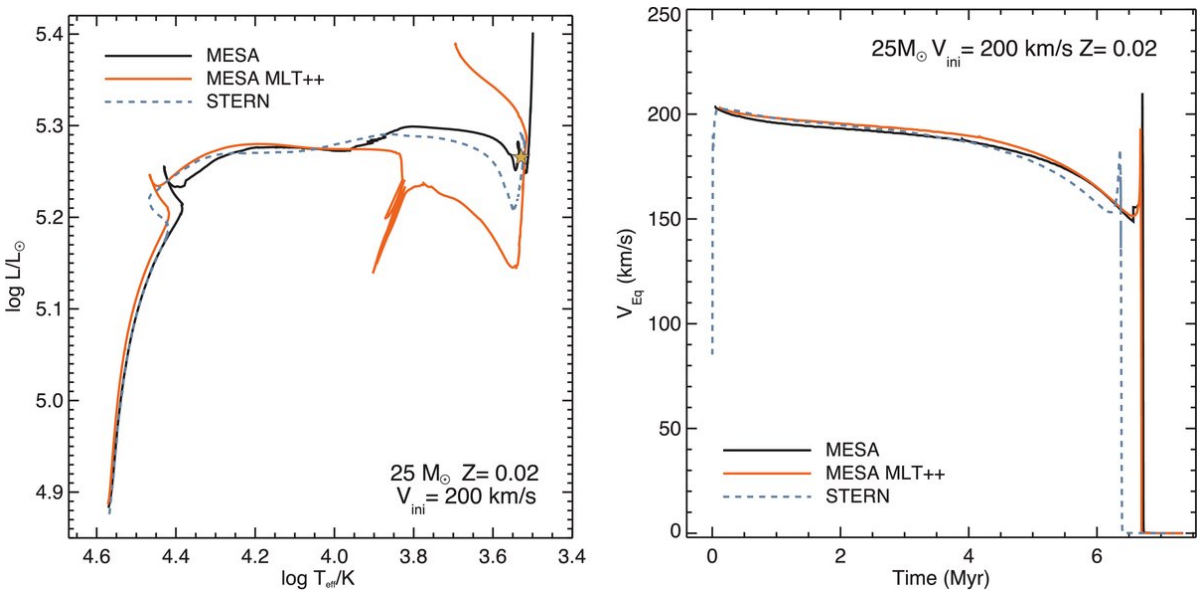

Figure 4.1: Comparison of evolutionary tracks (left) and equatorial rotational velocity (right) for a 25 $M_\odot$ model with Z = 0.02 and v_{eq} = 200 km s^-1. The solid black lines show MESA star results with MLT (black) and MLT++ (orange), while the dashed blue line refers to the stellar evolution code STERN calculations (Yoon & Langer 2005 [79]). [34].

did not reach the fixed stopping condition, terminated due to numerical reasons (in particular, a too short time-step) probably related to an unstable mass transfer (see Section 5.3).
To model the mass transfer, I chose the explicit method by Kolb (Kolb & Ritter 1990 [81]), which is an extension of the Ritter scheme (1988 [80]) and covers also the case in which $R_1 > R_{RL,1}$:

$$\dot{M}_{\rm RLOF} = -\dot{M}_0 - 2\,\pi\,F_1(q_2)\,\frac{R^3_{\rm RL,1}}{G\,M_1} \times \int_{P_{\rm ph}}^{P_{\rm RL}} \Gamma_1^{1/2} \left(\frac{2}{\Gamma_1+1}\right)^{\frac{\Gamma_1+1}{2\Gamma_1-2}} \left(\frac{k_B\,T}{m_p\,\mu}\right)^{1/2} d\,P\,, \tag{4.14}$$

with

$$\dot{M}_0 = \frac{2\,\pi}{exp(1/2)}\,F_1(q_2)\,\frac{R^3_{\rm RL,1}}{G\,M_1}\left(\frac{k_B\,T_{\rm eff}}{m_p\,\mu_{\rm ph}}\right)^{3/2}\rho_{\rm ph}\,, \tag{4.15}$$

and

$$F_1(q_2) = 1.23 + 0.5\,\log(q_2)\ \text{ if }\ 0.5 < q_2 < 10\,, \tag{4.16}$$

where $q_2 = M_2/M_1$, m_p is the proton mass, $T_{\rm eff}$ is the effective temperature of the donor, $\mu_{\rm ph}$ and $\rho_{\rm ph}$ are the mean molecular weight and density at its photosphere, Γ_1 is the first adiabatic exponent, $P_{\rm ph}$ and $P_{\rm RL}$ are the pressure at the photosphere and at $R_{\rm RL,1}$. The mass transfer rate for a binary composed by 8 $M_\odot$ and 6 $M_\odot$ stars is shown in Fig. 4.2. So, the total time derivatives of the component masses are given by

$$\dot{M}_1 = \dot{M}_{1,w} + \dot{M}_{\rm RLOF}\,,\ \dot{M}_2 = \dot{M}_{2,w} - f_{mt} \times \dot{M}_{\rm RLOF}\,, \tag{4.17}$$

where $\dot{M}_{i,w}$ are the mass-loss rate due to stellar winds of donor and accretor star and f_{mt} represent the accretion efficiency:

$$f_{mt} = 1 - \alpha_{mt} - \beta_{mt} - \delta_{mt}\,, \tag{4.18}$$

where α_{mt}, β_{mt}, δ_{mt} are the fraction of mass transferred which is lost from the vicinity of the donor, accretor and circumbinary toroid.
To compute the rate of change of orbital angular momentum, contributions by gravitational waves (Eq. 4.19), mass loss (Eq.4.20), magnetic breaking (Eq. 4.21) and spin-orbit coupling (Eq. 4.22) are taken into account:

$$\dot{J}_{gr} = -\frac{32}{5\,c^5}\left(\frac{2\,\pi\,G}{P_{\rm orb}}\right)^{7/3}\frac{(M_1\,M_2)^2}{(M_1+M_2)^{2/3}}\,, \tag{4.19}$$

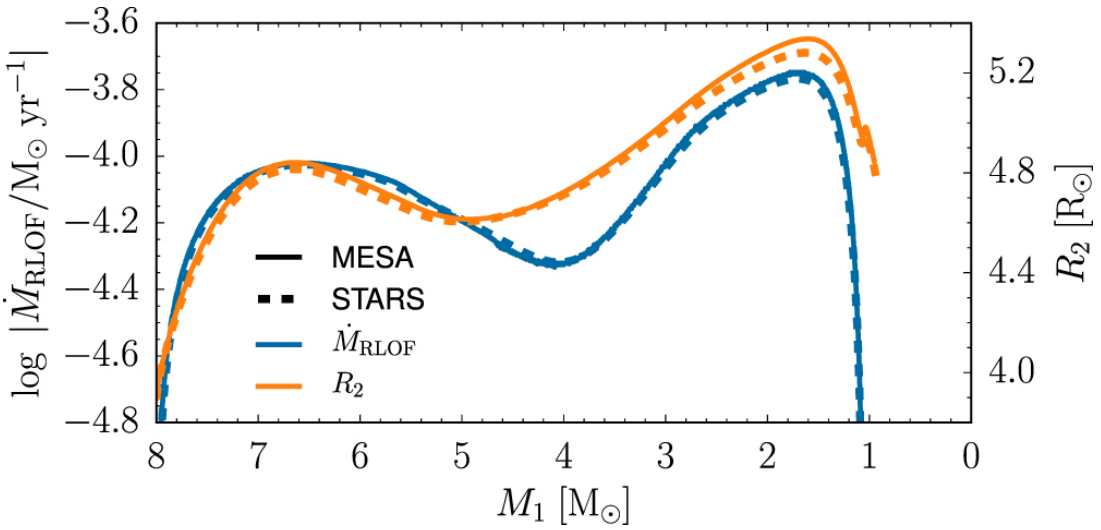

Figure 4.2: Mass transfer rate and accretor radius as computed by MESA and STARS [62] for an 8 $M_\odot$ + 6.5 $M_\odot$ binary with an initial orbital period of 3 days [35]. Fun fact: this figure appeared in the movie "Don't look up!", directed by Adam McKay; it stars an ensemble cast featuring Leonardo DiCaprio, Jennifer Lawrence, Cate Blanchett and Maryl Streep.

$$\begin{aligned} \dot{J}_{ml} = &\left[\left(\dot{M}_{1,w} + \alpha_{ml}\dot{M}_{\rm RLOF}\,M_1^2\right) + \left(\dot{M}_{2,w} + \beta_{ml}\dot{M}_{\rm RLOF}\,M_2^2\right)\right] \times \\ &\times \frac{a^2}{(M_1+M_2)^2}\,\frac{2\,\pi}{P_{\rm orb}} + \gamma_{mt}\,\delta_{mt}\,\dot{M}_{\rm RLOF}\sqrt{G\,(M_1+M_2)\,a}\,, \end{aligned} \tag{4.20}$$

$$\dot{J}_{mb} = -\,6.82\,\times\,10^{34}\,\times\,\left(\frac{M_1}{M_\odot}\right)\left(\frac{R_1}{R_\odot}\right)^{\gamma_{mb}}\left(\frac{1\,d}{P_{\rm orb}}\right)^3\,[\text{dyn cm}]\,, \tag{4.21}$$

$$\dot{J}_{ls} = -\,\frac{1}{\delta t}\left(\delta S_1 - S_{1,lost}\,\frac{\dot{M}_{1,w}}{\dot{M}_1} + \delta S_2 - S_{2,lost}\right), \tag{4.22}$$

where M_1 and M_2 are the mass of the donor and accretor star, $P_{\rm orb}$ is the orbital period, $\gamma_{mt}^2\,a$ is the radius of the toroid, $\gamma_{mb} = 4$, R_1 is the radius of the donor star, $S_{1,lost}$ and $S_{2,lost}$ are the spin angular momenta removed in a step and δS_1 and δS_2 are the changes in the spin angular momenta. Then, the total rate of change of the angular momentum is $\dot{J}_{orb} = \dot{J}_{gr} + \dot{J}_{ml} + \dot{J}_{mb} + \dot{J}_{ls}$.

4.2 Population Synthesis Codes

Stellar evolution codes can produce very precise and complete models of single stars and binary systems, but they are computationally expensive and more than two hours can be needed to reach the end of a single model. To achieve the final aim of this thesis, the evolution of PISN and PPISN rate density across cosmic time, a statistically relevant set of parameters regarding PISNe and PPISNe is essential and a faster tool to model single and binary systems is required.
Stellar population synthesis codes are designed to rapidly model the evolution of stellar populations, composed even by billions of stars, by performing stellar evolution interpolating pre-computed stellar tracks. By means of these codes, I was able to perform semi-analytic evolution of single and binary stellar populations, providing very large statistics: the famous BSE code (Hurley et al. 2000 [82], 2002 [43]), which is the common ancestor of the majority of binary population synthesis codes, evolves 10^6 binary stars in a couple of hours on a single CPU core. Many simplifications are needed and, in particular, the hydrodynamical evolution of the systems is not considered. The speed of population synthesis codes is crucial not only to model the parameter space of massive binary and single star evolution, but also to guarantee that they can be interfaced with N-body codes to study the dynamical formation of compact objects in dense stellar clusters (Iorio et al. 2023 [83]).
Many different population synthesis codes have been developed independently, but the most of them relies on fitting formulas developed by Hurley et al. [82], based on the tracks by Pols et al. (1998 [84]),

which express the main properties of stars as function of stellar age, mass and metallicity.
The more recent population synthesis codes developed strategies to include tracks from different stellar evolution codes (e.g. MESA) and a wider range of masses and metallicities; some examples are COMBINE (Fragos et al. 2023 [85]), METISSE (Agrawal et al. 2020 [86]), POSYDON (Fragos et al. 2023 [87]) and SEVN (Spera et al. 2015 [88], Spera & Mapelli 2017 [10], Spera et al. 2019 [89], Iorio et al. 2023 [83]). They all share the same approach to stellar evolution that consists into including an algorithm that interpolates the main stellar-evolution properties, such as mass, radius, core mass and radius, luminosity, etc. as a function of time and metallicity, from a number of pre-computed tables. The main advantage of this approach is that the interpolation algorithm is more flexible than fitting formulas.
In this work, I used SEVN to interpolate the tracks I produced with MESA and obtain catalogues to explore the rate of PISNe and PPISNe.

4.2.1 SEVN

SEVN (Stellar EVolution for N-body) is a rapid binary population synthesis code, which calculates stellar evolution by interpolating pre-computed sets of stellar tracks, while binary evolution is implemented through analytic and semi-analytic prescriptions [88] [10] [89] [83]. It is written in C++ and exploits CPU-parallelisation through OpenMP; the C++ classes that represent the properties of the single stars and binaries systems are shown in Fig. 4.3.

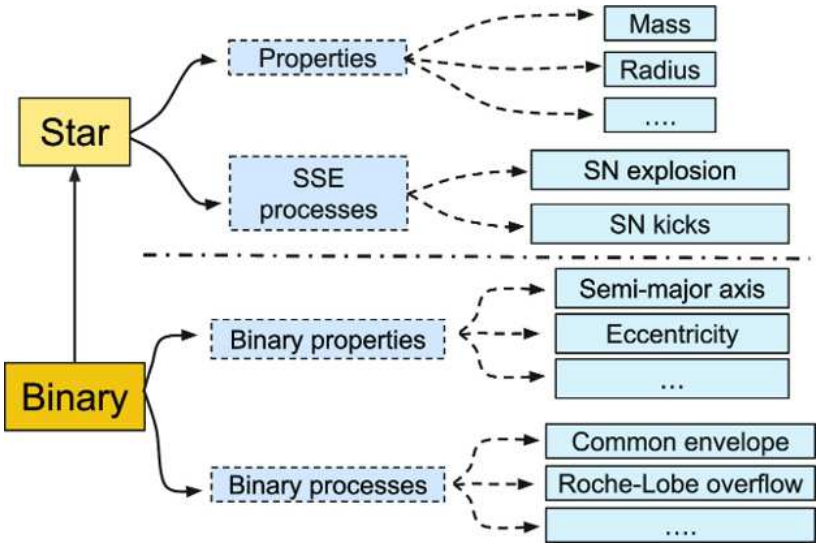

Figure 4.3: In SEVN, single stars, binary systems, properties, and processes are represented with C++ classes. Single stars are characterized by their properties (mass, radius, etc.) and single stellar evolution processes (supernova explosion type and natal kicks). Binary stars are characterized by their properties (semimajor axis, eccentricity, etc.), binary-evolution processes (mass transfer by winds, Roche-lobe overflow, CE, tides, etc.), and by the two stars component of the binary system [83].

In SEVN, the single stellar evolution (SSE) of a star is uniquely defined by the zero-age main sequence (ZAMS) mass $M_{\rm ZAMS}$ and the metallicity Z, so that, given a couple of $(M_{\rm ZAMS}, Z)$, the SSE of this star will be always the same, if the same tables will be used. Two sets of tables are required to model the evolution: the tables for stars starting their lives from hydrogen main sequence and the ones for pure-helium stars. Seven mandatory tables, grouped by metallicity, are required and each table refers to a different properties: star age, total stellar mass, He-core mass, CO-core mass, star radius, bolometric luminosity and stellar phase. In the updated version of SEVN, the stellar evolution is divided into seven physically motivated macro-phases: pre-main sequence phase, from zero-age to the ignition of the hydrogen in the core; main sequence; terminal main sequence phase, when the helium core is created; shell hydrogen burning; helium burning in the core; terminal-age core helium burning, when the carbon-oxygen core starts to form; shell helium burning; finally, remnant phase.
If the option `turn_WR_to_pureHe` is set as true, when the He-core mass is larger than 97.9% of the

total stellar mass, SEVN classifies the star as a WR star and it jumps to a new interpolating track on the pure-He tables. During its life, a star can indeed lose its hydrogen envelope (Section 2.1) and, if a star has a decoupled CO- or He- core, the core's properties are what drive the evolution of the star. The same can happen also in binary systems due to mass transfer episodes (Section 2.3). Then, the criterion followed by SEVN to decide if a change of track is necessary depends on the structure of stars and, unless there is a change in core mass, no change of track is admitted. When a star moves to a new track, SEVN searches the track that best matches the mass of the current star at the same evolutionary stage. A schematic representation of the algorithm used by SEVN to change track is shown in Fig. 4.4.

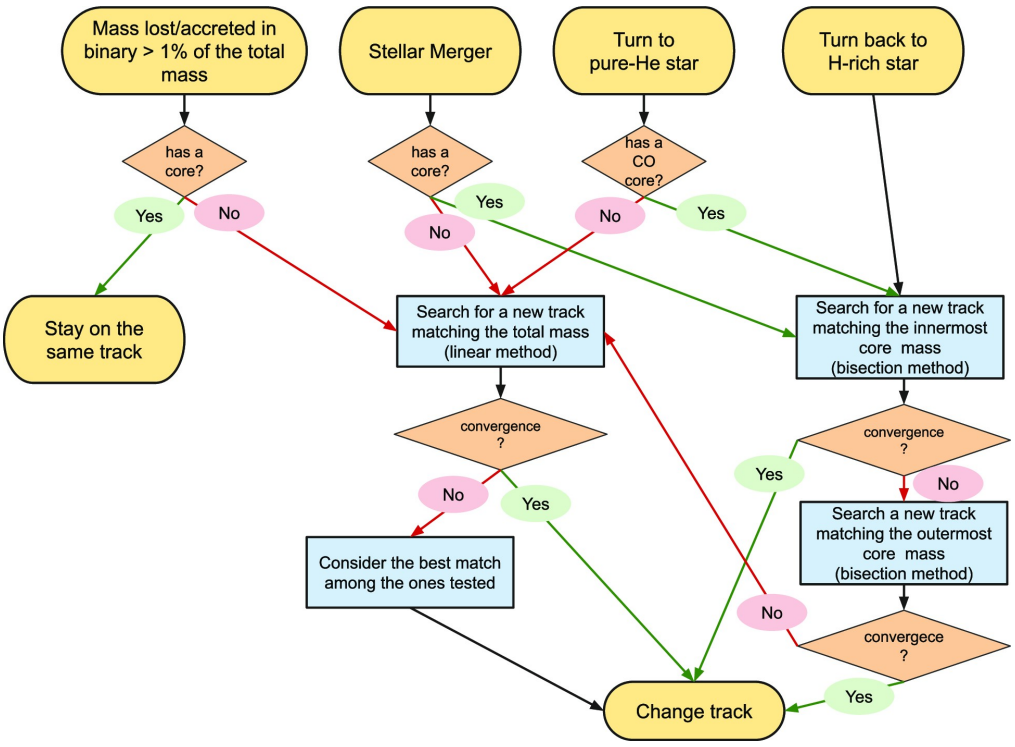

Figure 4.4: Schematic representation of the algorithm SEVN uses during a change of stellar track. The elements in the upper row indicate all the cases for which the code searches for a new stellar track: a significant mass-loss/mass accretion due to binary interactions, a stellar merger, an H-rich star that loses its envelope turning into a pure-He star, and a pure-He star that accretes a new H envelope turning back into a H-rich star. In stars with both an He and CO cores, the latter is the innermost core. In stars with only an He core the innermost and outermost cores coincide [83].

The properties of each star are estimated through interpolation. SEVN assigns four different tracks for each $(M_{\rm ZAMS}, Z)$ couple from the hydrogen or pure-He tables; they have two metallicities (Z_1, Z_2) and four $M_{\rm ZAMS}$, two for each metallicity, so that $M_{\rm ZAMS,1/3} \leq M_{\rm ZAMS} \leq M_{\rm ZAMS,2/4}$ and $Z_1 \leq Z \leq Z_2$. Then, a given property W is estimated as follows:

$$W = \frac{Z_2 - Z}{Z_2 - Z_1} W_{Z,1} + \frac{Z - Z_1}{Z_2 - Z_1} W_{Z,2}\,, \tag{4.23}$$

with

$$W_{Z,1} = \beta_1 W_{\rm ZAMS,1} + \beta_2 W_{\rm ZAMS,2}\,, \tag{4.24}$$

$$W_{Z,2} = \beta_3 W_{\rm ZAMS,3} + \beta_4 W_{\rm ZAMS,4}\,, \tag{4.25}$$

where $W_{\rm ZAMS,i}$ are the values of W in the interpolating tracks with $M_{\rm ZAMS,i}$ and β_i are the interpolation weights. When a star is initialised, these equations are used to set the starting times $t_{{\rm start},p}$ for each phase p and the stellar life-time is interpolated assuming that the last value in the table sets the total stellar life-time. For the other properties, W has to be estimated at a given t and the corresponding $W_{\rm ZAMS,i}$ is estimated at the same percentage of life in the interpolated star:

$$\Theta_p = \frac{t - t_{{\rm start},p}}{t_{{\rm start},p_{\rm next}} - t_{{\rm start},p}}\,, \tag{4.26}$$

where $t_{\mathrm{start},p}$ is the starting time of the phase p and $t_{\mathrm{start},p_{\mathrm{next}}}$ is the starting time of the following phase p_{next}. The time for each of the four interpolating tracks is

$$t_i = t_{\mathrm{start},p_i} + \Theta_p \, \Delta_{p_i} \, , \tag{4.27}$$

where t_{start,p_i} and $\Theta_p \, \Delta_{p_i}$ are the starting time and the duration of the current phase. Once evaluated the time, $W_{\mathrm{ZAMS,i}}$ can be computed by linear interpolation of the values stored in the tables.
When the evolution time passes the star life-time, a compact remnant is formed. SEVN triggers the formation of a white dwarf if the final mass of the CO-core is $M_{\mathrm{CO},f} < 1.38$ M$_\odot$, an electron capture SN if 1.38 M$_\odot \leq M_{\mathrm{CO},f} < 1.44$ M$_\odot$ or a CCSN is $M_{\mathrm{CO},f} \geq 1.44$ M$_\odot$. To handle PISNe and PPISNe the model M20 (Mapelli et al. 2020 [90]), which is the one used in the simulations presented in Chapter 5, can be adopted. It is based on the fit by Spera & Mapelli [10] to the BH mass obtained with 1D hydrodynamical simulations by Woosley [14], adopting the criterion based on the He-core mass illustrated in the previous chapters. While PISNe do not leave any compact remnant, the BH mass M_{PPISN} after a PPISN is given by applying a correction to the BH mass M_{CCSN} predicted by CCSN model: $M_{\mathrm{PPISN}} = \alpha_P \, M_{\mathrm{CCSN}}$. The correction parameter α_P depends on the mass of He-core and on the ratio between the He-core mass and the total mass in the pre-supernova stage; it can vary between 0 and 1. Following the results by Woosley, if $M_{\mathrm{PPISN}} < 4.5$ M$_\odot$, a PISN occurred and the mass of the compact remnant is set to 0.
When a compact remnant is formed, it received a natal kick after the supernova, which can be modelled through different formalisms in SEVN. For example, in the model Kσ265, the kick magnitude V_{kick} is produced from a Maxwellian distribution with 1D root-mean-square (rms) σ_{kick} and the direction is drawn from an isotropic distribution. The default 1D rms is $\sigma_{\mathrm{kick}} = 265$ km s^{-1} (Hobbs et al. 2005 [91]). Instead, in the model KGM20, the magnitude is estimated as follows:

$$V_{\mathrm{kick}} = f_{\mathrm{H05}} \, \frac{\langle M_{\mathrm{NS}} \rangle}{M_{\mathrm{rem}}} \, \frac{M_{\mathrm{ej}}}{\langle M_{\mathrm{ej}} \rangle} \, , \tag{4.28}$$

where f_{H05} is a random number from a Maxwellian distribution with $\sigma_{\mathrm{kick}} = 265$ km s^{-1}, $\langle M_{\mathrm{rem}} \rangle$ and $\langle M_{\mathrm{ej}} \rangle$ are the average neutron star mass and ejecta mass from single stellar evolution respectively, and M_{rem} and M_{ej} are the compact object mass and the ejecta mass (Giacobbo & Mapelli 2020 [92]). If the compact object is formed in a binary system, the natal kick changes the orbital properties, the relative orbital velocity and the centre of mass (Hurley et al. 2002 [43]). In SEVN, the binary properties are updated after a kick: if the semi-major axis is smaller than 0 or the eccentricity larger than 1, the binary does not survives the kick.
The binary evolution is performed by means of analytic and semi-analytic methods: wind mass transfer follows the implementation by Hurley (Eq. 2.26); RLOF begins whenever the radius of one of the stars is equal to its own Roche-lobe radius and stops when this condition is no more satisfied or the mass transfer leads to merger or CE; the CE evolution is based on the α formalism depicted in Section 2.3.2. SEVN takes into account also the semi-major axis and eccentricity time evolution due to gravitational waves including the same formalism of BSE code [43], depending on the eccentricity e, the semi-major axis a and the masses of the components $M_{1,2}$:

$$\dot{a} = - \, \frac{64 \, G^3 \, M_1 \, M_2 \, (M_1 + M_2)}{5 \, c^5 \, a^3 \, (1 - e^2) \left(\frac{7}{2}\right)} \left(1 + \frac{73}{24} \, e^2 + \frac{37}{96} \, e^4\right) , \tag{4.29}$$

$$\dot{e} = - \, \frac{304 \, G^3 \, M_1 \, M_2 \, (M_1 + M_2)}{15 \, c^5 \, a^4 \, (1 - e^2) \left(\frac{5}{2}\right)} \left(1 + \frac{121}{304} \, e^2\right) e \, . \tag{4.30}$$

The effect of the tidal forces on the orbit and stellar rotation is taken into account following the weak friction analytic models by Hut (1981 [93]) as implemented by Hurley et al. (2002 [43]). In particular, the model is based on the spin-orbit coupling by the misalignment of the tidal bulges in a star and the perturbing potential generated by the companion. The corresponding equations implemented in SEVN are the following:

$$\dot{a} = - \, 6 \, k_{\mathrm{tides}} \, q \, (q + 1) \left(\frac{R_{\mathrm{eff}}}{a}\right)^8 \frac{a}{(1 - e^2)^{7.5}} \left[f_1 - (1 - e^2)^{2/3} \, f_1 \, \frac{\Omega_{\mathrm{spin}}}{\Omega_{\mathrm{orb}}} \right] , \tag{4.31}$$

$$\dot{e} = -27\, k_{\rm tides}\, q\,(1+q)\left(\frac{R_{\rm eff}}{a}\right)^8 \frac{e}{(1-e^2)^{6.5}}\left[f_3 - \frac{11}{18}(1-e^2)^{2/3}\, f_4\, \frac{\Omega_{\rm spin}}{\Omega_{\rm orb}}\right], \tag{4.32}$$

$$\dot{J} = 3\, k_{\rm tides}\, q^2\, M\, R^2 \left(\frac{R_{\rm eff}}{a}\right)^6 \left(\frac{R_{\rm eff}}{R}\right)^2 \frac{\Omega_{\rm orb}}{(1-e^2)^6}\left[f_2 - (1-e^2)^{2/3}\, f_5\, \frac{\Omega_{\rm spin}}{\Omega_{\rm orb}}\right], \tag{4.33}$$

where $\Omega_{\rm spin}$ is the stellar angular velocity, R and M are the stellar radius and mass, $R_{\rm eff} = \min[R_L, R]$ is the minimum between the stellar radius and the Roche-lobe radius, the f_i are the polynomial functions of e^2 given by Hut (1981 [93]) and $k_{\rm tides}$ is the inverse of the timescale of tidal evolution. The term $k_{\rm tides}$ takes the different forms in the case of radiative envelopes (Zahn 1975 [94], 1975 [95], Hurley et al. 2002 [43]; Eq. 4.34) or convective envelopes (Zahn 1977 [95], Hurley et al. 2002 [43]; Eq. 4.35):

$$k_{\rm tides} = 3.156 \times 10^{-5} \left(\frac{M}{\rm M_\odot}\right)^{3.34} \left(\frac{R}{\rm R_\odot}\right) \left(\frac{a}{\rm R_\odot}\right)^{-2.5} \ {\rm yr}^{-1}, \tag{4.34}$$

$$k_{\rm tides} = \frac{2}{21}\left(\frac{\tau_{\rm conv}}{\rm yr}\right)^{-1} \left(\frac{M_{\rm conv}}{M}\right) \min\left\{1, \left(\frac{\pi}{(\Omega_{\rm orb} - \Omega_{\rm spin})\,\tau_{\rm conv}}\right)^2\right\} \ {\rm yr}^{-1}, \tag{4.35}$$

where $M_{\rm conv}$ is the mass of the convective envelope and $\tau_{\rm env}$ is the eddy turnover timescale.
When two stars merge, CO-cores, He-cores and total masses are summed and the result of the merger is assumed to be in the phase and percentage life of the most evolved progenitor star.

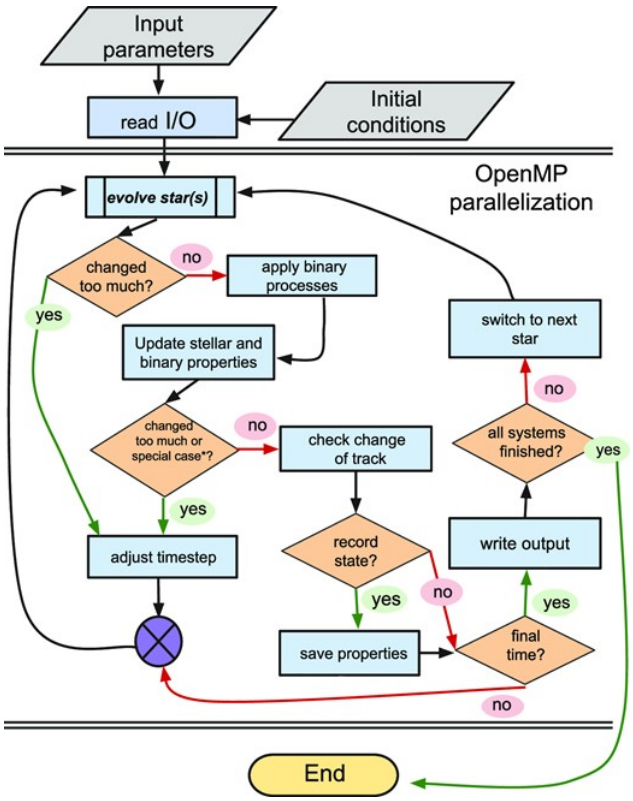

Figure 4.5: Schematic representation of the SEVN evolution algorithm. The 'changed too much' checks refer to the variation of the stellar and/or binary properties. In the case of single-stellar evolution or in the case of an ionized binary, SEVN skips the sections 'apply binary processes' and 'update stellar and binary properties'. The 'special case' check refers to all the cases in which SEVN repeats the evolution to follow a particular binary evolution process, i.e. CE, merger, and circularization at the onset of the RLOF [83].

To adapt the time-step, SEVN uses a prediction-correction method accounting for the large physical range of timescales typical of stellar and binary evolution: it looks at a sub-set of stellar and binary properties and if any of them changes too much during a time-step, the time-step is reduced and the calculation repeated. In practice, a maximum relative variation δ_{max} is chosen and it is imposed that

$$\max_{P \in \text{properties}} |\delta\, P| \leq \delta_{\rm max}\,, \tag{4.36}$$

where $|\delta P|$ is the absolute value of the property relative variation. Then, SEVN predicts the next time-step as

$$dt_{\rm next} = \min_{P\in \text{ properties}} \left(\delta_{\rm max}, \frac{dt_{\rm last}}{|\delta P_{\rm last}|}\right), \tag{4.37}$$

where $dt_{\rm last}$ is the last time-step, $|\delta P_{\rm last}|$ is the relative variation of property P during the last time-step and $\frac{dt_{\rm last}}{|\delta P_{\rm last}|}$ represents the absolute value of $\delta P_{\rm last}$ time derivative. If the condition in Eq. 4.36 is not met, a smaller step is computed with Eq. 4.37. Instead, when the star approaches a change of phase, the treatment is different: if the time-step is large enough to cross the time-boundary between two phases, it is automatically reduced so that the next evolution step is brought to 10^{-10} Myr before the phase change; the next time-step, instead, is set such that it brings the star/binary 10^{-10} Myr beyond the phase change. In this way stellar properties are evaluated just before and after the phase change. A schematic representation of the SEVN evolution algorithm is reported in Fig. 4.5.
TRACKCRUNCHER (Iorio et al. 2023 [83]) has been used to produce the stellar tables from the MESA tracks I computed. TRACKCRUNCHER is a code that extracts the main properties of the stars to store them in the SEVN tables, while estimating the starting time of the SEVN phases. It can be easily extended to process also the outputs of MESA.

4.3 Evolution Across Cosmic Time

In the previous sections, I described the stellar evolution and population synthesis codes I used to obtain catalogues of single stellar populations. Thanks to these data and their analysis, it is possible to achieve information on systems of our interest and, in particular, on PISNe and PPISNe. The main goal of the thesis is to model the evolution of PISN and PPISN rate density across the Universe history to understand how much these processes were common at high redshift and which is their relevance in the Local Universe. Once obtained the catalogues thanks to the population synthesis code SEVN, the next step is to combine them with data-driven prescription for the cosmic evolution of the star formation rate (SFR) and metallicity.

4.3.1 Cosmic Star Formation Rate Density

To obtain the star formation history of galaxies, we have to infer mass from light. Actual surveys allow us to study the emission of galaxies at different wavelengths and extrapolate the rate at which stars are formed in the galaxy. Almost all the observational tracers of star formation should measure the formation rate of massive stars, since massive stars emit most of the energy measured from a young stellar population. However, various observational tracers are sensitive to different ranges of stellar masses, leading them to react differently depending on the age of the stellar population. The wavelength regimes usually studied to estimate SFR and SFR density (SFRD) are the UV and IR. Analysing the data by the surveys, it is possible to obtain the best-fit luminosity function parameters and multiply the luminosity density by properly calibrated conversion factors to finally estimate the SFRD. In the following, I describe the analysis by Harikane et al. (2022 [96]) to model the SFRD.
Harikane et al. presented new measurements of the rest-frame UV luminosity functions based on wide and deep optical images obtained in the Hyper Supreme Cam (HSC) Subaru Strategic Program (SSP) survey (Aihara et al. 2018 [97]) and the CFHT Large Area U-band Deep Survey (CLAUDS; Sawicki et al. 2019 [98]). Fig. 4.6 shows their fit of the halo mass M_h as function of the UV magnitude $M_{\rm UV}$:

$$M_h = \frac{M_{h,0}}{2}\left[10^{-0.4(M_{\rm UV}-M_{\rm UV,0})\alpha} + 10^{-0.4(M_{\rm UV}-M_{\rm UV,0})\beta}\right], \tag{4.38}$$

with

$$M_{\rm UV} = m + 2.5\,\log(1+\bar{z}) - 5\,\log\left(\frac{d_L(\bar{z})}{10\,pc} + (m_{\rm UV} - m)\right), \tag{4.39}$$

where $\bar{z}$ is the average redshift, d_L is the luminosity distance, $(m_{\rm UV} - m)$ is a correction factor due to the band they used, $M_{h,0}$ and $M_{\rm UV,0}$ are the characteristic halo and UV magnitudes, α and β are faint and bright-end power-law slope.

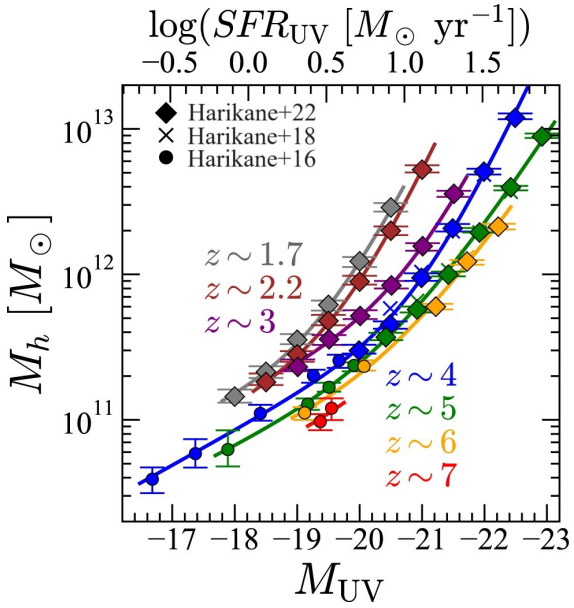

Figure 4.6: The gray, brown, purple, blue, green, orange, and red filled diamonds (circles) denote the halo masses as a function of the UV magnitude at z ∼ 1.7, 2.2, 3, 4, 5, 6, and 7, respectively. The crosses are results from the previous works based on the early HSC-SSP data. The solid curves show the best-fit relations of Eq. 4.38 [96].

Using the calibration factor in Madau & Dickinson (2014 [99]), the SFR in UV can be derived as follows:

$$SFR_{\rm UV} = 1.15 \times 10^{-28} \frac{L_{\rm UV}}{\rm erg\ s^{-1}\ Hz^{-1}} {\rm M_\odot\ yr^{-1}}\,, \tag{4.40}$$

where L_{UV} is the luminosity in the UV. Finally, the cosmic SFRD can be estimated using:

$$\rho_{\rm SFR} = \int d\,M_h \frac{d\,n}{d\,M_h}\,{\rm SFR} = \int d\,M_h \frac{d\,n}{d\,M_h}\,\dot{M}_h \frac{\rm SFR}{\dot{M}_h}\,, \tag{4.41}$$

where $\frac{d\,n}{d\,M_h}$ is the halo mass function and

$$\frac{\rm SFR}{\dot{M}_h} = \frac{2 \times 3.2 \times 10^{-2}}{(M_h/10^{11.5})^{-1.2} + (M_h/10^{11.5})^{0.5}}\,. \tag{4.42}$$

The final fitting formula they found is the following:

$$\rho_{\rm SFR} = \left[61.7 \times (1-z)^{-3.13} + 10^{0.22(1+z)} + 2.4 \times 10^{0.5(1+z)-3}\right]^{-1} [{\rm M_\odot\ yr^{-1}\ Mpc^{-3}}]. \tag{4.43}$$

It represents an important upgrade with respect to previous works (e.g. Madau & Dickinson, 2014 [99], gray dashed line in Fig. 4.7), which predicted an higher $\rho_{\rm SFR}$ at high redshift, and, as shown in Fig. 4.7, fits better the available data.

4.3.2 Metallicity Evolution

Metallicity evolution is another fundamental aspect to study the evolution of PISN and PPISN rate density across cosmic time: higher metallicities lead to higher mass-loss rates and lower He-core masses. To understand it, it is essential to know the chemical composition for high-redshift galaxies. The high-redshift Universe is occupied by populations of objects spanning a wide range of metallicities from [Z/H] ∼ 0, like quasars, to [Z/H] = −3, like the Ly-α forest clouds: systems with mean metal abundance between these two extremes are the damped Ly-α absorption systems (DLAs) and a lot of studies used them to reconstruct the metallicity evolution in the Universe history (De Cia et al. 2018 [100]).
However, metallicity strongly affects the number and luminosity of high-mass X-ray binaries (HMXBs),

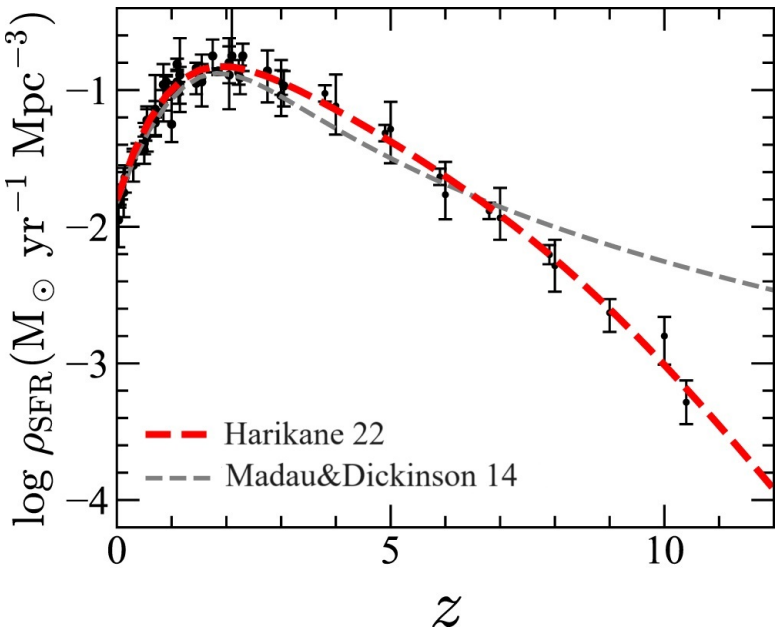

Figure 4.7: Fit to the observed cosmic SFR densities. The red dashed curve represents the fit (Eq. 4.43) to the observed cosmic SFR densities at z $\leq$ 10 and the calculated SFR densities at z $\geq$ 10 in Harikane et al. (2022 [96]). The gray dashed curve shows the fit in Madau & Dickinson (2014 [99]) [96].

due to the dependency of OB star mass-loss on the metal content. The gas-phase oxygen abundance is known to correlate with stellar mass in star-forming galaxies with a mass-metallicity (MZ) relation that extends down to $M_* \sim 10^6$ M$_\odot$ and up to redshift z $\sim$ 3.5:

$$12 + \log(O/H) = Z_0 + \log\left[1 - \exp\left(-\left(\frac{M_*}{M_0}\right)^\gamma\right)\right], \tag{4.44}$$

where Z_0 is the saturation metallicity, M_0 the characteristic turnover mass above which the metallicity asymptotically tends to Z_0 and $\gamma \sim 0.513$.
Madau & Fragos (2017 [101]) assumed that the MZ relation by Zahid et al. (2014 [102]; Eq. 4.44) holds at all redshift and integrated it over the evolving galaxy stellar mass function to compute a mean mass-weighted gas-phase metallicity at $z = 0.03$ (Baldry et al. 2012 [103]) and over the redshift ranges $0.35 < z < 3.5$ (Ilbert et al. 2013 [104]), $0.75 < z < 3$ (Kajisawa et al. 2009 [105]), $4 < z < 5$ (Lee et al. 2012 [106]) and $3.5 < z < 7.5$ (Grazian et al. 2015 [107]). The final fitting formula is reported in the following (Eq. 4.45) and the evolution of $\log\langle Z/Z_\odot\rangle$ as function of the redshift is shown in Fig. 4.8:

$$\log\langle Z/Z_\odot\rangle = 0.153 - 0.074\, z^{1.34}\,. \tag{4.45}$$

4.3.3 COSMORATE

As said at the beginning of Section 4.3, the aim of this work is to combine the SEVN results with data-driven prescriptions for SFRD and metallicity evolution. This can be done thanks to the semi-analytic code COSMORATE by Santoliquido et al. (2020 [108], 2021 [109]) that is computationally optimised to extensively probe the parameter space of SFRD and metallicity evolution.
COSMORATE basically computes the following integrals:

$$R(z) = \frac{d}{d\, t_{\rm lb}(z)}\left[\int_{z_{\rm max}}^{z} \psi(z')\,\frac{d\, t_{\rm lb}(z')}{d\, z'}\, d\, z' \int_{Z_{\rm min}}^{Z_{\rm max}} \eta(Z)\, F(z', z, Z)\, d\, Z\right], \tag{4.46}$$

that gives us the rate density of an event as function of the redshift. COSMORATE was meant to evaluate the merger rate density of compact binaries, but it can be easily customized to obtain the PISN and PPISN rate density; so, $t_{\rm lb}(z)$ is the look-back time at redshift z, $Z_{\rm min}$ and $Z_{\rm max}$ are the

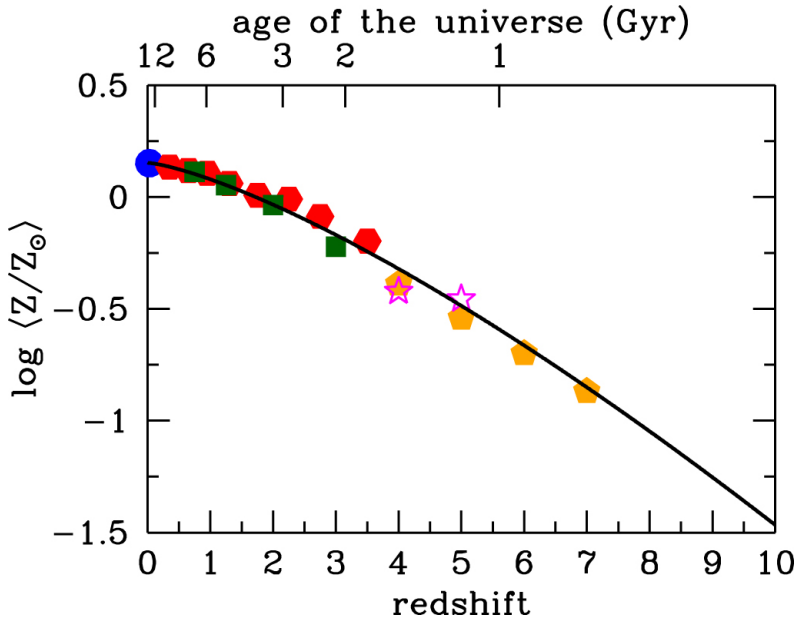

Figure 4.8: Gas-phase metallicity history of the galaxy population as a whole. The mass-weighted metallicity has been computed by integrating the mass–metallicity relation of Zahid et al. [102] over the evolving galaxy stellar mass function of Baldry et al. (2012 [103]; blue dot), Ilbert et al. (2013 [104]; red exagons), Kajisawa et al. (2009 [105]; green squares), Lee et al. (2012 [106]; magenta stars) and Grazian et al. (2015 [107]; orange pentagons) [101].

minimum and maximum metallicity we are using, $\psi(z')$ is the cosmic SFRD at redshift z', $F(z', z, Z)$ is the fraction of systems undergoing PISN/PPISN that formed at redshift z' from stars with metallicity Z and exploding at redshift z and $\eta(Z)$ is the PISN/PPISN efficiency.
The efficiency is estimated as follows:

$$\eta(Z) = f_{\rm bin}\, f_{\rm IMF}\, \frac{N_{\rm TOT}(Z)}{M_*(Z)}\,, \tag{4.47}$$

where $N_{\rm TOT}$ is the total number of systems exploding within an Hubble time, M_* is the total initial mass of the simulation, $f_{\rm bin}$ is the binary fraction, $f_{\rm IMF}$ is a correction factor that takes into account that only stars with mass higher than a certain threshold are simulated. The SFRD I used is the fitting formula found by Harikane et al. (2022 [96]) and reported in Eq. 4.43. The SFRD is then multiplied by a correction factor $f_{\rm Kroupa} = 0.66$ to convert the SFRs from a Salpeter IMF to a Kroupa IMF (Madau & Dickinson 2014 [99]). The function $F(z', z, Z)$ involves the average metallicity evolution deepened in the previous section; I used the fitting formula found by Madau & Fragos (2017 [101]; Eq. 4.45). The distribution of stellar metallicities $\log(Z/Z_\odot)$ at a given redshift is modelled through a normal distribution with a mean value $\mu(z)$ from Eq. 4.45 and standard deviation $\sigma_Z = 0.4$:

$$p(z', Z) = \frac{1}{\sqrt{2\,\pi\,\sigma_Z^2}}\, \exp\left\{ -\, \frac{[\log(Z/Z_\odot - \mu(z'))]^2}{2\,\sigma_Z^2} \right\}. \tag{4.48}$$

Then, the fraction of systems undergoing PISN/PPISN that form at redshift z' from stars with metallicity Z and explode at redshift z is given by

$$F(z', z, Z) = \frac{N(z', z, Z)}{N_{\rm TOT}(Z)}\, p(z', Z)\,, \tag{4.49}$$

where $N(z', z, Z)$ is the number of systems undergoing PISN/PPISN that form at redshift z' from stars with metallicity Z and explode at redshift z.
$F(z', z, Z)$ and $\eta(Z)$ are the functions which require the information from population synthesis catalogues: the mandatory input parameters are the total initial mass of the simulation M_*, needed to estimate the efficiency $\eta(Z)$, and the delay times of each system in the catalog, e.g. the life-time of the star before experience PISN/PPISN.

Chapter 5

Simulations and Results

In this Chapter, I present the simulations I performed and the main results of this work.
In particular, I describe the MESA setup used to model VMSs and massive binaries. MESA has been used to produce tracks for the rapid population synthesis code SEVN. Finally, the SEVN results have been combined with data-driven prescription for cosmic star formation rate and metallicity evolution by feeding the semi-analytical code COSMORATE with suitable catalogues. The obtained PISN and PPISN rate density, the most important results of this work, are then shown and discussed.

5.1 MESA Setup

The VMS models presented in this Chapter are calculated with the MESA version r12115 (Paxton et al. 2011 [33], 2013 [34], 2015 [35], 2018 [36], 2019 [37]). The setup I used is similar to the one published by Sabhahit et al. (2023 [38]) and available at the following link: `https://github.com/Apophis-1/VMS_Paper2`.
The MLT by Cox & Giuli (1968 [76]), described in Section 4.1.1, is used to treat convective mixing, adopting $\alpha_{\rm MLT} = 1.5$. To set the convective boundaries, the Ledoux criterion is applied (Ledoux, 1947 [74]; Section 4.1.1). This allows for semi-convective regions to form above the convective core due to the chemical gradient formed by the receding core during the MS. In these regions, convection can be so slow that it only transports a small amount of energy, but nevertheless leading to a homogeneous composition in the intermediate layer between the convective core and the radiative envelope. A semi-convective diffusion parameter $\alpha_{\rm SC} = 1$ is used (Sabhahit et al. 2022 [32], 2023 [38]). The model to treat semi-convection is very similar to MLT and $\alpha_{\rm SC}$ can be seen as the efficiency of this process. Even if the convective boundaries are set by the condition that the acceleration of the convective elements goes to zero, this does not mean that these elements have zero velocity at the core boundary. Indeed, these elements can over-shoot above (or below) the convective boundary and penetrate into the radiative regions with a non-zero velocity. The exponential overshooting by Herwing (2000 [110]) has been chosen to describe the overshooting above the convective regions with efficiency parameter $f_{\rm OV} = 0.03$. The diffusion coefficient in the overshooting regions is defined as:

$$D_{\rm OV} = D_O \, \exp\left[\frac{-2\,(r - r_O)}{f_{\rm OV}\, H_P}\right], \tag{5.1}$$

where D_O is the diffusion coefficient at the start of the overshooting region defined at location r_O just below the convective boundary, $f_{\rm OV}$ defines the inverse slope of the diffusion decay expressed in terms of the pressure scale height H_P.
The initial masses range from 50 $M_\odot$ to 500 $M_\odot$ by intervals of 25 $M_\odot$ and the initial metallicities are Z = 0.008, 0.006, 0.004, 0.002, 0.001, 0.0008, 0.0006, 0.0004, 0.0002, 0.0001; so, the grid consists of 19×10 models (19 different initial masses and 10 different initial metallicities). The metallicities have been chosen to properly study the low metallicity regime and investigate the metallicity threshold above which PISNe and PPISNe cannot occur: this boundary is usually set to $Z = 0.008$ (Spera

& Mapelli 2017 [10]), but the new model by Sabhahit et al. (2023 [38]) lowers this boundary to $Z \sim 0.002$.
For all the models, the initial He mass fraction Y is calculated as $Y = Y_{\rm prim} + \frac{\Delta Y}{\Delta Z} Z$, where $Y_{\rm prim}$ is the primordial He abundance and $\frac{\Delta Y}{\Delta Z}$ is parameterized to span the range between an approximately primordial chemistry ($X = 0.76$, $Y = 0.24$, $Z = 0$), and a quasi-solar abundance ($X = 0.70$, $Y = 0.28$, $Z = 0.02$). Both $Y_{\rm prim}$ and $\frac{\Delta Y}{\Delta Z}$ follow the default values in MESA (Pols et al. 1998 [84]), so $Y_{\rm prim} = 0.24$ and $\frac{\Delta Y}{\Delta Z} = 2$. The H mass fraction X is then given by $X = 1 - Y - Z$.
During the MS, the mass-loss framework detailed in Section 2.2.3 is used; while during the He-burning phase, it is used only for temperatures between 4×10^3 K and 10^4 K; for temperatures below 4×10^3 K, the recipe by de Jager (1988 [5]) is implemented; for temperatures higher than 10^4 K and H mass fraction lower than 0.01, the WR mass-loss recipe by Sander & Vink (2020 [111]) is adopted.
Finally, the MLT++ option is turned on only during the He-burning phase to ensure the convergence. However, the main focus of Sabhahit et al. (2023 [38]) was not the study of the advanced evolutionary phases, which are, instead, needed to obtain a more complete comprehension of the pair-instability regime and to produce tracks suitable for SEVN; so, I modified their `inlist` files to achieve this aim. In particular, I changed the definition of the core boundary and the nuclear reaction network:

- `he_core_boundary_h1_fraction = 1d-4` (MESA default: 0.1);
- `c_core_boundary_he4_fraction = 1d-4` (MESA default: 0.1);
- `o_core_boundary_c12_fraction = 1d-4` (MESA default: 0.1);
- `min_boundary_fraction = 1d-4` (MESA default: 0.1);
- `auto_extend_net = true` (MESA default: `false`).

Sabhahit et al. (2023 [38]) adopted the `basic` nuclear reaction network which includes only 8 isotopes (H, ^{3}He, ^{4}He, ^{12}C, ^{14}N, ^{16}O, ^{20}Ne, ^{24}Mg) and assumes that the temperature is low enough to ignore advanced burning. I decided to use `auto_extend_net` which switches from `basic` to `co_burn` (which includes also ^{28}Si) after the MS to have a more complete and extended network for C- and O-burning and α-chains.
The evolution is followed until the luminosity due to carbon burning L_C is less than the 20% of the total luminosity $L_{\rm TOT}$ ($L_C/L_{\rm TOT} < 0.2$) and He central abundance Y_c is lower than 10^{-8}. The final requirement to produce the tracks is to have at least three CO-core mass points, so that the first one is used to set the terminal He burning phase, the second one to set the He shell burning phase, the last one is used as last point of the track.
In addition, I also modelled binary systems, varying the orbital period ($P_{\rm orb} = 30$ d, 15 d, 10 d). The initial mass of the accretor star is always fixed to 50 $M_\odot$, while the initial mass of the donor rages from 150 $M_\odot$ to 400 $M_\odot$ by intervals of 50 $M_\odot$. Two different metallicities have been considered: $Z = 0.004$, 0.001. The initial eccentricity is always set to 0. The binary system with initial donor mass $M_{\rm donor} = 100$ $M_\odot$ is presented only for orbital period $P_{\rm orb} = 30$ d and metallicity $Z = 0.004$.
In MESA, three different `inlist` files are necessary to model a binary system: two files to evolve the single stars (one for each component) and an additional one to interface the evolution of the components and set the prescriptions to model the binary interaction. In particular, I used the Kolb scheme (Kolb & Ritter, 1990 [81]; Eq. 4.14) to model the mass transfer and decided to relax the time-step controls to facilitate the convergence. However, none of the models at $Z = 0.001$ reached the end of the simulation, since the mass transfer became unstable and MESA cannot handle it anymore. The same happened to models with initial mass of the donor star $M_{\rm donor} = 200$ $M_\odot$ and orbital period $P_{\rm orb} = 15$ d, 10 d at metallicity $Z = 0.004$.
The `inlist` files used to evolve the components are the ones described before to model single stars. In all the models, the evolution is followed until the central H abundance X_c of one of the two components is lower than 0.01.
The `inlist` files I used to evolve VMSs during the MS (`inlist_project_H`), the He-burning phase (`inlist_project_He`) and in binary systems (`inlist_project_bin`) are reported in the Appendix: MESA Inlist Files.

5.2 Single Star Models

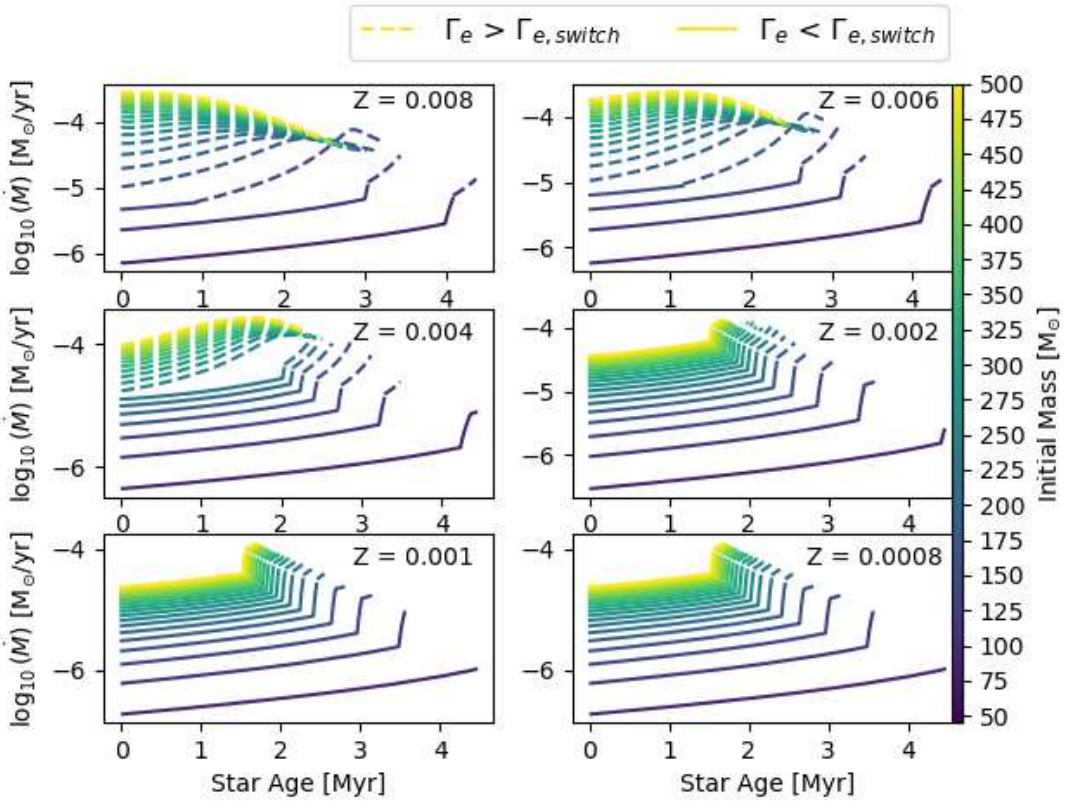

Figure 5.1: Time evolution of the mass-loss rate in $M_\odot$ yr^{-1}: $Z = 0.008$ models are presented in the top-left panel; $Z = 0.006$ models in the top-right panel; $Z = 0.004$ models in the central-left panel; $Z = 0.002$ models in the central-right panel; $Z = 0.001$ models in the bottom-left panel; $Z = 0.0008$ models in the bottom-right panel. The dashed lines highlight the evolutionary phase in which the stars enter the optically-thick regime ($\Gamma_{\rm Edd} > \Gamma_{\rm Edd,\ switch}$).

In this section, I present the mass-loss rate evolution, the mass evolution, the HR diagram tracks and the radius evolution of the single stellar models until the end of the MS. Then, I report also the HR diagram tracks and the evolution of the He core mass until the end of the simulation. In addition, I also discuss some issues in modelling the transition between the MS and the He-burning phase. In all the following plots, if not specified in the caption, the colors represent the initial stellar mass, which can range from 50 $M_\odot$ to 500 $M_\odot$. In order to make the plots more understandable and clear, models at $Z = 0.0006, 0.0004, 0.0002, 0.0001$ are not here reported since their evolution is very similar to the one at $Z = 0.0008$.

Fig. 5.1 shows the evolution of the mass-loss rate with the time at different metallicities ($Z = 0.008, 0.006, 0.004, 0.002, 0.001, 0.0008$). Two fundamental parameters affect the mass-loss rate value: the metallicity and the luminosity-to-mass ratio (Section 2.2.3). The dashed lines highlight the evolutionary phase in which the stars enter the enhanced winds regime ($\Gamma_{\rm Edd} > \Gamma_{\rm Edd,\ switch}$) and it is evident from these plots the impact of the metallicity and the mass on when this can happen. Indeed, during the MS, the initial mass required to enter this regime grows decreasing the metallicity: at $Z = 0.0008$, models with $M_{\rm init} \leq 125$ $M_\odot$ do not experience optically-thick winds; at $Z = 0.008$, even the 50 $M_\odot$ and 75 $M_\odot$ (classified as massive stars) experience enhanced winds.

When stars, which begin their life with $\Gamma_{\rm Edd} < \Gamma_{\rm Edd,\ switch}$ (e.g. models with masses 50 $M_\odot \leq M_{\rm init} \leq$ 200 $M_\odot$ at $Z = 0.004$), experience optically-thick winds, a boost in the mass-loss rate is present. Instead, the mass-loss rate of stars, which begin their life with $\Gamma_{\rm Edd} > \Gamma_{\rm Edd,\ switch}$ (e.g. models with masses 225 $M_\odot \leq M_{\rm init} \leq$ 500 $M_\odot$ at $Z = 0.004$), reaches a peak of $\sim 10^{-3.5}$ $M_\odot$ yr^{-1} and then starts to decrease. As aforementioned, the mass of the star plays an important role on evaluating $\dot{M}$ and a huge mass loss translates in a lower $\dot{M}$ at the end of the MS.

An higher mass-loss rate obviously translates into a larger amount of mass lost: as shown in Fig. 5.2,

at higher metallicities ($Z = 0.008, 0.006, 0.004$), where the winds are more efficient, the more massive stars can end their MS with a total mass lower than the least massive star in the grid (e.g. see 500 $M_\odot$, yellow line, and 50 $M_\odot$, dark violet line, models at $Z = 0.008$ in the top-left panel of Fig. 5.2). This has important consequence on the PISN and PPISN rate density: indeed at higher metallicities, even the more massive stars can end their life with a He mass core $M_{\rm He} < 32\ M_\odot$ and avoid the pair-instability regime.

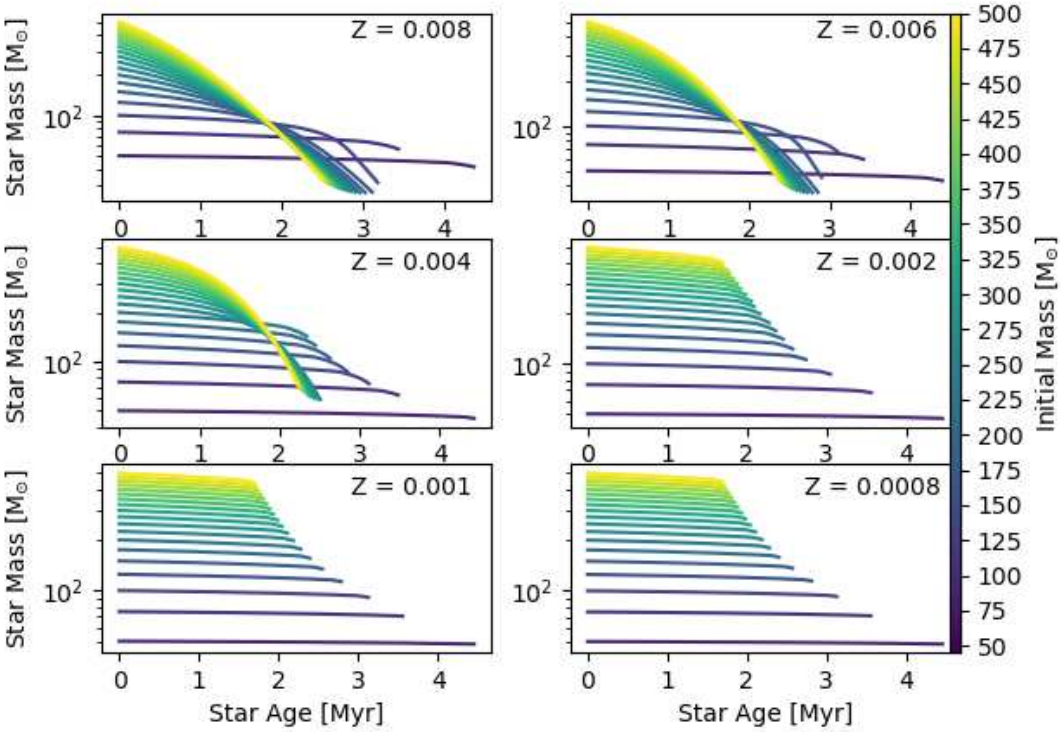

Figure 5.2: Evolution of the stellar mass as function of time in $M_\odot$: $Z = 0.008$ models are presented in the top-left panel; $Z = 0.006$ models in the top-right panel; $Z = 0.004$ models in the central-left panel; $Z = 0.002$ models in the central-right panel; $Z = 0.001$ models in the bottom-left panel; $Z = 0.0008$ models in the bottom-right panel.

In Fig. 5.3, the HR diagram tracks until the end of the MS are reported. All the models at low metallicities ($Z = 0.002$, 0.001, 0.0008) basically use the low-$\Gamma_{\rm Edd}$ winds (see Section 2.2.3) during all the MS, but in the very last period. These models evolve horizontally in the HR diagram towards cooler temperatures and the mass loss is not high enough to cause the drop in luminosity. Certain models at higher metallicities, e.g. the $M_{\rm init} = 100\ M_\odot$ model at $Z = 0.008$ (top-left panel in Fig. 5.3) or the $M_{\rm init} = 125\ M_\odot$ model at $Z = 0.006$ (top-right panel in Fig. 5.3), increase gradually their luminosity-to-mass ratio, entering the high-$\Gamma_{\rm Edd}$ regime, and are shifted to the blue. At these Z, the more massive stars switch to the high-$\Gamma_{\rm Edd}$ regime just after the ZAMS and mark the boundary of the two different evolutionary behaviours: indeed, these models experience a vertical evolution in the HR diagram, steeply decreasing their luminosity, but spanning a very narrow range of temperatures.
The new stellar wind model by Sabhahit et al. (2022 [32], 2023 [38]) affects also the stellar structure. One problem of modelling VMSs was the inflation of the radius at temperatures lower than the massive stars in contradiction with the observations (see discussion in Section 2.1.3 and Section 4.1.1). Now, the boosted mass-loss rate can self-regulate the radius inflation during the MS. In Fig. 5.4, the time evolution of the stellar radius is shown. The radii of stars, which enter the enhanced wind regime immediately after the ZAMS, rapidly decrease as a consequence of the large amount of the mass lost: indeed, in these cases, the H envelope is quickly lost and mass from the inner region of the star is emitted. Then, in the models which switch to high-$\Gamma_{\rm Edd}$ during the MS, the radius reach the peak at ~ 2 Myr and then decreases. Finally, when the models enter this regime in the very last part of the MS, the mass-loss is not able to contrast the inflation and the radius grows up to $\log(R/R_\odot) \sim 3.5$ in

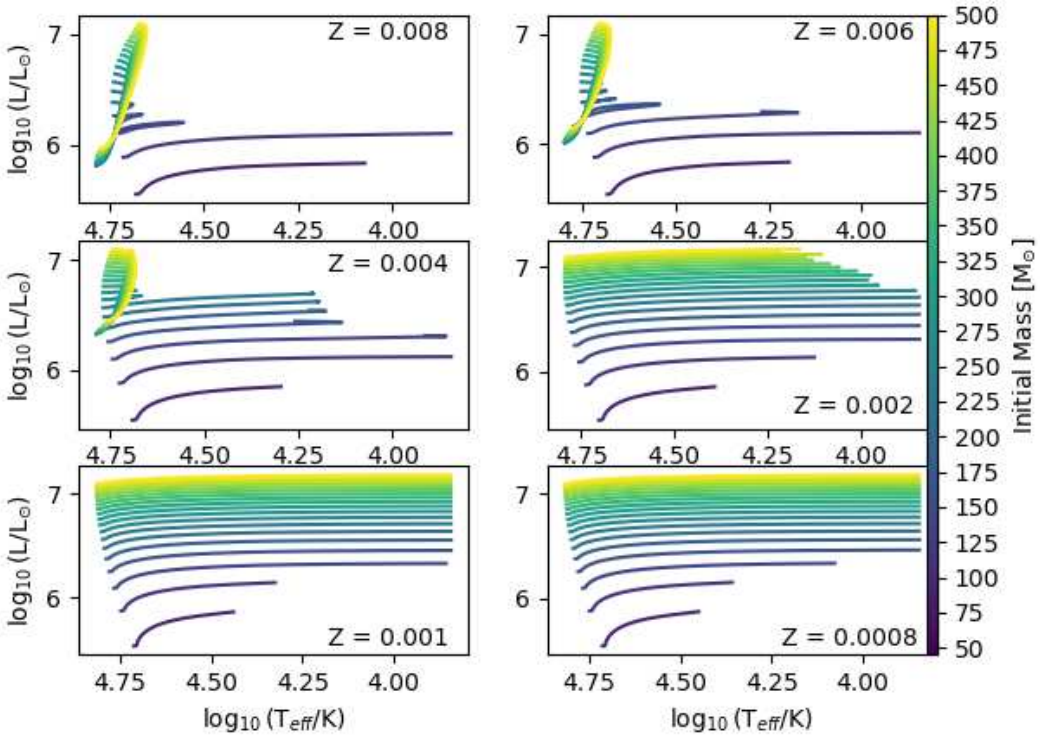

Figure 5.3: HR diagrams of the simulated models divided by metallicity: $Z = 0.008$ models are presented in the top-left panel; $Z = 0.006$ models in the top-right panel; $Z = 0.004$ models in the central-left panel; $Z = 0.002$ models in the central-right panel; $Z = 0.001$ models in the bottom-left panel; $Z = 0.0008$ models in the bottom-right panel.

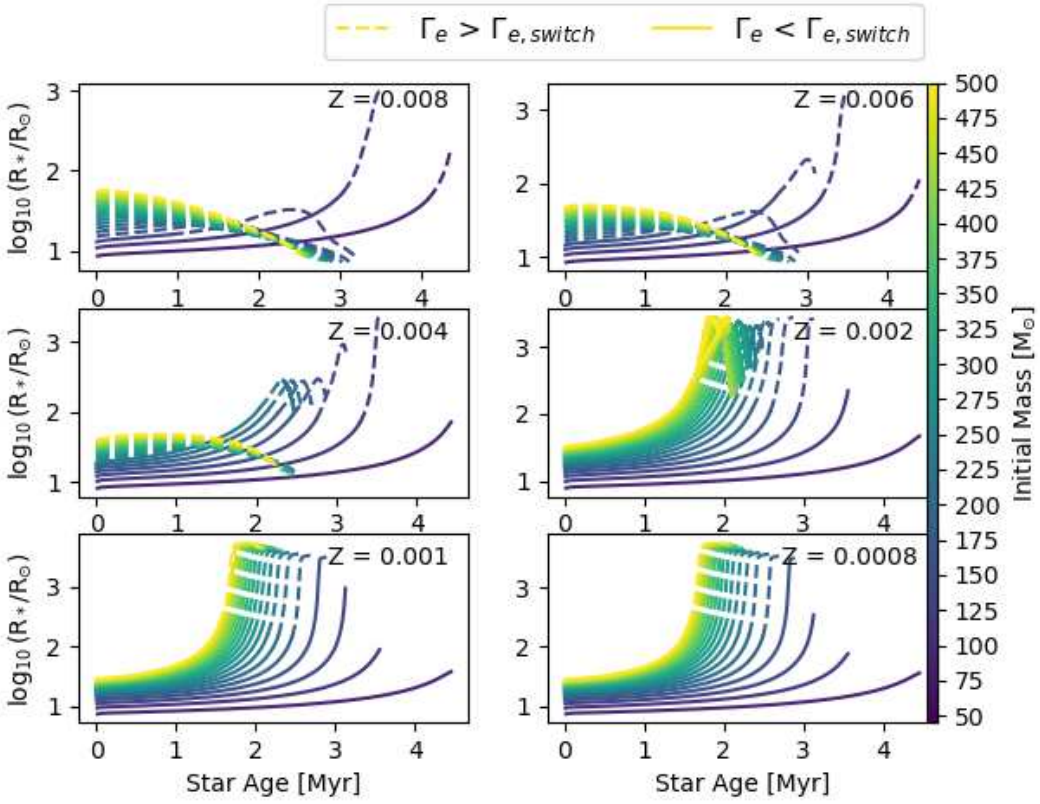

Figure 5.4: Time evolution of the radius in $R_\odot$: $Z = 0.008$ models are presented in the top-left panel; $Z = 0.006$ models in the top-right panel; $Z = 0.004$ models in the central-left panel; $Z = 0.002$ models in the central-right panel; $Z = 0.001$ models in the bottom-left panel; $Z = 0.0008$ models in the bottom-right panel. The dashed lines highlight the evolutionary phase in which the stars enter the optically-thick regime ($\Gamma_{\rm Edd} > \Gamma_{\rm Edd,\ switch}$).

a short timescale. This is the reason why it has been necessary to use the MLT++ option (Section 4.1.1) in the advanced evolutionary phases to ensure the convergence of all the models.
While activating the MLT++ option during the advanced evolutionary phases is useful to ensure the convergence of the model, it can produce inconsistencies in the evolution of some stellar properties. Fig. 5.5 shows the luminosity evolution with the time of the 75 $M_\odot$ model at $Z = 0.004$. The green dashed line represents the luminosity due to hydrogen burning, the blue line the luminosity due to helium burning, the red line the total luminosity. After $\sim$ 3.5 Myr, the total luminosity jumps instantaneously from $\log(L/L_\odot) \sim 6$ to $\log(L/L_\odot) \sim 7.4$. The jump corresponds to moment in which the MLT++ option is set to true (see Appendix: MESA Inlist Files). There are no evident physical reasons for the luminosity jump. It is likely related to a short re-adjustment phase of the stellar structure as a consequence of the change of MLT prescriptions. Indeed, without the MLT change the jump disappears, but the models do not converge. For his reason, we decided to remove the jump features from the tracks used to produce the SEVN tables

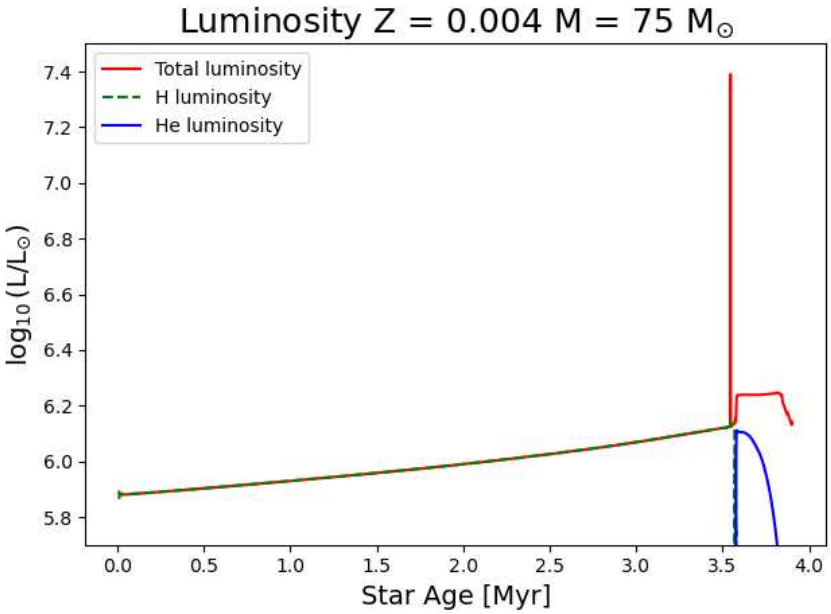

Figure 5.5: Time evolution of the luminosity of the $Z = 0.004$ and $M_{\rm init} = 75$ $M_\odot$ model. The red line indicates the total luminosity, the green line the luminosity due to hydrogen burning, the blue line the luminosity due to helium burning.

After the MS, all the models with $M_{\rm init} \geq 150$ $M_\odot$ enter the optically-thick wind regime and their tracks in the HR diagram move towards hotter temperatures. In Fig. 5.6, the tracks on the HR diagram of some models are reported. Not all the models are shown to make the plots more easily readable. At higher metallicities ($Z = 0.008, 0.004$) all the models, but one ($M_{\rm init} = 50$ $M_\odot$, $Z = 0.004$), move to the blue and enter the WR phase, ending their life at $\log(T_{\rm eff}/{\rm K}) \sim 5.5$. At lower metallicities ($Z = 0.001, 0.0008$), this happens only for models with $M_{\rm init} > 175$ $M_\odot$.
The fact that the majority of the VMSs experience enhanced winds in the advanced evolutionary phases impacts the expected mass of the He-core, which is the fundamental parameter to understand whether the star enter the pair-instability regime or not (Chapter 3). In Fig. 5.7, the evolution of the He core mass is shown and in Tab. 5.1 the final He core mass values of the same systems are reported. At $Z = 0.008$, after being formed, the mass of He core quickly starts to decrease and all the models end their life with 13.7 $M_\odot \leq M_{\rm He\ core,\ f} \leq 20$ $M_\odot$; these systems cannot enter the pair-instability regime and undergo CCSN. Lowering the metallicity, at $Z = 0.004$, only stars with 150 $M_\odot \leq M_{\rm init} \leq 200$ $M_\odot$ can experience PPISNe, while in all the other cases I found $M_{\rm He\ core,\ f} < 32$ $M_\odot$. Considering $Z = 0.001$, stars can experience different fates: the $M_{\rm init} = 50$ $M_\odot$ model is the only one to undergo CCSN; $M_{\rm init} = 75$, 100 $M_\odot$ models go through PPISN episodes; while models with 125 $M_\odot \leq M_{\rm init} \leq 450$ $M_\odot$ can experience PISNe; the $M_{\rm init} = 475$, 500 $M_\odot$ models, instead, directly collapse onto an IMBH. At even lower metallicity ($Z = 0.0008$), similar fates

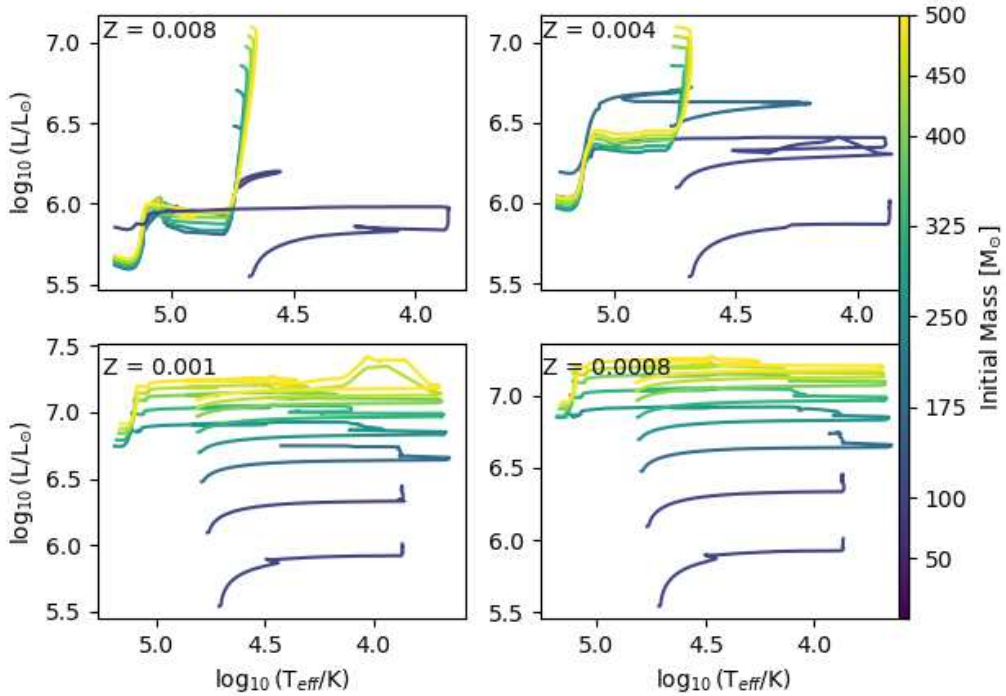

Figure 5.6: HR diagrams of the simulated models divided by metallicity: $Z = 0.008$ models are presented in the top-left panel; $Z = 0.004$ models in the top-right panel; $Z = 0.001$ models in the bottom-left panel; $Z = 0.0008$ models in the bottom-right panel.

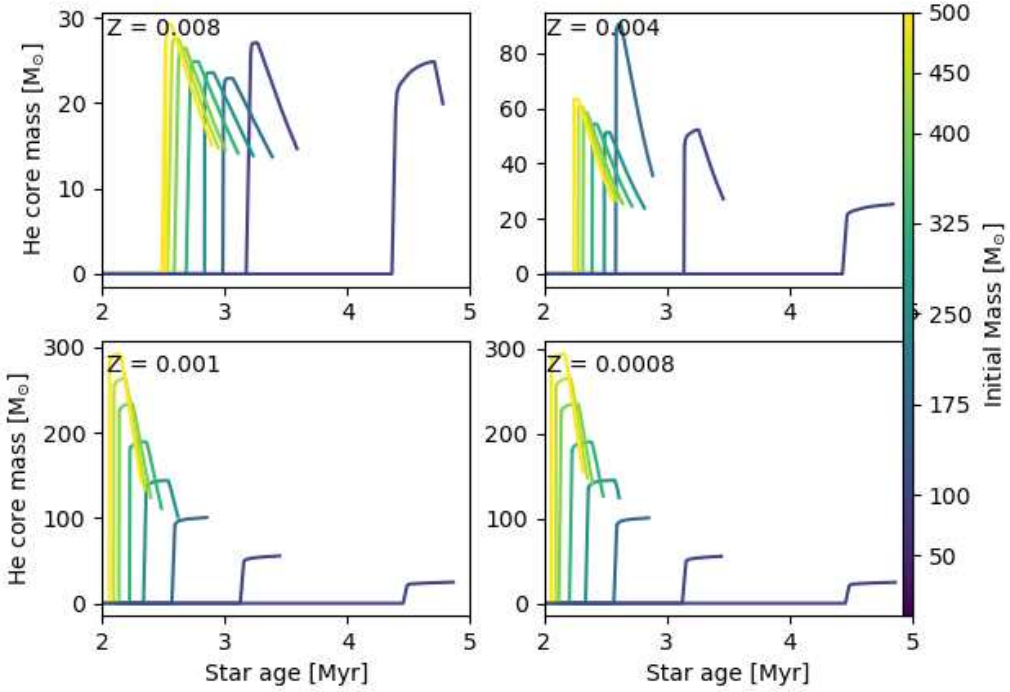

Figure 5.7: He core mass evolution with the time: $Z = 0.008$ models are presented in the top-left panel; $Z = 0.004$ models in the top-right panel; $Z = 0.001$ models in the bottom-left panel; $Z = 0.0008$ models in the bottom-right panel.

	Final He core mass [$M_\odot$]			
$M_{\rm init,\ star}$ [$M_\odot$]	$Z = 0.008$	$Z = 0.004$	$Z = 0.001$	$Z = 0.0008$
50	19.95	25.29	24.73	24.73
75	17.69	32.36	39.92	40.05
100	14.67	27.15	55.47	55.42
125	13.76	28.91	70.58	70.57
150	13.72	32.15	85.56	85.63
175	13.72	35.72	100.44	100.68
200	13.76	39.42	109.67	115.64
225	13.81	23.80	105.42	129.16
250	13.87	23.91	101.07	124.51
275	13.94	24.11	104.55	124.08
300	14.05	24.36	107.28	127.24
325	14.15	24.59	111.27	126.61
350	14.27	24.87	116.09	131.65
375	14.40	25.18	118.67	132.90
400	14.52	25.51	123.79	140.90
425	14.65	25.86	127.66	142.21
450	14.78	26.23	132.21	148.11
475	14.89	26.61	135.75	151.58
500	15.07	27.05	142.14	155.49

Table 5.1: Final mass of the He core of the single stellar model at $Z = 0.008$ (second column), $Z = 0.004$ (third column), $Z = 0.001$ (fourth column) $Z = 0.0008$ (fifth column). In the first column is reported the initial total mass of the corresponding star.

are expected, but the initial stellar mass range of systems that can go through PISNe is reduced: 125 $M_\odot \leq M_{\rm init} \leq$ 350 $M_\odot$; instead, stars with $M_{\rm init} >$ 350 $M_\odot$ directly collapse into IMBHs.
Using the stellar wind model by Sabhahit et al. (2023 [38]), the maximum initial mass of a star that can experience PISN (among the systems I considered) is 450 $M_\odot$ and could lower the expected number of IMBHs. Indeed, this limit was usually set at $\sim$ 250 $M_\odot$ (Spera & Mapelli 2017 [10], Woosley 2017 [14], Marchant et al. 2019 [15], Heger et al. 2023 [9]; Section 2.1.2).

5.3 Binary Systems

In this Section, I present the massive binary models. In all the models, the initial mass of the accretor star is set to 50 $M_\odot$, while the initial masses of the donor stars range from 150 $M_\odot$ to 400 $M_\odot$ by intervals of 50 $M_\odot$. The binary system with initial donor mass equal to 100 $M_\odot$ is presented only for orbital period $P_{\rm orb} = 30$ d and metallicity $Z = 0.004$. None of the models at $Z = 0.001$ reached the end of the simulation, since the mass transfer became unstable and MESA cannot handle it anymore. The same happened with the models at initial mass of the donor star $M_{\rm donor} = 200$ $M_\odot$ and orbital period $P_{\rm orb} = 15$ d, 10 d at metallicity $Z = 0.004$. In all the following plots, the colors represent the initial mass of the donor stars.
In particular, I focused on mass transfer episodes and how they are affected by enhanced winds. In Fig. 5.8 is shown the time evolution of the radius of the donor star (solid line) and its Roche-lobe radius (dashed line). At metallicity $Z = 0.004$, due to the high mass-loss rate, the radii of the more massive stars ($M_{\rm star} >$ 200 $M_\odot$) start to decrease after $\sim$ 1 Myr. As a consequence of that, these stars are not able to fill their Roche volume and cannot transfer mass by RLOF. For the less massive stars at the same metallicity, the orbital period plays an important role. In particular, the binary systems with $P_{\rm orb} = 30$ d and initial donor star mass between 100 $M_\odot$ and 200 $M_\odot$ can experience RLOF episodes for a short phase: the radius of the donor star increases and fills the Roche volumes; then, since the enhanced winds become effective, the radius steeply decreases and the RLOF ends. At shorter periods ($P_{\rm orb} = 15$ d, 10 d), the 150 $M_\odot$ donor star fills its Roche volume constantly until

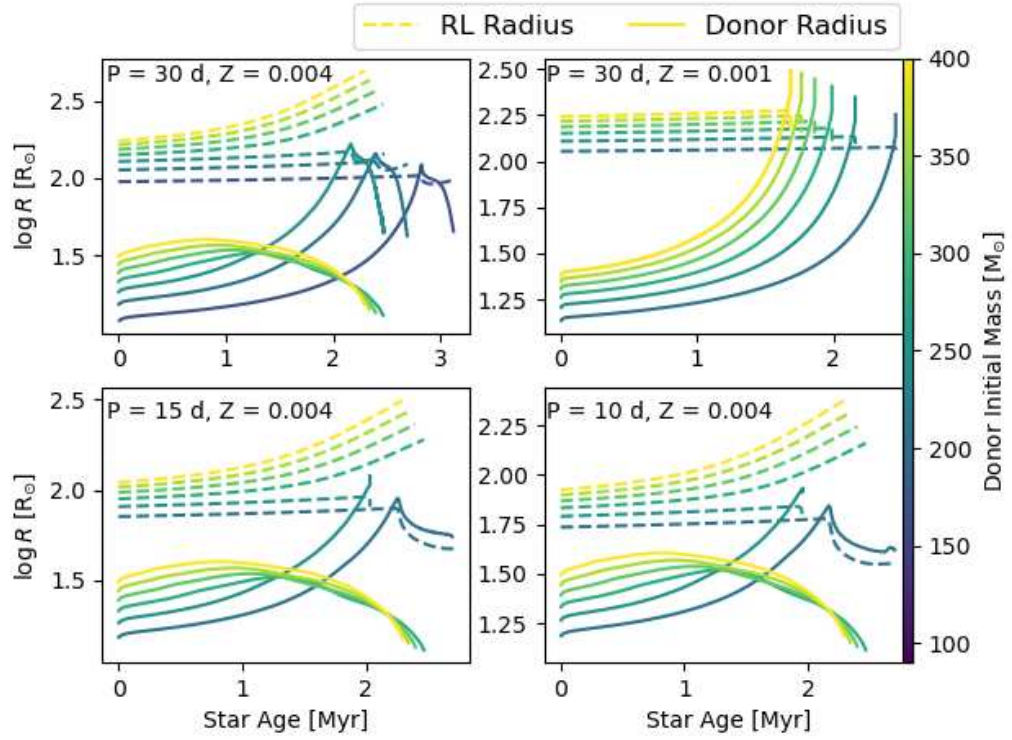

Figure 5.8: Evolution of the donor's radius (solid line) and its Roche-lobe radius (dashed line) as function of the time at different periods and metallicities: $P_{\rm orb} = 30$ d, $Z = 0.004$ binary systems are shown in the top-left panel; $P_{\rm orb} = 30$ d, $Z = 0.001$ in the top-right panel; $P_{\rm orb} = 15$ d, $Z = 0.004$ in the bottom-left panel; $P_{\rm orb} = 10$ d, $Z = 0.004$ in the bottom-right panel.

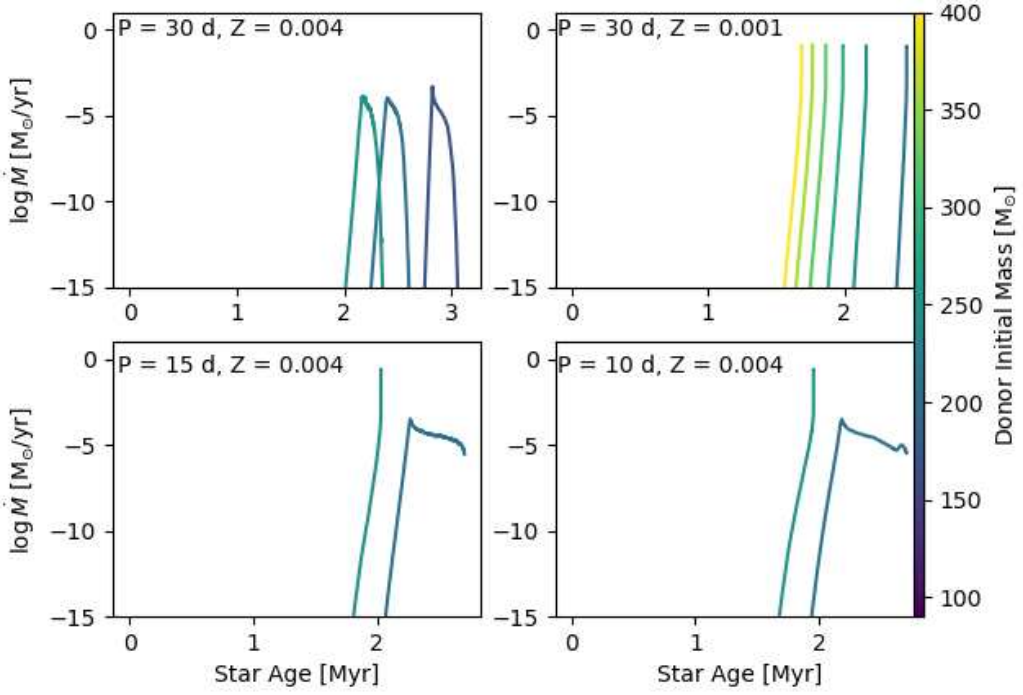

Figure 5.9: Time evolution of the mass transfer rate at different periods and metallicities: $P_{\rm orb} = 30$ d, $Z = 0.004$ binary systems are shown in the top-left panel; $P_{\rm orb} = 30$ d, $Z = 0.001$ in the top-right panel; $P_{\rm orb} = 15$ d, $Z = 0.004$ in the bottom-left panel; $P_{\rm orb} = 10$ d, $Z = 0.004$ in the bottom-right panel.

the end of the MS and the RLOF remains stable. At metallicity $Z = 0.001$, all the binary systems experience RLOF, but it quickly becomes unstable and cannot be modelled by MESA. As shown in Fig. 5.9, these behaviours translates in very different mass transfer rates. In particular, when RLOF is stable and efficient, the mass transfer rate reaches peaks of $\dot{M}_{\rm RLOF} \sim 10^{-3.5}$ M$_\odot$ yr^{-1}.
Fig. 5.10 and Fig. 5.11 show the mass evolution of the donor and accretor stars. The evolution of the most massive stars is dominated by the mass loss due to stellar winds (see also Fig. 5.2). Instead, a wiggle is present during the evolution of the less massive donor stars (100 M$_\odot \leq M_{\rm star} \leq$ 200 M$_\odot$) after $\sim$ 2 Myr, due to the interplay of stellar winds and efficient RLOF. Indeed, in these cases, the mass-loss rate due to stellar winds and the mass transfer rate due to RLOF are comparable and more mass is lost. The mass of the accretor stars, instead, rapidly increases: the accretor star of the binary system at $Z = 0.004$ with initial orbital period $P_{\rm orb} = 10$ d and initial donor mass $M_{\rm donor} = 150$ M$_\odot$ can end its MS with a total mass of $\sim$ 70 M$_\odot$. However, the orbital period is not negligible and it affects the maximum mass that the accretor star can reach: indeed, among all the systems simulated with $P_{\rm orb} = 30$ d and $Z = 0.004$, the maximum mass reached by an accretor star is $M_{\rm accretor} \sim 54$ M$_\odot$ (corresponding to an initial donor star mass $M_{\rm donor} = 200$ M$_\odot$).

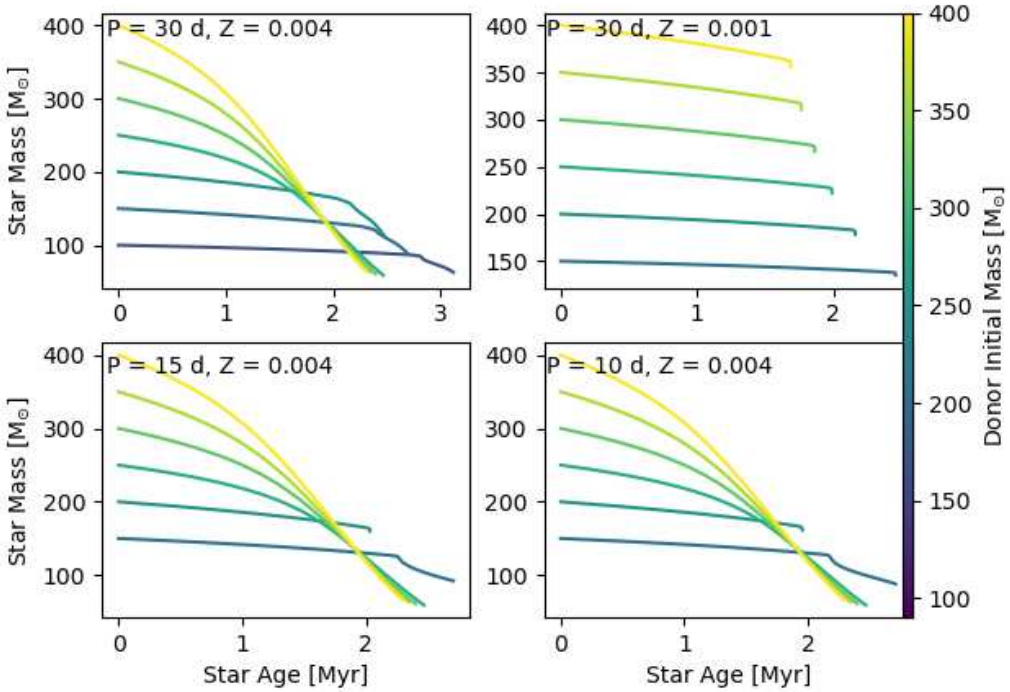

Figure 5.10: Time evolution of the mass of the donor star at different periods and metallicities: $P_{\rm orb} = 30$ d, $Z = 0.004$ binary systems are shown in the top-left panel; $P_{\rm orb} = 30$ d, $Z = 0.001$ in the top-right panel; $P_{\rm orb} = 15$ d, $Z = 0.004$ in the bottom-left panel; $P_{\rm orb} = 10$ d, $Z = 0.004$ in the bottom-right panel.

The time evolution of the orbital periods is shown in Fig. 5.12 and they can vary by more than an order of magnitude when the RLOF is not efficient. Indeed, these stars lose large amount of mass already during the MS and this huge mass loss translates into more and more loosely bound binaries whose components basically evolve as single stars: systems with initial period $P_{\rm orb} = 30$ d can end the MS with periods even longer than 400 d. Instead, when the RLOF is efficient, the periods slightly decrease and remain constant before increasing when the RLOF episode ends.
In conclusion, the stellar wind model used (Sabhahit et al. 2023 [38]) can affect the stellar structure, causing a radius reduction that prevents the more massive stars from filling their Roche volume.

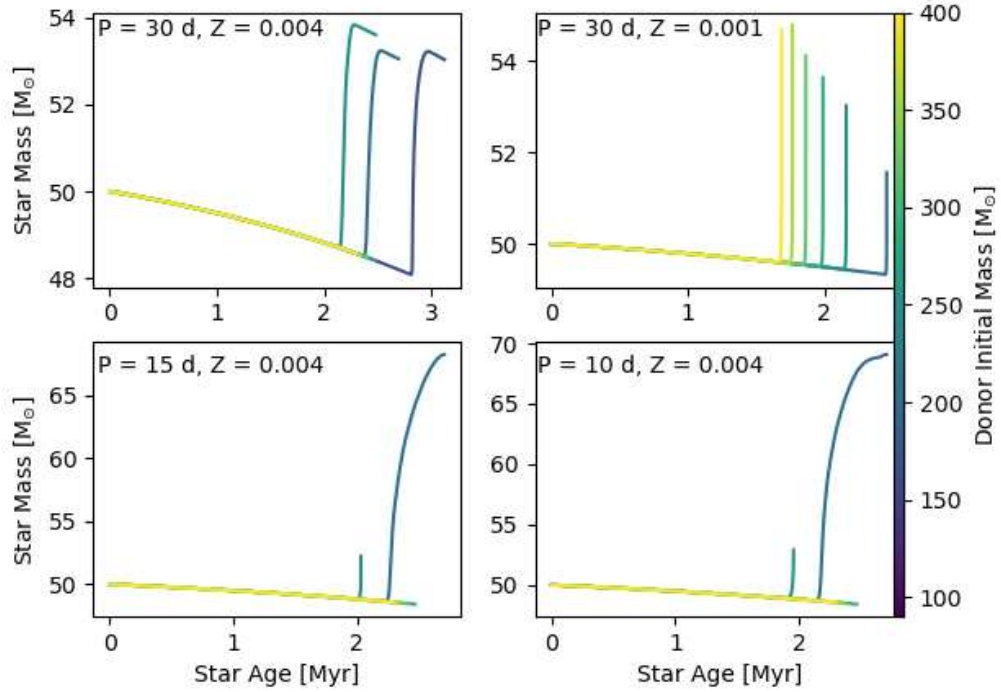

Figure 5.11: Time evolution of the mass of the accretor star at different periods and metallicities: $P_{\rm orb} = 30$ d, $Z = 0.004$ binary systems are shown in the top-left panel; $P_{\rm orb} = 30$ d, $Z = 0.001$ in the top-right panel; $P_{\rm orb} = 15$ d, $Z = 0.004$ in the bottom-left panel; $P_{\rm orb} = 10$ d, $Z = 0.004$ in the bottom-right panel.

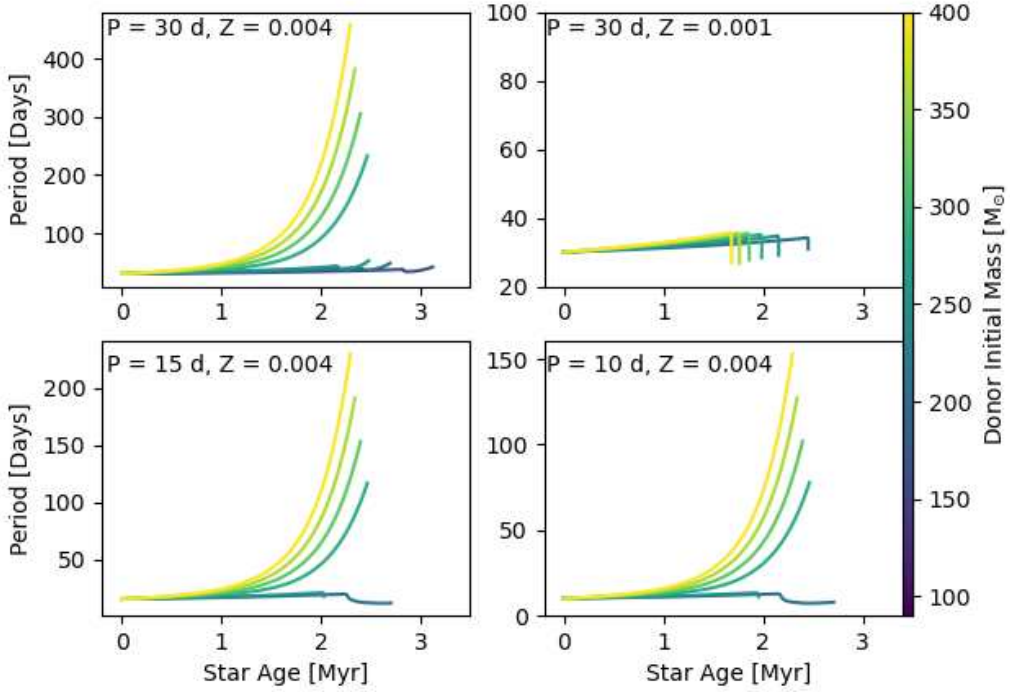

Figure 5.12: Time evolution of orbital period at different periods and metallicities: $P_{\rm orb} = 30$ d, $Z = 0.004$ binary systems are shown in the top-left panel; $P_{\rm orb} = 30$ d, $Z = 0.001$ in the top-right panel; $P_{\rm orb} = 15$ d, $Z = 0.004$ in the bottom-left panel; $P_{\rm orb} = 10$ d, $Z = 0.004$ in the bottom-right panel.

5.4 SEVN & COSMORATE Setups

COSMORATE (Santoliquido et al. 2020 [108], 2021 [109]) is a semi-analytic code that uses data-driven prescription to model the variation of an event rate density as function of the redshift. It is meant to evaluate the merger rate density of compact binaries, but I used it to obtain the PISN and PPISN rate density. Some changes are necessary to achieve this goal. In particular, I modified COSMORATE so that it can handle also empty catalogues. Indeed, as it will be clear in the following (Fig. 5.13), implementing the new winds by Sabhahit et al. (2023 [38]), I do not find any PISN episode above Z = 0.002 and PPISN episode above Z = 0.004 (see also Tab. 5.1 and Fig. 5.7). Then, the most important change I did is to modify how it computes the v matrix, which gives us the number of objects undergoing PISN or PPISN per Mpc^3 as a function of the time bin of PISN explosion, the star formation time bin and the metallicity: when a catalogue is empty, the corresponding value of the v matrix is set to 0, which is equivalent to have efficiency $\eta(Z) = 0$ (Eq. 4.47).
Different prescriptions are present to model the SFRD and metallicity evolution: I chose the fitting formula by Harikane et al. (2022 [96]) reported in Section 4.3.1 to describe the SFRD (Eq. 4.43) and the one by Madau & Fragos (2017 [101]) to describe the metallicity evolution (reported in Section 4.3.2; Eq. 4.45). Then, I used the correction factor $f_{\rm IMF} = 3.59 \times 10^{-4}$ since I simulated only stars with masses between 50 $M_\odot$ and 500 $M_\odot$. This value has been computed simply integrating a Kroupa IMF in the interval of masses I considered. Finally, I incremented the number of bins to 1000 bins to have a more precise esteem.
Each input file contains the total stellar mass simulated and the delay time of each system, as detailed in Section 4.3.3. As delay time, I used the star age at the end of the simulation, which is a good approximation of the total life-time of the star.
The input files, grouped by metallicity, have been produced from the analysis of the SEVN outputs (Spera et al. 2015 [88], Spera & Mapelli 2017 [10], Spera et al. 2019 [89], Iorio et al. 2023 [83]). The initial conditions (ICs) for the SEVN samples have been generated by means of the python module IC4popsyn by Giacobbo et al. (2021 [112]), specifically developed to generate ICs for SEVN. These consist of an input file in which each line contains the initial parameters of a unique system: ZAMS mass, metallicity, stellar spin, supernova model, age of the star at the beginning of the simulation, age at which the simulation stops, times at which the outputs are stored. The initial metallicities I considered are Z = 0.008, 0.006, 0.004, 0.002, 0.001, 0.0008, 0.0006, 0.0004, 0.0002, 0.0001 and the ICs of 10^5 stars have been generated for each metallicity. The initial masses are distributed following a Kroupa IMF with slope $\alpha = 2.3$ between 50 $M_\odot$ and 500 $M_\odot$. Finally, the stellar spin is set to 0 and SN model M20 has been chosen (see Section 4.2.1). Through the analysis of the SEVN outputs, it is possible to generate ICs suitable for COSMORATE.
In order to compare my results with the ones that can be obtained with the stellar wind model by Vink et al. (2001 [4]), I performed the same analysis by using the SEVN tables produced with the stellar evolution code PARSEC (Bressan et al. 2012 [63], Costa et al. 2019a [113], Costa et al. 2019b [114], Nguyen et al. 2022 [115]).

5.5 Pair-instability Supernova Rate Density

In this Section, I present the results obtained from the analysis of the SEVN and COSMORATE outputs. I show the rate of systems undergoing PISNe and PPISNe among the mass range I considered ($50\ M_\odot \leq M_{\rm star} \leq 500\ M_\odot$). Then, the PISN and PPISN rate density evolution with the redshift, the main results of this work, are presented and discussed.
First of all, thanks to the analysis of the SEVN results, it is possible to obtain the rate of systems undergoing PISN or PPISN among the ones I simulated (Fig. 5.13). Even if the numerical value is biased by the range of masses I considered ($50\ M_\odot < M_{\rm simulated} < 500\ M_\odot$), it is interesting to comment the general evolution with the metallicity. Indeed, the PISN rate computed using the new stellar wind model by Sabhahit et al. (2023 [38]), reported in the bottom panel of Fig. 5.13, is constant until metallicity $Z \sim 6 \times 10^{-4}$, where the mass-loss rate is enhanced only in the last evolutionary phases. Then, the peak is reached at $Z = 10^{-3}$. Beyond the peak, the rate quickly decreases and above

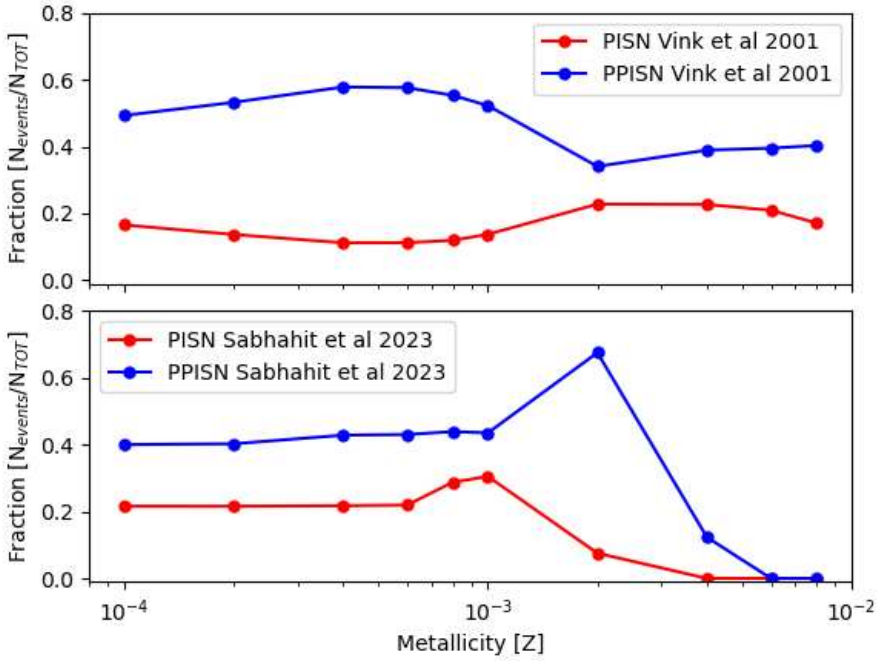

Figure 5.13: Fractions of PISNe (red) and PPISNe (blue), computed as number of system undergoing PISNe and PPISNe over the total number of system simulated, as function of the metallicity. The top panel shows the fractions obtained with the model by Vink et al. (2001 [4]) and the bottom panel shows the fractions obtained with the model by Sabhahit et al. (2023 [38]).

$Z = 2 \times 10^{-2}$ no PISN episodes are present. The PPISN rate shows the same behaviour, reaching the peak at $Z = 2 \times 10^{-2}$ and going to zero above $Z = 4 \times 10^{-2}$. One can expect that the rates monotonically decrease increasing the metallicity, since an higher metallicity translates into a less massive star and a less massive core. The peaks are a consequence of the enhanced mass-loss rate: indeed, even the more massive stars, which should undergo direct collapse onto a BH at the end of their life, can now enter the pair instability regime (see Tab. 5.1 and Fig. 5.7). Instead, at metallicity $Z > 2 \times 10^{-3}$ ($Z > 4 \times 10^{-3}$), the winds are so strong that the stars are prevented from undergoing PISN (PPISN) episodes and experience CCSN.

The top panel of Fig. 5.13 shows the rates computed using the stellar evolution code PARSEC and implementing the stellar wind model by Vink et al. (2001 [4]). A kink is present at $Z = 2 \times 10^{-3}$, above which the PPISN rate is slightly reduced and the PISN rate slightly increased. This behaviour can be due to the fact that the mass-loss rate increases with the metallicity: indeed, a higher mass-loss rate can make the more massive stars to enter the pair-instability regime (undergoing PISNe) and the less massive stars to avoid it.

Fig. 5.14 and Fig. 5.15 show the new PISN and PPISN rate density evolution across cosmic time obtained with COSMORATE, respectively: the thick black line represents the total evolution of the rate density and the colored thin lines the contribution by the single metallicities. In both the cases, the rate density increases from redshift $z = 15$ to redshift $z = 8$; then, a sort of plateau is present between redshift $z = 4$ and $z = 8$; finally, it steeply decreases from redshift $z = 2$ to redshift $z = 0$. As expected, different metallicities contribute in different epochs: at high redshift, the main contribution are from $Z = 1 \times 10^{-4}$ and $Z = 2 \times 10^{-4}$; at low redshift, instead, the main contributions are from $Z = 2 \times 10^{-3}$ and, in the case of PPISNe, $Z = 4 \times 10^{-3}$.

The steep drop at very low redshift is due to fact that no contributions from metallicities above $Z = 4 \times 10^{-3}$ are present; this is the reason why it was important to modify COSMORATE and make it able to read empty catalogues as explained in the previous Section. Indeed, between solar metallicity ($Z = 0.019$) and $Z = 4 \times 10^{-3}$, due to the large amount of mass loss, the final He core mass is lower than the threshold set to enter the pair-instability regime and even the more massive

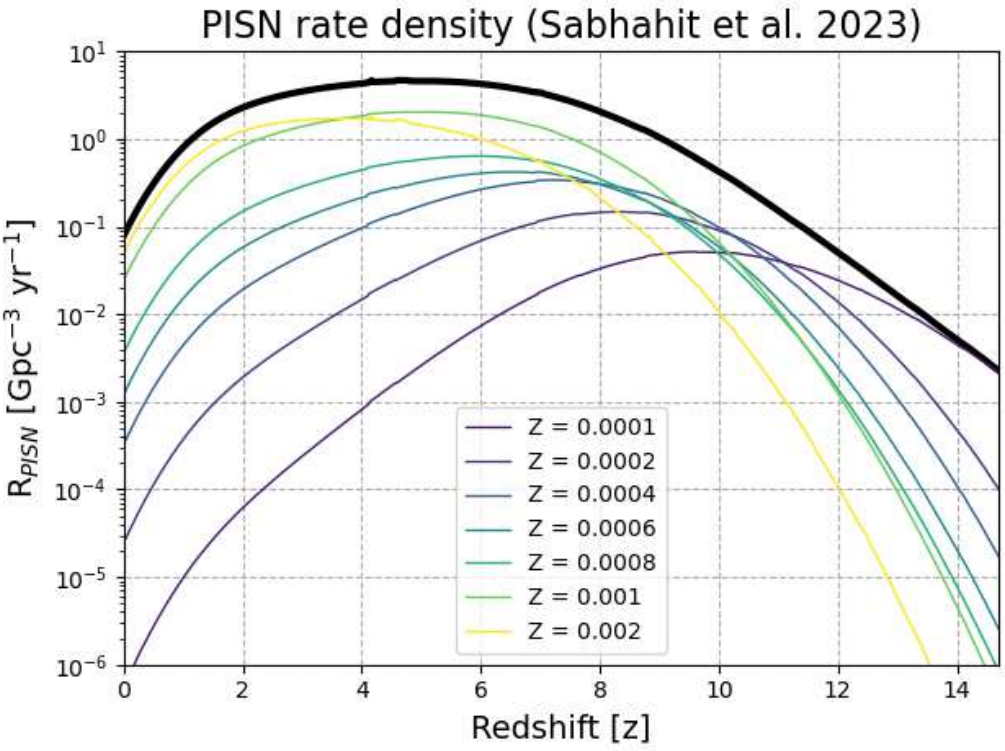

Figure 5.14: PISN rate density evolution with redshift from simulation with the new wind model by Sabhahit et al. (2023 [38]). The black thick line represents the total rate density, the colored ones contribution of the single metallicities.

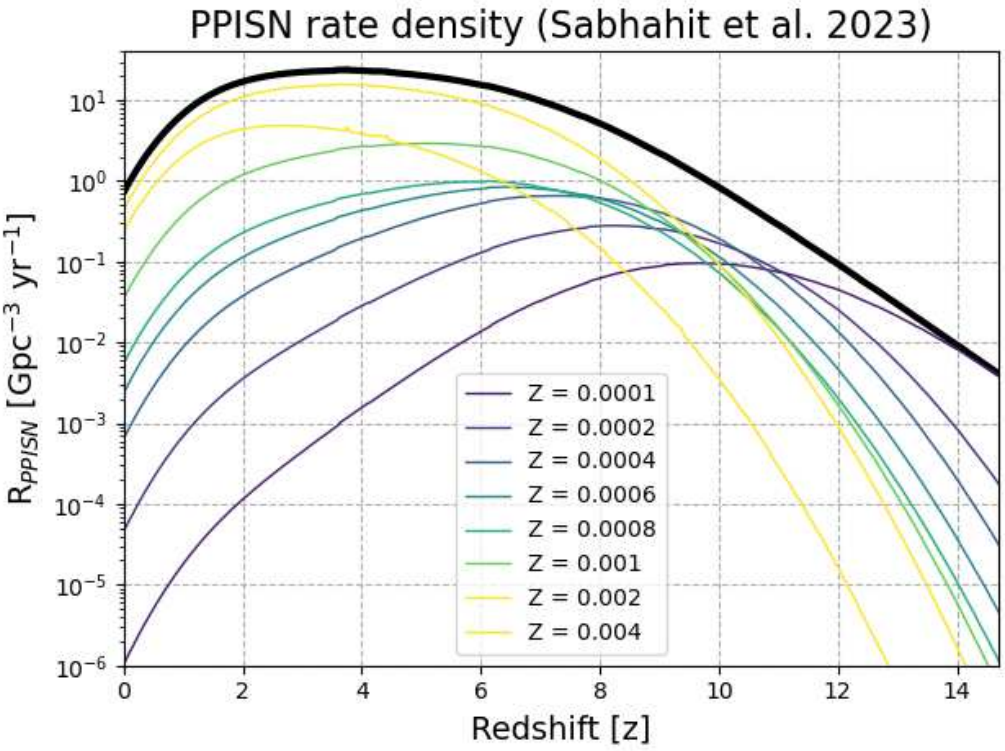

Figure 5.15: PPISN rate density evolution with redshift from simulation with the new wind model by Sabhahit et al. (2023 [38]). The black thick line represents the total rate density, the colored ones contribution of the single metallicities.

stars undergo CCSN.
The predicted PISN and PPISN rate density at redshift $z = 0$ are the following:

$$R_{\rm PISN} = 8.08 \times 10^{-2}\ {\rm Gpc}^{-3}\ {\rm yr}^{-1}\,, \tag{5.2}$$

$$R_{\rm PPISN} = 7.39 \times 10^{-1}\ {\rm Gpc}^{-3}\ {\rm yr}^{-1}\,. \tag{5.3}$$

The same analysis has been performed using the SEVN tables produced with the stellar evolution code PARSEC and the wind model by Vink et al. (2001 [4]) implemented: in Fig. 5.16 and Fig. 5.17, the total PISN and PPISN rate density evolution (black thick line) and the contribution by each metallicity (colored thin lines) are shown. In this case, also VMSs at metallicities until $Z = 0.008$ are expected to undergo PISNe and PPISNe. This fact translates into a peak in the PISN and PPISN rate density between redshift $z = 1$ and $z = 2$ and higher values at redshift $z = 0$: $R_{\rm PISN,\ z\,=\,0} = 5.94\ {\rm Gpc}^{-3}\ {\rm yr}^{-1}$; $R_{\rm PPISN,\ z\,=\,0} = 13.35\ {\rm Gpc}^{-3}\ {\rm yr}^{-1}$.

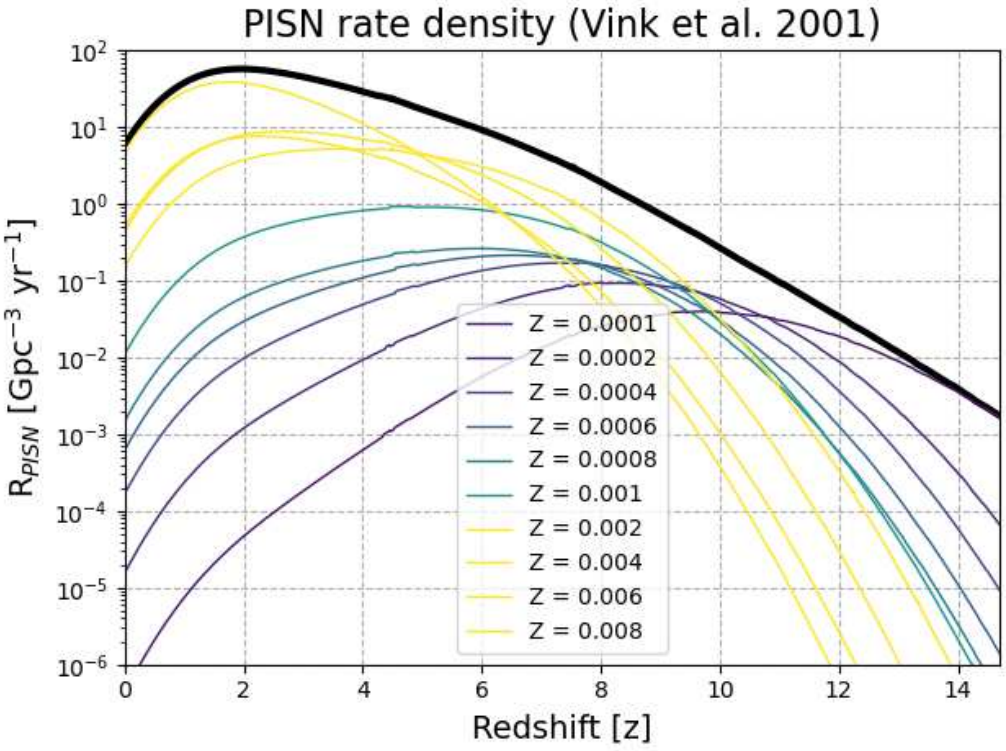

Figure 5.16: PISN rate density evolution with redshift from simulation with the wind model by Vink et al. (2001 [4]). The black thick line represents the total rate density, the colored ones contribution of the single metallicities.

A direct comparison between the results given by the wind model by Vink et al. (2001 [4]; dashed lines) and the one by Sabhahit et al. (2023 [38]; solid lines) is shown in Fig. 5.18, where the red (blue) line represents the PISN (PPISN) rate densities; while, in Fig. 5.19, it is the reported the ratio of the two rate densities, where $R_{\rm old}$ stands for the ones obtained using the model by Vink et al. (2001 [4]) and $R_{\rm new}$ stands for ones obtained using the model by Sabhahit et al. (2023 [38]). One can expect exactly the same behaviour at high redshift, where the main contributions are from low metallicities and the enhanced winds are not effective. However, the SEVN tables have been produced by means of two different stellar evolution codes, MESA and PARSEC, which treat the evolution of the core in different ways. This is the reason why some small discrepancies are however present at high redshift.
In conclusion, I want to highlight how the enhanced winds (Sabhahit et al. 2023 [38]) can prevent PISN (PPISN) episodes, lowering the metallicity threshold above which these events can occur from $Z \sim Z_{\odot}/3$ to $Z \sim 2 \times 10^{-3}$ ($Z \sim 4 \times 10^{-3}$). The absence of contributions by higher metallicities suppresses the peak between redshift $z = 1$ and $z = 2$ and reduces the rate densities at redshift $z = 0$ by two order of magnitude with respect to the one predicted with the old model (Vink et al.

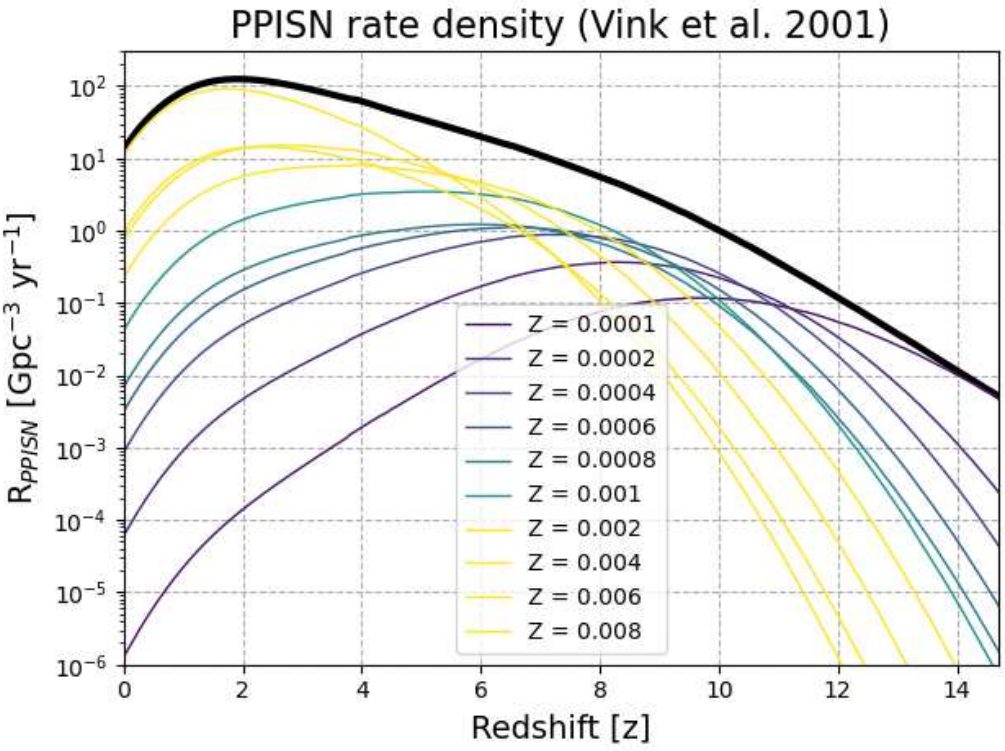

Figure 5.17: PPISN rate density evolution with redshift from simulation with the wind model by Vink et al. (2001 [4]). The black thick line represents the total rate density, the colored ones contribution of the single metallicities.

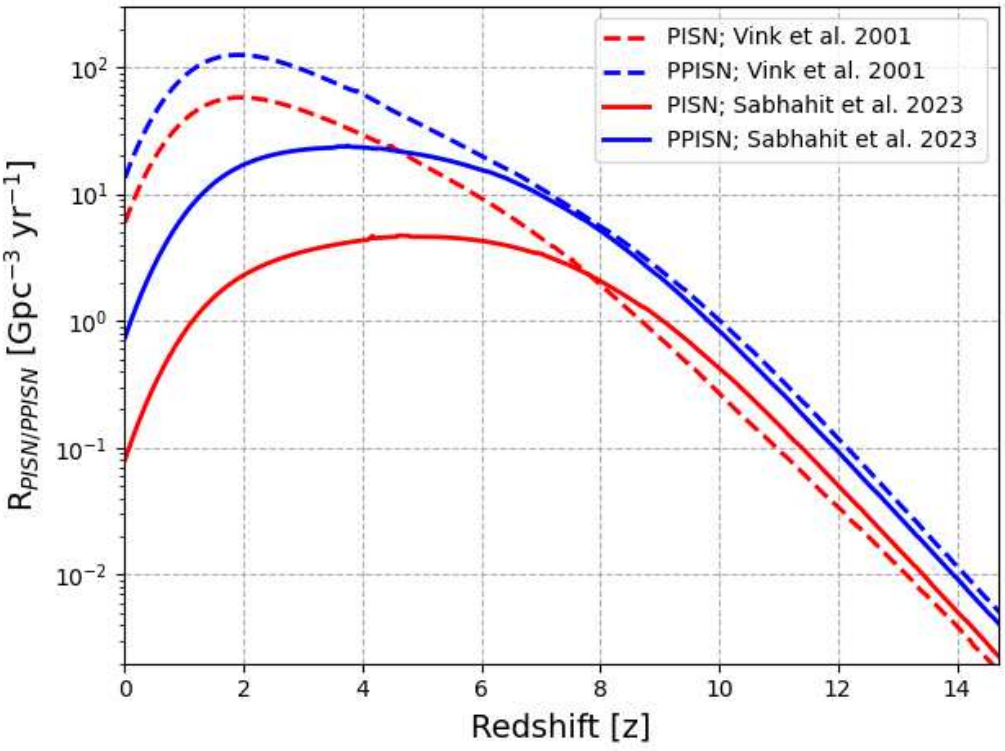

Figure 5.18: Comparison between the total PISN (solid red line) and PPISN (solid blue line) rate densities obtained using the model by Sabhahit et al. (2023 [38]) and the PISN (dashed red line) and PPISN (dashed blue line) rate densities obtained using the model by Vink et al. (2001 [4]).

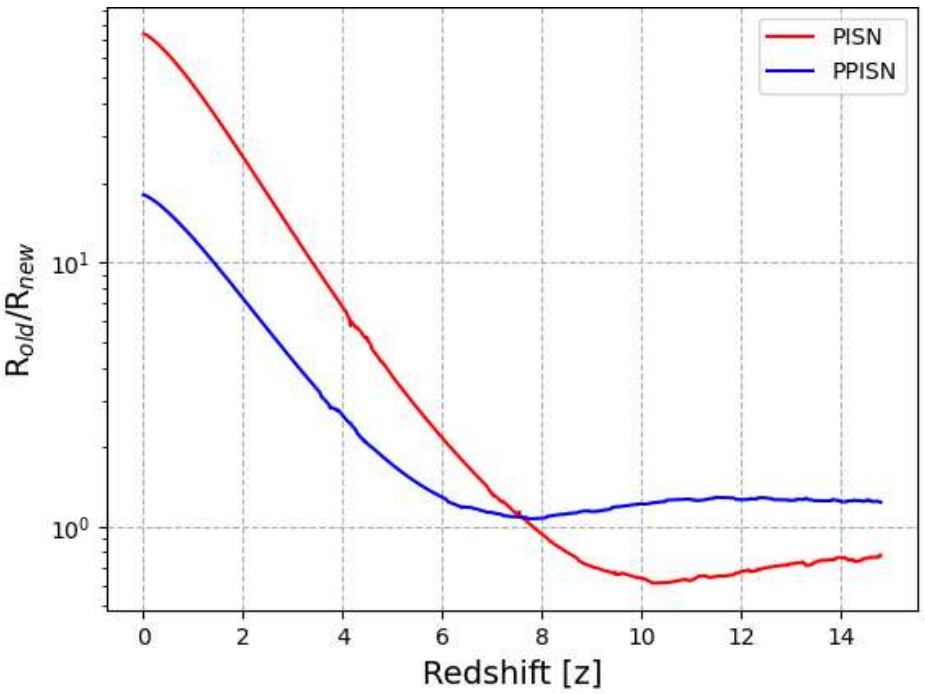

Figure 5.19: Ratio between PISN (red) and PPISN (blue) rate density computed with the stellar wind model by Vink et al. (2001 [4]) $R_{\rm old}$ and by Sabhahit et al. (2023 [38]) $R_{\rm new}$.

2001 [4]). Remarkably, the updated PISN rate density that I have obtained performing this analysis falls inside the observational rate density constraints obtained by Schulze et al. (2024 [56]) through the photometric and spectroscopic analysis of SN 2018ibb (Section 3.2).

Chapter 6

Conclusion

In this work, I studied the evolution of VMSs implementing the new model for the stellar winds by Sabhahit et al. (2022 [32], 2023 [38]) in order to obtain updated PISN and PPISN rate density. This new model characterizes the transition from an optically-thin to an optically-thick wind in VMSs and results in a higher mass-loss rate with respect to the one predicted in previous works, e.g. Vink et al. (2001 [4]), which is the most commonly used.
By means of the stellar evolution code MESA (Paxton et al. 2011 [33], 2013 [34], 2015 [35], 2018 [36], 2019 [37]), I modelled single VMSs with initial masses from 50 $M_\odot$ to 500 $M_\odot$ by intervals of 25 $M_\odot$ and initial metallicities $Z = 0.008$, 0.006, 0.004, 0.002, 0.001, 0.0008, 0.0006, 0.0004, 0.0002, 0.0001. At higher metallicities ($Z = 0.008$, 0.006), all the simulated models go through enhanced winds, while the initial stellar mass required to enter this regime increases lowering the metallicity. The stars, which experience optically-thick winds just after the ZAMS, have a vertical evolution in the HR diagram: the luminosity steeply drops, but a very narrow range of temperatures is spanned. Instead, at lower metallicities, where the winds are less efficient, the stars show a completely different behaviour in the HR diagram, moving toward the red with a basically constant luminosity. The stellar structure is also affected: indeed, due to the large amount of mass lost, the stellar radius starts to decrease when the winds are enhanced.
I also modelled binary systems, varying the orbital period ($P_{\rm orb}$ = 30, 15, and 10 d), in order to follow mass transfer episodes. The initial mass of the accretor star is always fixed to 50 $M_\odot$, while the initial mass of the donor rages from 150 $M_\odot$ to 400 $M_\odot$ by intervals of 50 $M_\odot$. Two different metallicities have been considered: $Z = 0.004$, 0.001. Since radii of the more massive stars decrease when they enter the optically-thick regime, all the binaries at metallicity $Z = 0.004$ and initial donor mass $M_{\rm donor} \geq 200$ $M_\odot$ cannot undergo RLOF. Instead, at short orbital periods ($P_{\rm orb} = 15, 10$ d), the systems with $M_{\rm donor} < 200$ $M_\odot$ can experience stable RLOF until the end of the MS. At $Z = 0.001$, stellar winds are less efficient and stellar radii inflate; as a consequence, all the binary systems go through RLOF episodes.
The stellar tracks obtained with MESA have been used to produce stellar tables for the population synthesis code SEVN (Spera et al. 2015 [88], Spera & Mapelli 2017 [10], Spera et al. 2019 [89], Iorio et al. 2023 [83]). By means of SEVN, the evolution of 10^5 stars for each metallicity ($Z = 0.008$, 0.006, 0.004, 0.002, 0.001, 0.0008, 0.0006, 0.0004, 0.0002, 0.0001) have been followed until the formation of the CO core. The initial masses have been generated following a Kroupa IMF between 50 $M_\odot$ and 500 $M_\odot$. The enhanced mass-loss rate translates into a large amount of mass lost already in the MS, preventing the models at metallicities higher than $Z = 0.004$ from undergoing PPISNe and the ones at metallicities higher than $Z = 0.002$ from undergoing PISNe. Another important consequence is that, at $Z = 0.001$, also stars with initial masses until $M_{\rm star} = 450$ $M_\odot$ can experience PISNe instead of directly collapsing in an IMBH. Lowering the metallicity, the maximum mass of a star undergoing PISN decreases: e.g. at $Z = 0.0008$, this value is set to 375 $M_\odot$.
Then, I combined the outputs of SEVN with a semi-analytic code, COSMORATE (Santoliquido et al. 2020 [108], 2021 [109]), which uses data-driven prescriptions to model the SFRD and metallicity evolution. In particular, I used the fitting formulas by Harikane et al. (2022 [96]) to model the

SFRD and the one by Madau & Fragos (2017 [101]) to model the metallicity evolution. Thanks to the analysis of the COSMORATE outputs, I obtained the main results of this work: the evolution of PISN and PPISN rate density across the cosmic time, taking the new stellar wind model by Sabhahit et al. (2022 [32], 2023 [38]) into account. In both cases, the rate density increases from redshift $z = 15$ to redshift $z = 8$; then, a plateau is present between redshift $z = 4$ and $z = 8$; finally, it steeply decreases from redshift $z = 2$ to redshift $z = 0$. As expected, different metallicities contribute in different epochs: at high redshift, the main contributions are from $Z = 0.0001$ and $Z = 0.0002$; at low redshift, instead, the main contributions are from $Z = 0.002$ and, in the case of PPISNe, also $Z = 0.004$. The absence of contributions from metallicities above $Z = 0.002$ and $Z = 0.004$ causes the drop at very low redshift. The predicted PISN and PPISN rate density at redshift $z = 0$ are then:

$$R_{\rm PISN} = 8.08 \times 10^{-2}\ {\rm Gpc}^{-3}\ {\rm yr}^{-1}\,, \tag{6.1}$$

$$R_{\rm PPISN} = 7.39 \times 10^{-1}\ {\rm Gpc}^{-3}\ {\rm yr}^{-1}\,. \tag{6.2}$$

To compare my results with the old stellar wind model by Vink et al. (2001 [4]), I performed the same analysis using SEVN tables produced with the stellar evolution code PARSEC (Bressan et al. 2012 [63], Costa et al. 2019a [113], Costa et al. 2019b [114], Nguyen et al. 2022 [115]). In this case, the main contributions on the PISN and PPISN rate densities at low redshift are from metallicities $Z = 0.008, 0.006$. This translates into a peak between redshift $z = 1$ and $z = 2$, which is instead suppressed using the model by Sabhahit et al. (2022 [32], 2023 [38]).
In conclusion, the enhanced wind model lowers the metallicity threshold above which PISNe (PPISNe) cannot occur from $Z = 0.008$ to $Z = 0.002$ ($Z = 0.004$). As a consequence, the PISN and PPISN rate density at redshift $z = 0$ are two orders of magnitude lower than the ones obtained using the model by Vink et al. (2001 [4]).
Previous models of stellar winds resulted in an excess of the PISN rate, in tension with the upper limits from data. The new rate density I obtain adopting the winds by Sabhahit et al (2023 [38]) is instead in agreement with the observational constraints imposed by Schulze et al. (2024 [56]) through the photometric and spectroscopic analysis of SN 2018ibb: $0.009\ {\rm Gpc}^{-3}\ {\rm yr}^{-1} \leq R_{\rm PISN} \leq 0.7\ {\rm Gpc}^{-3}\ {\rm yr}^{-1}$. This demonstrates the importance of stellar winds to describe the evolution of massive and very massive stars and their final fates: (pulsational) pair instability and compact-object formation.

Bibliography

[1] Krumholz M. R., 2015, ASSL, 412, 43. doi:10.1007/978-3-319-09596-7_3

[2] Abel T., Bryan G. L., Norman M. L., 2000, ApJ, 540, 39. doi:10.1086/309295

[3] Bromm V., Yoshida N., Hernquist L., McKee C. F., 2009, Nature, 459, 49. doi:10.1038/nature07990

[4] Vink J. S., de Koter A., Lamers H. J. G. L. M., 2001, A&A, 369, 574. doi:10.1051/0004-6361:20010127

[5] de Jager C., Nieuwenhuijzen H., van der Hucht K. A., 1988, A&AS, 72, 259

[6] Bennett M. E., Hirschi R., Pignatari M., Diehl S., Fryer C., Herwig F., Hungerford A., et al., 2012, MNRAS, 420, 3047. doi:10.1111/j.1365-2966.2012.20193.x

[7] Hirschi R., 2017, hsn..book, 567. doi:10.1007/978-3-319-21846-5_120

[8] Vink J. S., Muijres L. E., Anthonisse B., de Koter A., Gräfener G., Langer N., 2011, A&A, 531, A132. doi:10.1051/0004-6361/201116614

[9] Heger A., Müller B., Mandel I. 2023, arXiv, arXiv:2304.09350. doi:10.48550/arXiv.2304.09350

[10] Spera M., Mapelli M., 2017, MNRAS, 470, 4739. doi:10.1093/mnras/stx1576

[11] Yoshida T., Umeda H., 2011, MNRAS, 412, L78. doi:10.1111/j.1745-3933.2011.01008.x

[12] Yusof N., Hirschi R., Meynet G., Crowther P. A., Ekström S., Frischknecht U., Georgy C., et al., 2013, MNRAS, 433, 1114. doi:10.1093/mnras/stt794

[13] Di Carlo U. N., Mapelli M., Pasquato M., Rastello S., Ballone A., Dall'Amico M., Giacobbo N., et al., 2021, MNRAS, 507, 5132. doi:10.1093/mnras/stab239

[14] Woosley S. E., 2017, ApJ, 836, 244. doi:10.3847/1538-4357/836/2/244

[15] Marchant P., Renzo M., Farmer R., Pappas K. M. W., Taam R. E., de Mink S. E., Kalogera V., 2019, ApJ, 882, 36. doi:10.3847/1538-4357/ab3426

[16] Crowther P. A., Schnurr O., Hirschi R., Yusof N., Parker R. J., Goodwin S. P., Kassim H. A., 2010, MNRAS, 408, 731. doi:10.1111/j.1365-2966.2010.17167.x

[17] Martins F., Palacios A., 2022, A&A, 659, A163. doi:10.1051/0004-6361/202243048

[18] Kozyreva A., Ph.D. dissertation, University of Bonn, 2014.

[19] Martins F., Hillier D. J., Paumard T., Eisenhauer F., Ott T., Genzel R., 2008, A&A, 478, 219. doi:10.1051/0004-6361:20078469

[20] Bestenlehner J. M., Gräfener G., Vink J. S., Najarro F., de Koter A., Sana H., Evans C. J., et al., 2014, A&A, 570, A38. doi:10.1051/0004-6361/201423643

[21] Lamers H. J. G. L. M., Cassinelli J. P., Line driven winds. In: Introduction to Stellar Winds. Cambridge University Press; 1999:187-254.

[22] Castor J. I., Abbott D. C., Klein R. I., 1975, ApJ, 195, 157. doi:10.1086/153315

[23] Curé M., Araya I., 2023, Galax, 11, 68. doi:10.3390/galaxies11030068

[24] Müller P. E., Vink J. S., 2008, A&A, 492, 493. doi:10.1051/0004-6361:20078798

[25] Nugis T., Lamers H. J. G. L. M., 2002, A&A, 389, 162. doi:10.1051/0004-6361:20020557

[26] Sander A. A. C., Vink J. S., Hamann W. R., 2020, MNRAS, 491, 4406. doi:10.1093/mnras/stz3064

[27] Vink J. S., 2024, arXiv, arXiv:2406.16517. doi:10.48550/arXiv.2406.16517

[28] Vink J. S., Gräfener G., 2012, ApJL, 751, L34. doi:10.1088/2041-8205/751/2/L34

[29] Gräfener G., Koesterke L., Hamann W. R., 2002, A&A, 387, 244. doi:10.1051/0004-6361:20020269

[30] Hamann W. R., Gräfener G., 2003, A&A, 410, 993. doi:10.1051/0004-6361:20031308

[31] Sander A., Shenar T., Hainich R., Gímenez-García A., Todt H., Hamann W.-R., 2015, A&A, 577, A13. doi:10.1051/0004-6361/201425356

[32] Sabhahit G. N., Vink J. S., Higgins E. R., Sander A. A. C., 2022, MNRAS, 514, 3736. doi:10.1093/mnras/stac1410

[33] Paxton B., Bildsten L., Dotter A., Herwig F., Lesaffre P., Timmes F., 2011, ApJS, 192, 3. doi:10.1088/0067-0049/192/1/3

[34] Paxton B., Cantiello M., Arras P., Bildsten L., Brown E. F., Dotter A., Mankovich C., et al., 2013, ApJS, 208, 4. doi:10.1088/0067-0049/208/1/4

[35] Paxton B., Marchant P., Schwab J., Bauer E. B., Bildsten L., Cantiello M., Dessart L., et al., 2015, ApJS, 220, 15. doi:10.1088/0067-0049/220/1/15

[36] Paxton B., Schwab J., Bauer E. B., Bildsten L., Blinnikov S., Duffell P., Farmer R., et al., 2018, ApJS, 234, 34. doi:10.3847/1538-4365/aaa5a8

[37] Paxton B., Smolec R., Schwab J., Gautschy A., Bildsten L., Cantiello M., Dotter A., et al., 2019, ApJS, 243, 10. doi:10.3847/1538-4365/ab2241

[38] Sabhahit G. N., Vink J. S., Sander A. A. C., Higgins E. R., 2023, MNRAS, 524, 1529. doi:10.1093/mnras/stad1888

[39] Gräfener G., Vink J. S., de Koter A., Langer N., 2011, A&A, 535, A56. doi:10.1051/0004-6361/201116701

[40] Vink J. S., Sander A. A. C., 2021, MNRAS, 504, 2051. doi:10.1093/mnras/stab902

[41] Sana H., de Mink S. E., de Koter A., Langer N., Evans C. J., Gieles M., Gosset E., et al., 2012, Sci, 337, 444. doi:10.1126/science.1223344

[42] Bondi H., Hoyle F., 1944, MNRAS, 104, 273. doi:10.1093/mnras/104.5.273

[43] Hurley J. R., Tout C. A., Pols O. R., 2002, MNRAS, 329, 897. doi:10.1046/j.1365-8711.2002.05038.x

[44] Lauer A. C., 2017, PhDT

[45] Eggleton P. P., 1983, ApJ, 268, 368. doi:10.1086/160960

[46] Mapelli M., 2021, hgwa.book, 16. doi:10.1007/978-981-15-4702-7_16-1

[47] Webbink R. F., 1984, ApJ, 277, 355. doi:10.1086/161701

[48] Marchant P., Langer N., Podsiadlowski P., Tauris T. M., Moriya T. J., 2016, A&A, 588, A50. doi:10.1051/0004-6361/201628133

[49] Barkat Z., Rakavy G., Sack N., 1967, PhRvL, 18, 379. doi:10.1103/PhysRevLett.18.379

[50] Fowler W. A., Hoyle F., 1964, ApJS, 9, 201. doi:10.1086/190103

[51] Heger A., Woosley S. E., 2002, ApJ, 567, 532. doi:10.1086/338487

[52] Stothers R. B., 1999, MNRAS, 305, 365. doi:10.1046/j.1365-8711.1999.02444.x

[53] Farmer R., Renzo M., de Mink S. E., Marchant P., Justham S., 2019, ApJ, 887, 53. doi:10.3847/1538-4357/ab518b

[54] Costa G., Bressan A., Mapelli M., Marigo P., Iorio G., Spera M., 2021, MNRAS, 501, 4514. doi:10.1093/mnras/staa3916

[55] Arca sedda M., Kamlah A. W. H., Spurzem R., Rizzuto F. P., Giersz M., Naab T., Berczik P., 2024, MNRAS, 528, 5140. doi:10.1093/mnras/stad3951

[56] Schulze S., Fransson C., Kozyreva A., Chen T. W., Yaron O., Jerkstrand A., Gal-Yam A., et al., 2024, A&A, 683, A223. doi:10.1051/0004-6361/202346855

[57] Kozyreva, A., Kromer, M., Noebauer, U. M., & Hirschi, R. 2018, MNRAS, 479, 3106

[58] Jerkstrand A., Smartt S. J., Heger A., 2016, MNRAS, 455, 3207. doi:10.1093/mnras/stv2369

[59] Briel, M. M., Eldridge, J. J., Stanway, E. R., Stevance, H. F., & Chrimes, A. A. 2022, MNRAS, 514, 1315

[60] Xing, Q. F., Zhao, G., Liu, Z. W., et al. 2023, Nature, 618, 712, doi: 10.1038/s41586-023-06028-1

[61] Skúladóttir Á., Koutsouridou I., Vanni I., Amarsi A. M., Lucchesi R., Salvadori S., Aguado D. S., 2024, ApJL, 968, L23. doi:10.3847/2041-8213/ad4b1a

[62] Eggleton P. P., 1971, MNRAS, 151, 351. doi:10.1093/mnras/151.3.351

[63] Bressan A., Marigo P., Girardi L., Salasnich B., Dal Cero C., Rubele S., Nanni A., 2012, MNRAS, 427, 127. doi:10.1111/j.1365-2966.2012.21948.x

[64] Degl'Innocenti S., Prada Moroni P. G., Marconi M., Ruoppo A., 2008, Ap&SS, 316, 25. doi:10.1007/s10509-007-9560-2

[65] Szécsi D., Agrawal P., Wünsch R., Langer N., 2022, A&A, 658, A125. doi:10.1051/0004-6361/202141536

[66] Eggenberger P., Meynet G., Maeder A., Hirschi R., Charbonnel C., Talon S., Ekström S., 2008, Ap&SS, 316, 43. doi:10.1007/s10509-007-9511-y

[67] Rogers, F. J., & Nayfonov, A., 2002, ApJ, 576, 1064

[68] Saumon, D., Chabrier, G., & van Horn, H. M. 1995, ApJS, 99, 713

[69] Timmes, F. X., & Swesty, F. D. 2000, ApJS, 126, 501

[70] Potekhin, A. Y., & Chabrier, G. 2010, Contrib. Plasma Phys., 50, 82

[71] Timmes, F. X. 1999, ApJS, 124, 241

[72] Grevesse, N. & Noels, A., 1993, Phys. Scr. T, 47, 133

[73] Castelli, F., & Kurucz, R. L. 2003, IAU Symp. 210, ed. N. Piskunov, W. W. Weiss, & D. F. Gray San Francisco: ASP

[74] Ledoux P., 1947, ApJ, 105, 305. doi:10.1086/144905

[75] Schwarzschild M., 1958, ses..book

[76] Cox J. P., Giuli R. T., 1968, pss..book

[77] Joyce M., Tayar J., 2023, Galax, 11, 75. doi:10.3390/galaxies11030075

[78] Pasetto S., Chiosi C., Chiosi E., Cropper M., Weiss A., 2016, MNRAS, 459, 3182. doi:10.1093/mnras/stw858

[79] Yoon, S. C., & Langer, N. 2005, A&A, 443, 643

[80] Ritter, H. 1988, A&A, 202, 93

[81] Kolb, U., Ritter, H. 1990, A&A, 236, 385

[82] Hurley J. R., Pols O. R., Tout C. A., 2000, MNRAS, 315, 543. doi:10.1046/j.1365-8711.2000.03426.x

[83] Iorio G., Mapelli M., Costa G., Spera M., Escobar G. J., Sgalletta C., Trani A. A., et al., 2023, MNRAS, 524, 426. doi:10.1093/mnras/stad1630

[84] Pols O. R., Schroeder K. P., Hurley J. R., Tout C. A., Eggleton P. P., 2009, yCat, 729. J/MNRAS/298/525

[85] Kruckow M. U., Tauris T. M., Langer N., Kramer M., Izzard R. G., 2018, MNRAS, 481, 1908. doi:10.1093/mnras/sty2190

[86] Agrawal P., Hurley J., Stevenson S., Szécsi D., Flynn C., 2020, MNRAS, 497, 4549. doi:10.1093/mnras/staa2264

[87] Fragos T., Andrews J. J., Bavera S. S., Berry C. P. L., Coughlin S., Dotter A., Giri P., et al., 2023, ApJS, 264, 45. doi:10.3847/1538-4365/ac90c1

[88] Spera M., Mapelli M., Bressan A., 2015, MNRAS, 451, 4086. doi:10.1093/mnras/stv1161

[89] Spera M., Mapelli M., Giacobbo N., Trani A. A., Bressan A., Costa G., 2019, MNRAS, 485, 889. doi:10.1093/mnras/stz359

[90] Mapelli M., Spera M., Montanari E., Limongi M., Chieffi A., Giacobbo N., Bressan A., et al., 2020, ApJ, 888, 76. doi:10.3847/1538-4357/ab584d

[91] Hobbs G. , Lorimer D. R., Lyne A. G., Kramer M., 2005, MNRAS , 360, 974

[92] Giacobbo N. , Mapelli M., 2020, ApJ , 891, 141

[93] Hut P. , 1981, A&A, 99, 126

[94] Zahn J. P. , 1975, A&A, 41, 329

[95] Zahn J. P. , 1977, A&A, 57, 383

[96] Harikane Y., Ono Y., Ouchi M., Liu C., Sawicki M., Shibuya T., Behroozi P. S., et al., 2022, ApJS, 259, 20. doi:10.3847/1538-4365/ac3dfc

[97] Aihara H., Arimoto N., Armstrong R., Arnouts S., Bahcall N. A., Bickerton S., Bosch J., et al., 2018, PASJ, 70, S4. doi:10.1093/pasj/psx066

[98] Sawicki M., Arnouts S., Huang J., Coupon J., Golob A., Gwyn S., Foucaud S., et al., 2019, MNRAS, 489, 5202. doi:10.1093/mnras/stz2522

[99] Madau P., Dickinson M., 2014, ARA&A, 52, 415. doi:10.1146/annurev-astro-081811-125615

[100] De Cia A., Ledoux C., Petitjean P., Savaglio S., 2018, A&A, 611, A76. doi:10.1051/0004-6361/201731970

[101] Madau P., Fragos T., 2017, ApJ, 840, 39. doi:10.3847/1538-4357/aa6af9

[102] Zahid H. J., Kashino D., Silverman J. D., Kewley L. J., Daddi E., Renzini A., Rodighiero G., et al., 2014, ApJ, 792, 75. doi:10.1088/0004-637X/792/1/75

[103] Baldry, I. K., Driver, S. P., Loveday, J., et al. 2012, MNRAS, 421, 621

[104] Ilbert, O., McCracken, H. J., Le Fèvre, O., et al. 2013, A&A, 556, A55

[105] Kajisawa, M., Ichikawa, T., Tanaka, I., et al. 2009, ApJ, 702, 1393

[106] Lee, K. S., Ferguson, H. C., Wiklind, T., et al. 2012, ApJ, 752, 66

[107] Grazian, A., Fontana, A., Santini, P., et al. 2015, A&A, 575, A96

[108] Santoliquido F., Mapelli M., Bouffanais Y., Giacobbo N., Di Carlo U. N., Rastello S., Artale M. C., et al., 2020, ApJ, 898, 152. doi:10.3847/1538-4357/ab9b78

[109] Santoliquido F., Mapelli M., Giacobbo N., Bouffanais Y., Artale M.C., 2021, MNRAS, 502, 4877. doi:10.1093/mnras/stab280

[110] Herwig F., 2000, A&A, 360, 952

[111] Sander A. A. C., Vink J. S., 2020, MNRAS, 499, 873

[112] N. Giacobbo. (2021) Ic4popsyn. [Online]. Available: https://github.com/GiacobboNicola/IC4popsyn

[113] Costa G., Girardi L., Bressan A., Marigo P., Rodrigues T. S., Chen Y., Lanza A., et al., 2019, MNRAS, 485, 4641. doi:10.1093/mnras/stz728

[114] Costa G., Girardi L., Bressan A., Chen Y., Goudfrooij P., Marigo P., Rodrigues T. S., et al., 2019, A&A, 631, A128. doi:10.1051/0004-6361/201936409

[115] Nguyen C. T., Costa G., Girardi L., Volpato G., Bressan A., Chen Y., Marigo P., et al., 2022, A&A, 665, A126. doi:10.1051/0004-6361/202244166

Appendix: MESA Inlist Files

In the following, I report the `inlist` files used to model VMSs during the MS (`inlist\_project\_H`) and the He-burning phase (`inlist\_project\_He`) and the `inlist` file used to model binary systems.

inlist_project_H

```
&star_job

! – begin with pre-main sequence model –
create_pre_main_sequence_model = .true.
pre_ms_relax_num_steps = 100
pre_ms_T_c = 3d5

! – rotation –
new_rotation_flag = .true.
change_rotation_flag = .false. ! rotation off unil near zams
new_omega_div_omega_crit = 0
near_zams_relax_omega_div_omega_crit = .true.
num_steps_to_relax_rotation = 50

! – prevent pgstar closing before terminating –
!pause_before_terminate = .true.

! – save the last pgstar output –
save_pgstar_files_when_terminate = .true.

! – save model after hydrogen burning –
save_model_when_terminate = .true.
save_model_filename ='/home/simonato/work_SEVN/H_burning_500_0.2Z_sol.mod'

! – display on-screen plots –
pgstar_flag = .true.

! – opacity table –
kappa_file_prefix = 'gs98'
show_kap_info = .true.

! – Z fractions –
initial_zfracs = 3

! – change net –
change_net = .true.
new_net_name = 'basic.net'
```

```
/ !end of star_job namelist

&controls

! Initial mass, Z and LOGS file in inlist_project_H_LOGS

! – output options –
history_interval = 2
profile_interval = 100
max_num_profile_models = 10000

! – mixing and exponential overshooting parameters –
mixing_length_alpha = 1.5

use_ledoux_criterion = .true.
alpha_semiconvection = 1
thermohaline_coeff = 0

overshoot_f_above_burn_h_core = 0.03
overshoot_f0_above_burn_h_core = 0.001

set_min_D_mix = .true.
min_D_mix = 1d-2
D_mix_ov_limit = 1d-2

! – mass loss –
use_other_wind = .true.
hot_wind_scheme = 'other'
Dutch_scaling_factor = 1
hot_wind_full_on_T = 1d0
cool_wind_full_on_T = 0d0
mdot_omega_power = 0

! – form of energy equation (MESA paper 4) –
use_dedt_form_of_energy_eqn = .true.
include_composition_in_eps_grav = .true.
convergence_ignore_equL_residuals = .true.
use_eosDT2 = .true.
use_eosELM = .true.

! – use gold tolerances –
use_gold_tolerances = .true.

he_core_boundary_h1_fraction = 1d-4
min_boundary_fraction = 1d-4
! – stopping condition –
xa_central_lower_limit_species(1) = 'h1'
xa_central_lower_limit(1) = 0.01

! – mesh controls –
mesh_delta_coeff = 1

! – timestep controls –
```

varcontrol_target = 1d-4
delta_lg_XH_cntr_min = -4.0d0
max_years_for_timestep = 1d3
retry_limit = 8

! – hydro info –
maxT_for_gold_tolerances = 1.5d9
backup_hold = 2
retry_hold = 1 ! default 1

! – Rotation diffusion factors (only for non-zero rotation) –
am_D_mix_factor = 0.0333d0
am_nu_factor = 1.0
am_gradmu_factor = 0.05

D_DSI_factor = 0
D_SH_factor = 1
D_SSI_factor = 1
D_ES_factor = 1
D_GSF_factor = 1
D_ST_factor = 0

! – MLT++ –
okay_to_reduce_gradT_excess = .false.
x_ctrl(1) = 0 ! for run_stars to check whether MLT++ on or not. Off for H burning

! – deeper homologous mesh –

max_logT_for_k_below_const_q = 100 ! MESA default 5
max_q_for_k_below_const_q = 0.99 ! MESA default 1.0
min_q_for_k_below_const_q = 0.99 ! MESA default 0.999d0
max_logT_for_k_const_mass = 100 ! MESA default 6
max_q_for_k_const_mass = 0.98 ! MESA default 1.0
min_q_for_k_const_mass = 0.98 ! MESA default 0.995

fix_eps_grav_transition_to_grid = .true.

/ ! end of controls namelist

inlist_project_He

&star_job

load_saved_model = .true.
saved_model_name ='/home/simonato/work_SEVN/H_burning_500_0.2Z_sol.mod'

! – prevent pgstar closing before terminating –
!pause_before_terminate = .true.

! – save the last pgstar output –
save_pgstar_files_when_terminate = .true.

```
! – save model after hydrogen burning –
save_model_when_terminate = .true.
save_model_filename ='/home/simonato/work_SEVN/He_burning_500_0.2Z_sol.mod'

! – display on-screen plots –
pgstar_flag = .true.

! – opacity table –
kappa_file_prefix = 'gs98'
show_kap_info = .true.

! – Z fractions –
initial_zfracs = 3

! – change net –
auto_extend_net = .true.

/ !end of star_job namelist

&controls

! – output options –
history_interval = 2
profile_interval = 100
max_num_profile_models = 10000


! – mixing and exponential overshooting parameters –
mixing_length_alpha = 1.5

use_ledoux_criterion = .true.
alpha_semiconvection = 1
thermohaline_coeff = 0

overshoot_f_above_burn_he_core = 0.01
overshoot_f0_above_burn_he_core = 0.001

set_min_D_mix = .true.
min_D_mix = 1d-2
D_mix_ov_limit = 1d-2

! – mass loss –
use_other_wind = .true.
hot_wind_scheme = 'other'
Dutch_scaling_factor = 1
hot_wind_full_on_T = 1d0
cool_wind_full_on_T = 0d0
mdot_omega_power = 0

! – form of energy equation (MESA paper 4) –
use_dedt_form_of_energy_eqn = .true.
include_composition_in_eps_grav = .true.
convergence_ignore_equL_residuals = .true.
use_eosDT2 = .true.
```

```
use_eosELM = .true.

use_gold_tolerances = .true.

he_core_boundary_h1_fraction = 1d-4
c_core_boundary_he4_fraction = 1d-4
o_core_boundary_c12_fraction = 1d-4
min_boundary_fraction = 1d-4


! – stopping condition –
xa_central_lower_limit_species(1) = 'he4'
xa_central_lower_limit(1) = 1d-10
!max_number_retries = 1000

! – mesh controls –
mesh_delta_coeff = 1

! – timestep controls –
varcontrol_target = 5d-4
delta_lg_XH_cntr_min = -4.0d0

! – hydro info –
!maxT_for_gold_tolerances = 1.5d9
backup_hold = 5
retry_hold = 5 ! default 1

! – Rotation diffusion factors –
am_D_mix_factor = 0.0333d0
am_nu_factor = 1.0
am_gradmu_factor = 0.05

D_DSI_factor = 0
D_SH_factor = 1
D_SSI_factor = 1
D_ES_factor = 1
D_GSF_factor = 1
D_ST_factor = 0

! – MLT++ –
okay_to_reduce_gradT_excess = .true.

gradT_excess_f1 = 1d-4
gradT_excess_f2 = 1d-2
gradT_excess_age_fraction = 0.99d0

gradT_excess_lambda1 = -1
x_ctrl(1) = 1

! – deeper homologous mesh –

max_logT_for_k_below_const_q = 100 ! MESA default 5
max_q_for_k_below_const_q = 0.99 ! MESA default 1.0
min_q_for_k_below_const_q = 0.99 ! MESA default 0.999d0
```

```
max_logT_for_k_const_mass = 100 ! MESA default 6
max_q_for_k_const_mass = 0.98 ! MESA default 1.0
min_q_for_k_const_mass = 0.98 ! MESA default 0.995

fix_eps_grav_transition_to_grid = .true.

/ ! end of controls namelist
```

inlist_project_bin

```
&binary_job

inlist_names(1) = 'inlist1'
inlist_names(2) = 'inlist2'

evolve_both_stars = .true.

/ ! end of binary_job namelist

&binary_controls

m1 = 150d0 ! donor mass in Msun
m2 = 50d0 ! companion mass in Msun
initial_period_in_days = 30d0

fm_limit = 1d-5
fr_limit = 1d-4
fe_limit = 1d-3

!transfer efficiency controls
limit_retention_by_mdot_edd = .false.


mdot_scheme = 'Kolb'
max_tries_to_achieve = 20

accretor_overflow_terminate = 10d0

mass_transfer_alpha = 0.0d0
mass_transfer_beta = 0.0d0
mass_transfer_delta = 0.1d0
mass_transfer_gamma = 1.2d0

do_wind_mass_transfer_1 = .true.
do_wind_mass_transfer_2 = .true.

max_wind_transfer_fraction_1 = 0.5d99
max_wind_transfer_fraction_2 = 0.5d99

terminate_if_initial_overflow = .false.
/ ! end of binary_controls namelist
```